Institute of Physics and Astronomy
University of Potsdam

Ultrafast X-Ray Studies on the Non-Equilibrium of the Magnetic and Phononic System in Heavy Rare-Earths

DISSERTATION

Zur Erlangung des akademischen Grades
Doctor rerum naturalium
(Dr. rer. nat.)
in der Wissenschaftsdisziplin: “Experimentalphysik”

eingereicht an der
Mathematisch-Naturwissenschaftlichen Fakultät
der Universität Potsdam

vorgelegt von

Azize Koç

Sarıoğlan-Kayseri

2018

https://doi.org/10.25932/publishup-42328

“*Dünyada her şey için en hakiki mürşit ilimdir, fendir.*”

“*The most truthful guide for everything in the world is science.*”

inspired by

Mustafa Kemal Atatürk

To him...

Abstract

In this dissertation the lattice and the magnetic recovery dynamics of the two heavy rare-earth metals Dy and Gd after femtosecond photoexcitation are described. For the investigations, thin films of Dy and Gd were measured at low temperatures in the antiferromagnetic phase of Dy and close to room temperature in the ferromagnetic phase of Gd. Two different optical pump-x-ray probe techniques were employed: Ultrafast x-ray diffraction with hard x-rays (UXRD) yields the structural response of heavy rare-earth metals and resonant soft (elastic) x-ray diffraction (RSXD), which allows measuring directly changes in the helical antiferromagnetic order of Dy. The combination of both techniques enables to study the complex interaction between the magnetic and the phononic subsystems. The transient responses showed that the magnetic and phononic systems of the rare-earth metals are for long timescales out of equilibrium.

For antiferromagnetic Dy and ferromagnetic Gd, the average transient strain after optical excitation was measured. It is induced in part by contractive stress due to the destruction of the magnetic order and of expansive stress due to the excitation of the phonon system. The dynamics differ strongly depending on the sample temperature and indicate a strong and long-lasting non-equilibrium between both subsystems. The time scale obtained for the structural recovery is up to hundreds of nanoseconds in antiferromagnetic Dy. Gd in the ferromagnetic phase equilibrates much faster and both materials show signatures of critical slowing down of the dynamics close to their phase transition temperatures. The analysis with a two-thermal-energies-model reveals the quantitative transient temperature changes of the phonon and the magnetic systems and the initial energy distribution between the subsystems. In addition to this, the complex heat flow through the multilayers consisting of Dy and non-magnetic metals is analyzed, where the transient temperatures are determined layer-specifically by UXRD. This proves the influence of the magnetic excitations on the heat transport.

The direct measurements of the magnetic structure indicate the strong spatial non-equilibrium within the spin system of the $4f$ electrons of Dy. Furthermore, after the instantaneous initial loss of the magnetic order upon photoexcitation, the magnetic system remains unordered for surprisingly long time, especially close to the phase transition temperature. The magnetic recovery starts after this equilibration time. This behavior is explained by the persistent temperature gradient in the magnetic system. A simple model was developed that uses the description of the long-range helical antiferromagnetic order of Dy as a sinusoidal wave and hence allows the determination of the temperatures in the $4f$ spin system. The transient direct measurements of the magnetic structure by RSXD confirm the theoretically predicted dynamical critical exponent of Dy. This was determined from the equilibration of the magnetic structure. The UXRD measurements yield also the same value of the dynamical critical exponent for Dy, which is given by the time on which the phonon temperature falls below the temperature of the magnetic system.

Zusammenfassung

In dieser Dissertation wird die Relaxationsdynamik des Gitters und der magnetischen Ordnung der zwei schweren, seltenen Erden Dy und Gd nach der Anregung mit femtosekunden Laserpulsen beschrieben. Für diese Untersuchungen wurden dünne Schichten von Dy und Gd bei niedrigen Temperaturen in der antiferromagnetischen Phase von Dy und nahe der Raumtemperatur in der ferromagnetischen Phase von Gd gemessen. Es wurden zwei verschiedene Experimente mittels optischem Anrege- Röntgen Abfrageverfahren durchgeführt, die ultraschnelle Röntgenbeugung mit harten Röntgenstrahlen (UXRD) und die resonante weiche (elastische) Röntgenbeugung (RSXD). Letzteres Verfahren erlaubt es, direkt die Änderungen der helikalen, antiferromagnetischen Ordnung zu messen. Die Kombination beider Techniken ermöglicht es, die komplexe Wechselwirkung zwischen dem magnetischen und dem phononischen Subsystem zu untersuchen. Die transienten Reaktionen zeigten, dass die magnetischen und phononischen Systeme der Materialien auf einer langen Zeitskala nicht im Gleichgewicht sind.

Für antiferromagnetisches Dy und ferromagnetisches Gd wurde die mittlere transiente Ausdehnung nach der optischen Anregung gemessen, die zum Teil aus einer kontraktiven Verspannung aufgrund der Zerstörung der magnetischen Ordnung und einer expansiven Verspannung aufgrund der Anregung des Phononsystems resultiert. Die Dynamik hängt stark von der Probentemperatur ab und zeigt ein starkes und lang anhaltendes Nichtgleichgewicht zwischen beiden Subsystemen. Die Zeitskala für die strukturelle Relaxation ist bis zu Hunderten von Nanosekunden in der antiferromagnetischen Dy. Gd in der ferromagnetischen Phase relaxiert viel schneller und beide Materialien zeigen Signaturen einer kritischen Verlangsamung der Dynamik nahe ihrer Phasenübergangstemperaturen. Die Analyse mit einem Zwei-Wärme-Energie-Modell zeigt die quantitativen, transienten Temperaturänderungen des phononischen und magnetischen Systems und die anfängliche Energieverteilung zwischen den Teilsystemen. Darüber hinaus wurde der komplexe Wärmefluss durch die Grenzflächen der dünnen, multilagigen Metallschichten aus Dy und nichtmagnetischen Metallen analysiert. Die Temperaturen wurden dabei schichtspezifisch über UXRD bestimmt. Dies beweist den Einfluss der magnetischen Anregungen auf den Wärmetransport.

Die direkten Messungen der magnetischen Struktur zeigen das starke lokale Nichtgleichgewicht innerhalb des Spin-Systems der $4f$-Elektronen von Dy. Außerdem bleibt das magnetische System nach dem sofortigen Verlust der magnetischen Ordnung nach der Anregung für lange Zeiten ungeordnet, insbesondere in der Nähe der Phasenübergangstemperatur. Die Relaxation findet erst danach statt. Dieses Verhalten wird durch den anhaltenden Temperaturgradienten im magnetischen System erklärt. Es wurde ein einfaches Modell entwickelt, das die Beschreibung der lang-reichweitigen, helikalen, antiferromagnetischen Ordnung von Dy als sinusförmige Welle nutzt und somit die Bestimmung der Temperaturen im 4f-Spin-System ermöglicht. Die transienten Resultate der magnetischen Struktur durch RSXD bestätigen

den theoretisch vorhergesagten, dynamischen kritischen Exponenten von Dy. Die UXRD-Messungen ergeben ebenfalls den gleichen Wert dieses Exponenten für Dy, der durch die Zeit gegeben ist, in der die phononische Temperatur unter die magnetische Temperatur fällt.

Contents

---

1. Introduction

Studying the multifarious dynamics of magnetic materials after manipulation of the material with ultrafast optical laser pulses is of big interest of current scientific investigations. The results lead to improvements of the current technological applications such in data storage and manipulation, but also give insight into the underlying mechanisms [1–4]. Among the magnetic materials, the rare-earth metals are investigated intensively because of their variety of magnetic structures over a wide temperature range [5]. The rare-earth metals are the elements in lanthanoid series in the periodic table of elements that possess the largest atomic magnetic moments due to their partially filled $4f$ orbitals. The interaction mechanisms between the localized $4f$ and the valence $5d6s$ electrons and also the crystal lattice due to the spin-orbit coupling, Ruderman-Kittel-Kasuya-Yosida indirect exchange interaction [6–8] and the strong magneto-elastic effects [9] show their importance for the science.

Time-resolved experiments performed in the last decade on magnetic materials reveal different time scales for the demagnetization of magnetic metals, which in particular differ between the rare-earth $4f$ (anti-)ferromagnetic metals and the $3d$ transition metal ferromagnets. The $3d$ ferromagnets exhibit a fast one-step demagnetization within a few 100 fs and also fast remagnetization on the ps time scale [10–12]. On the contrary, a two-step time scale is obtained for the loss of the magnetic order in $4f$ magnets. For ferromagnetic Gd and Tb, a fast demagnetization time of 760 fs and 740 fs is deduced from x-ray magnetic circular dichroism (XMCD), which is followed by much slower dynamics on the time scale of 40 ps and 8 ps, respectively [13]. The slow dynamics are attributed to spin-orbit coupling related to interaction between the magnetic system and the phonon system. Additionally, photoemission studies of the $4f$ magnetic linear dichroism and the $5d$ exchange splitting in ferromagnetic Gd showed a fast loss of $5d$ spin alignment within 800 fs and a much slower dynamics of the $4f$ system, which takes up to 14 ps to respond. The slow time scale is in this case attributed to the recovery of the $5d$-$4f$ intra-atomic alignment due to $4f$-spin-lattice relaxation [14], where electron and phonon systems are already coupled on this time scale. In other photoemision experiments for Gd, the $4f$-spin-lattice equilibration time was reported > 50 ps depending on the temperature and also the excitation fluence [15, 16]. For the loss of the helical antiferromagnetic order of Dy, XMCD experiments report two time scales of 290 fs and 14 ps at low temperature [17]. An investigation of the demagnetization process of the $5d$ and $4f$ electrons separately in antiferromagnetic Ho reports the ultrafast loss of the magnetic order with the same time dependencies for the $5d$ and $4f$ systems, which is attributed to the strong intra-atomic exhange coupling [18].

For the explanation of the different observed time scales, a theoretical microscopic model has been suggested by Koopmans *et al.* [19], which is based on electron-phonon-mediated spin flip scattering. They implemented the microscopic description of spin dynamics into a phenomenological 3 temperature model and infer both time scales from this model.

A literature survey reveals that most studies focus mainly on the fast initial demagnetization dynamics in magnetic metals and only few works report on the recovery of the magnetic order [20]. The question how the equilibrium is reached after destroying the magnetic order is particularly important for understanding the energy conversion between the different subsystems during the recovery dynamics. This is especially relevant for technological applications of magnetic metals where the thermal transport on the nanoscale is important [21].

This dissertation reports the complete structural and magnetic recovery dynamics of two heavy rare-earth metals Dy and Gd after the manipulation of the magnetic order with ultrafast laser pulses. Two different x-ray diffraction techniques were employed for the investigation of the magnetization dynamics, which is on the one side ultrafast x-ray diffraction with hard x-rays, UXRD, and on the other side resonant soft (elastic) x-ray diffraction, RSXD. The experiments were conducted at the synchrotron radiation facility BESSY II at the KMC3-XPP and FemtoSpex endstations. The use of UXRD for studying magnetization dynamics is not prevalent. Only several studies performed structural experiments on magnetic materials and concentrated on the magnetostrictive properties [22–24]. RSXD is a widely used experimental method for the direct quantitative, element-specific probe of the magnetization of a sample, charge or orbital order and long-range antiferromagnetic order in solids. Many studies investigated the magnetic order and magnetization dynamics of the complex antiferromagnetic state of heavy-rare earth metals at the $\mathrm{L_{III}}$ or $\mathrm{M_V}$ absorption edges by RSXD [25–28]. This thesis combines both experimental techniques on the same sample in order to study the complex interaction between the magnetic and phonon subsystems with a special focus on the slow dynamics close to the phase transition temperatures. Furthermore, it includes the complex heat transport in the multilayer system consisting of Dy and non-magnetic metals by analyzing the temperature changes for each layer.

The present dissertation is organized as follows:

In chapter 2 the fundamentals of magnetism are introduced. This chapter includes an overview of the magnetic and thermal properties of the rare-earth metals. Furthermore, the interaction of laser pulses and magnetic properties and the magnetic phase transitions are briefly reviewed. Chapter 3 covers the basic principles of x-ray diffraction. Here, a brief description of the magnetic x-ray diffraction is included. Chapter 4 and 5 contain the experimental part of this work. In chapter 4 the experimental setup at KMC3-XPP is introduced and the structure of three multilayer samples is described. Subsequently, the structural changes antiferromagnetic Dy and ferromagnetic Gd close to the second order phase transition temperature are discussed. The transient temperature changes after ultrafast heating of the phonon and the magnetic systems are determined separately performing an analytic solution of the two-thermal-energies-model (TTEM) [24]. Additionally, the influence of the magnetic excitations on the heat transport in nanolayers is described in antiferromagnetic Dy. In chapter 5, the experimental setup of the FemtoSpex endstation is described, which is followed by the presentation and discussions on the experimental results of the magnetic structure in antiferromagnetic Dy in thermal equilibrium and non-equilibrium after the ultrafast photoexcitation studied as function of temperature and excitation fluence. Additionally, a simple model is used to explain the experimental data. In chapter 6 the direct measurements of the magnetic structure by RSXD and the structural results by UXRD are reviewed and compared. Finally in chapter 7, the results are summarized and an outlook is given.

2. Magnetism

Magnetism has been an interesting and fascinating subject for mankind since thousands of years. In the 4th century BC it has been observed that “lodestone”, the mineral magnetite Fe_3O_4, attracts small iron pieces [29]. The phenomenon of magnetism remains up to the present days interesting and even becomes more and more important, both, in technology and science.

Fundamental achievements in theoretically understanding this phenomenon were first formulated in the 19th century by James Clark Maxwell who formed the basis of electromagnetism. The connection between electricity, magnetism, and light as an electromagnetic wave, is given by Maxwell’s equations [30]. In the 20th century, the semi-phenomenological explanation of magnetism is replaced by the atomic picture by means of quantum mechanics. The investigation of magnetism and related phenomena requires many specialized experimental techniques such as neutron diffraction [31], magneto-optical Kerr effect (MOKE), x-ray magnetic linear/circular dichroism (XMCD) [32], resonant soft x-ray diffraction (RSXD) etc. for the measurement of magnetic properties of matter.

In this chapter, the basics of magnetism including collective order of the magnetic moments in solids are summarized. Furthermore, the materials investigated in this thesis, which are heavy rare-earth metals, are introduced including their magnetic properties, heat capacity and transport properties. After that, the response of the magnetic metals after ultrashort photoexcitation is summarized. In the last section, the concept of the so-called critical behavior of second-order magnetic phase transitions is introduced.

2.1. Fundamentals

In the classical theory of magnetism, the macroscopic magnetization, M, of the materials describing the total magnetic moment per unit volume, is linearly related to the applied external magnetic field, H, by the dimensionless magnetic susceptibility χ:

$$M = \chi H \ . \tag{2.1}$$

The magnetization and the magnetic susceptibility are thermodynamic quantities and can be also derived from the Helmholtz free energy.

In quantum mechanics, the magnetic moment of any free atom in the absence of an external magnetic field originates from two main contributions: an intrinsic spin angular momentum of electrons, μ_S, and an orbital angular momentum via their circulating motion around the nucleus, μ_L [33] ,[1]

$$\mu_L = -g_L \mu_B \frac{L}{\hbar} \tag{2.2}$$

$$\mu_S = -g_S \mu_B \frac{S}{\hbar} \tag{2.3}$$

where L and S are the quantized orbital and spin angular momenta, g_L and g_S the corresponding g-factors, and $\hbar$ the reduced Planck's constant. μ_B is the orbital magnetic moment of one electron and is called Bohr magneton,

$$\mu_B = \frac{e\hbar}{2m_e} \tag{2.4}$$

with the charge e and the mass m_e of electrons. In general, in an atom with the atomic number Z, an interaction between the individual magnetic moments of the spins and the magnetic field arising from the orbital motion occurs. This interaction is the so-called spin-orbit coupling, which has an increasing magnitude proportional to Z^4 [35]. Spin-orbit coupling results in a total angular momentum, J, which is the vectorial sum of spin and orbital momenta. One has to distinguish between the so-called jj-coupling and L-S coupling (Russel-Saunders coupling), which depends on, whether the coupling potential is greater or less than the individual orbit-orbit and spin-spin couplings, respectively. The quantum numbers L, S, and J are determined via Hund's rules, which take the Pauli exclusion principle and Coulomb interaction into account [35, 36] and are a good prediction of the magnetic moment in the ground state of the atom. Consequently, the magnetic moment of the atom is given by

$$\mu_J = -g_J \mu_B \frac{J}{\hbar} \quad \text{with} \quad < J^2 >= J(J+1)\hbar^2 \ . \tag{2.5}$$

Magnetic materials are classified depending on the existence of ordered/disordered magnetic moments in the absence of an external magnetic field: diamagnetic, paramagnetic, ferromagnetic, antiferromagnetic, or ferrimagnetic. A diamagnetic material shows zero magnetic moment without magnetic field and possesses a negative magnetic susceptibility, which indicates that these materials are repelled by the applied magnetic field by orienting the magnetic moments opposite to the external field direction. In paramagnetic and antiferromagnetic materials the total magnetization is zero, however, they contain magnetic moments with either random or antiparallel orientation, respectively (Figure 2.1.a-b). There are more complicated magnetic alignments possible, for example a helical orientation of the magnetic moments as it is realized in metallic Dy (see section 2.2), which is considered as an antiferromagnetic material because of its zero net magnetic moment. Ferro- and ferrimagnetic materials possess a finite spontaneous magnetization, which is characterized by a parallel alignment of same magnitude or an antiparallel arrangement of different magnitude of the magnetic moments (Figure 2.1.c-d), respectively. These materials are attracted by magnetic field.

---

[1] Another contribution to total magnetic moment is the one of nucleus, which is about 10^{-3} times smaller than the one of electrons [34].

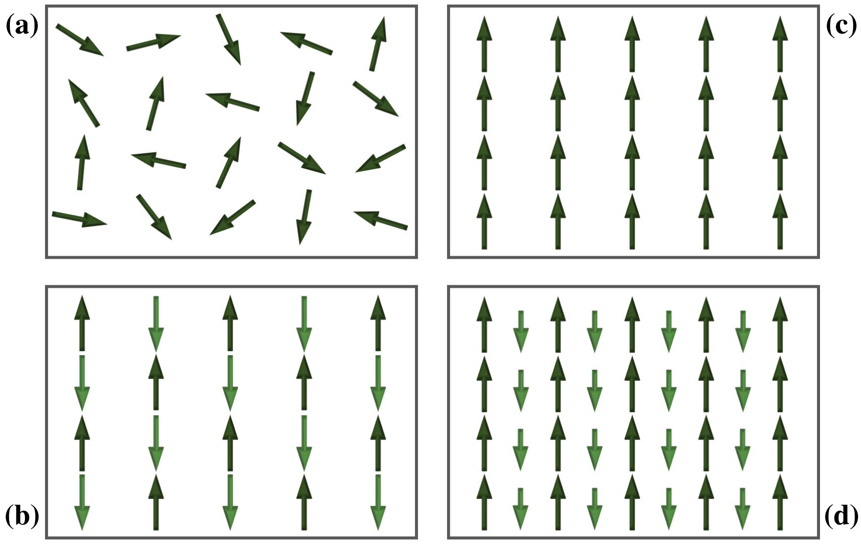

Figure 2.1.: Different magnetic moment alignments are depicted schematically in a) paramagmetic order, b) antiferromagnetic order, c) ferromagnetic order, and d) ferrimagnetic order [33].

The magnetization or magnetic susceptibility depends on temperature, T, and the temperature dependence for para-, ferro- and antiferromagnetic materials is shown in figure 2.2. The observed inverse proportionality of χ as function of temperature in the paramagnetic state is described by the Curie-Weiss law [37]. Below the ferro- or antiferromagnetic ordering temperature, the so-called Curie or Néel temperature, T_C and T_N, the magnetic susceptibility of ferromagnets diverges while the one of antiferromagnets indicates a strong variation depending on the direction of the applied magnetic field with respect to the orientation of magnetic moments in the material as indicated in figure 2.2 with dashed blue lines.

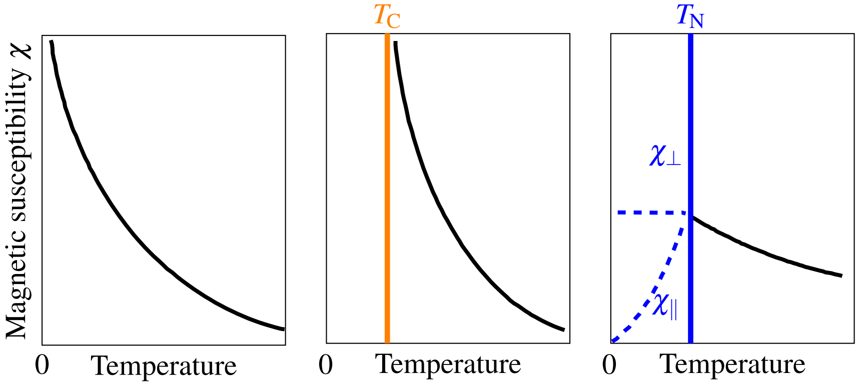

Figure 2.2.: Magnetic susceptibility of a paramagnet, a ferromagnet and an antiferromagnet. The Curie or Néel temperature, T_C and T_N are indicated with orange and blue lines. $\chi_\perp$ and $\chi_\parallel$ are the perpendicular and parallel susceptibility in antiferromagnetic phase, respectively [36].

In ferro-, ferri-, and antiferromagnetic materials, the interaction of the permanent atomic magnetic moments with each other produces a long range spatial order, which arises from the quantum mechanical exchange interaction, $\mathscr{J}$, between adjacent moments. This is nothing else than an electrostatic interaction taking the Pauli exclusion principle into account and was first proposed by Werner Heisenberg and Paul Dirac seperately. It considers two electrons that have to have an antisymmetric total wave function with either a spin-singlet state ($S = 0$) or spin-triplet state ($S = 1$) with the energy eigenstates E_S and E_T [36]. The exchange interaction is the energy difference of singlet and triplet eigenstates

$$\mathscr{J} = E_S - E_T \ . \tag{2.6}$$

In the case of $E_S < E_T$, which yields $\mathscr{J} < 0$, the singlet state is more favourable and therefore the spins align antiparallel. In the case of $E_S > E_T$, the parallel alignment is more favourable and a ferromagnetic coupling results. The exchange interaction energy typically ranges up to 100 meV, which is significantly greater than the dipole interaction of about 0.1 meV, which is much smaller than the thermal energy at room temperature of 25 meV [36, 38]. The Hamiltonian of two neighboring spins $S_{i,j}$ on the lattice sites i and j is described by the Heisenberg model and yields

$$\mathscr{H} = -\sum_{i>j} \mathscr{J}_{ij}\, S_i \cdot S_j \ . \tag{2.7}$$

Depending on the electronic configuration of the material, different types of interaction mechanisms might be present, for example a direct interaction arising from the direct overlap of wave functions of electrons with magnetic moments or an indirect interaction, for example the so-called RKKY interaction named after Ruderman, Kittel, Kasuya and Yosida [6–8]. This is the interaction mechanism in the rare-earth metals, that describes the connection between strongly localized $4f$ electrons via conduction band electrons, which leads to the wealth of the observed magnetic phases in rare-earth metals. In section 2.2.1 this will be explored in more detail.

2.2. Properties of the rare-earth metals

The atoms in the transition metal groups and lanthanoid series from $_{57}$La to $_{71}$Lu in the periodic table of elements possess a spontaneous magnetic moment, which makes them very important for the application in many magnetic materials. The elements in the lanthanoid series from Gd to Lu are often called heavy rare-earth elements. They are marked in the periodic table in figure 2.3 and two of them, Gd and Dy, are investigated in this thesis.

Heavy rare-earth metals exhibit the largest atomic magnetic moments originating from their open $4f$ orbitals surrounded by hybridized $5d6s$ valence electrons with [Xe] $4f^n(5d^{1\text{ or }0}\ 6s^2)$ atomic configuration [39], where n is a positive integer between 0 and 14. The prediction of the total magnetic moments of the rare-earth elements with oxidation number $+3$ using Hund's rules is very consistent with the experimentally determined values because one needs to consider solely localized $4f$ electrons. On the other hand, in transition metals, the magnetism is determined by the quasi free electrons, which leads to the

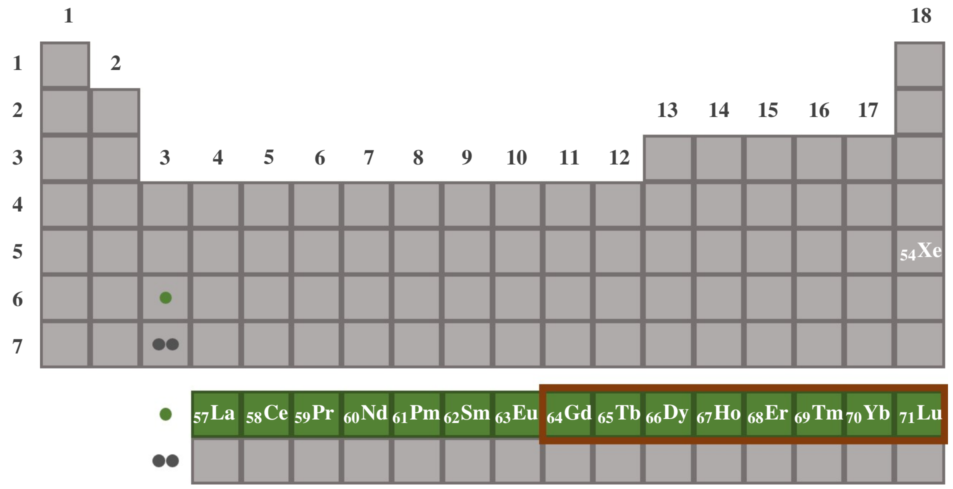

	Gd^{3+} [Xe] $4f^7$	Tb^{3+} [Xe] $4f^8$	Dy^{3+} [Xe] $4f^9$	Ho^{3+} [Xe] $4f^{10}$	Er^{3+} [Xe] $4f^{11}$	Tm^{3+} [Xe] $4f^{12}$	Yb^{3+} [Xe] $4f^{13}$	Lu^{3+} [Xe] $4f^{14}$
S	7/2	3	5/2	2	3/2	1	1/2	0
L	0	3	5	6	6	5	3	0
J	7/2	6	15/2	8	15/2	6	7/2	0
μ_J	7.94 μ_B	9.72 μ_B	10.63 μ_B	10.60 μ_B	9.59 μ_B	7.57 μ_B	4.54 μ_B	0

Figure 2.3.: The heavy rare-earth metals are the elements from Gd to Lu in the lanthanoid series that are marked in periodic system of elements. In the table, the quantum numbers S, L, J and the magnetic moment are determined experimentally and theoretically using Hund's rules on heavy rare-earth cations as listed in reference [36].

so-called Stoner band magnetism [36]. The μ_J values of each heavy-rare earth cation are listed in the table accompanying figure 2.3. They are calculated with equation 2.5 using the g_J-factor

$$g_J = 1 + \frac{J(J+1) + S(S+1) - L(L+1)}{2J(J+1)} \quad . \tag{2.8}$$

One finds that Dy and Ho show the largest total magnetic moment while Gd exhibits the largest pure spin moment with $L = 0$ and $S = 7/2$. Lu has a completely filled $4f$ shell, which results in a zero total magnetic moment of the cation.

All heavy rare-earth metals except Yb crystallize in the hexagonal close packed structure (hcp) at room temperature. The ratio between the interplanar distances, c/a, for these metals is less than the typical value of any hcp structure with $c/a = 1.633$ [40]. Additionally, the atomic volume decreases with increasing atomic number in the lanthanoid series, which is known as lanthanide contraction. This is the result of the poor shielding of the $4f$ electrons that causes an increasing attraction of the $5d6s$

electrons and hence, a reduced atomic radius [5].

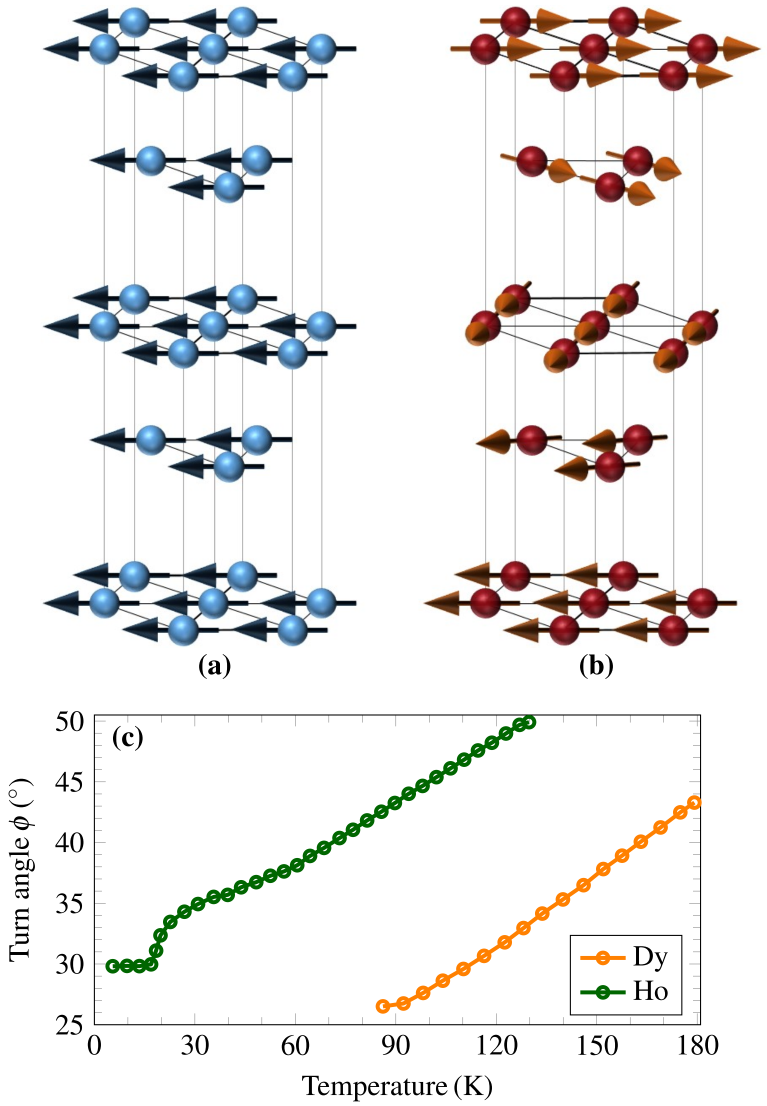

Figure 2.4.: Different alignments of $4f$ magnetic moments in hcp crystal structure of heavy rare earth metals are shown for a) ferromagnetic order along all crystal directions as observed in Gd, b) helical antiferromagnetic order along the c-axis that occurs in Dy, Ho, Tb [41]. c) Temperature-dependent turn angle of the magnetic moments between adjacent basal planes is reproduced for bulk Dy and Ho from references [42, 43].

The similar electronic configuration of rare-earth ions that is dominated by the outermost $5d6s$ electrons leads to very similar chemical properties. However, they exhibit various magnetic structures including conical ferromagnetic, ferromagnetic, and helical antiferromagnetic orientation that spread over a wide temperature range. In figure 2.4 two important types of magnetic order in a hcp cystal structure of rare-earth metals are shown. Gd exhibits ferromagnetic order below $T_C = 293\,\mathrm{K}$ (figure 2.4.a) [40] whereas Dy shows two different types of magnetic order: i) a ferromagnetic phase develops below

$T_C = 86\,\mathrm{K}$ [44], where the magnetic moments align parallel to each other in the basal plane and along the c-axis (figure 2.4.a). In this state, the Dy crystal structure is associated with an orthorombic distortion [9]. ii) A helical antiferromagnetic phase exists between 86 K and $T_N = 179\,\mathrm{K}$ [44] as indicated in figure 2.4.b. In this case, the atomic magnetic moments point into the same direction within the hexagonal basal planes and have an interplanar turn angle, ϕ, between adjacent basal planes staggered along the c-axes. Tb and Ho possess also two ordered magnetic phases and in their antiferromagnetic state, the same helical magnetic structure as in Dy is observed. Below 20 K, the magnetic structure of Ho is a conical ferromagnetic configuration, in which a small ferromagnetic component of $1.7\mu_\mathrm{B}$ exists parallel to the c-axis [43]. In the helical and conical spin arrangement the turn angle varies strongly with temperature (figure 2.4.c). For Dy the interlayer turn angle changes from about 43° to about 26° with decreasing temperature from T_N.

The formation of this great variety of magnetic structures is the result of the localized $4f$ moments, which are influenced by many forces in the crystal lattice. The free energy of the system can be derived from an effective Hamiltonian, $\mathscr{H}_\mathrm{eff}$, that is the result of competition between these interactions. The minimum of the free energy determines the type of the dominating magnetic structure at different temperatures:

$$\mathscr{H}_\mathrm{eff} = \mathscr{H}_\mathrm{exc} + \mathscr{H}_\mathrm{cfa} + \mathscr{H}_\mathrm{ms} \tag{2.9}$$

with $\mathscr{H}_\mathrm{exc}$ being the indirect exchange coupling term that is primarily responsible for the complex long-range oscillatory alignment in the rare-earth metals. $\mathscr{H}_\mathrm{cfa}$ is the crystal-field anisotropy, and $\mathscr{H}_\mathrm{ms}$ is the magnetostriction term arising from magneto-elastic effects [5]. In the following, these three terms are discussed in more detail.

2.2.1. Indirect exchange coupling (RKKY interaction)

In rare-earth metals, the interatomic overlap of $4f$ electronic wave functions is quite weak due to the fact that $4f$ electrons are strongly localized around the nucleus resulting in no significant direct interaction of neighboring ions. Two-ion coupling, i.e. $4f$-$4f$ coupling is mediated via the spin polarization of the surrounding electron gas induced by the direct intra-atomic overlap between $4f$ and conduction band electrons. The isotropic exchange Hamiltonian of RKKY interaction is given similar to equation 2.7 by

$$\mathscr{H}_{exc} = -\sum_{i>j} \mathscr{J}_{ij}^{RKKY} J_i \cdot J_j \tag{2.10}$$

with the total angular momenta J of ions at the lattice sites i and j.

The anisotropic exchange arising from the non-spherical $4f$ wave function with $L \neq 0$ is neglected here [45, 46]. The resulting exchange integral $\mathscr{J}_{ij}^{RKKY}$ is calculated including the intra-atomic coupling between $4f$ spins and the free electron gas [6–8, 47] and one obtains

$$\mathscr{J}_{ij}^{RKKY} \sim F(2k_F R_{ij}) \quad \text{with} \quad F(x) = \frac{\sin x - x\cos x}{x^4} \tag{2.11}$$

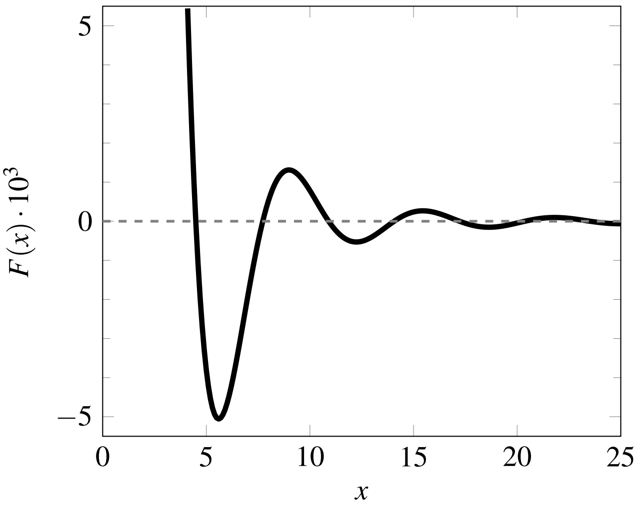

Figure 2.5.: The oscillatory behavior of the RKKY indirect interaction depending on the distance between atomic positions is introduced according to the function $F(x)$ (equation 2.11). The positive and negative values of this function correspond to a ferromagnetic and an antiferromagnetic coupling, respectively.

with the absolut value of Fermi vector k_F and the distance of the rare-earth ions R_{ij}. The amplitude of the effective exchange integral is determined with the function $F(x)$, which is depicted in figure 2.5 and is characterized by an oscillatory behavior depending on the distance between the atomic sites. A remarkable result of this is that due to the sign change of the function either a ferromagnetic or an antiferromagnetic order of the magnetic moments can occur as already mentioned in section 2.1. For all rare earth metals one may expect an oscillating antiferromagnetic magnetic structure for the case that only the isotropic indirect exchange interaction contributes to the magnetic exchange. Another important point is that the function $F(x)$ decays with R_{ij}^{-3}, which results in a long-range oscillatory exchange [47].

The initial peridiocity of the helical magnetic structure in the vicinity of the magnetic phase transition temperature can be derived from the wave vector-dependent paramagnetic electronic susceptibility, $\chi(q)$, which leads to the determination of the q-dependent spin fluctuations [5, 49, 50] and is proportional to the Fourier transform of the exchange integral, $\mathscr{J}^{RKKY}(q)$,

$$\mathscr{J}^{RKKY}(q) \propto |\mathscr{I}(q)|^2 \, \chi(q) \tag{2.12}$$

with the intra-atomic exchange coupling constant $\mathscr{I}(q)$. The wave vector, at which the maximum of the exchange energy is observed, τ, determines the minimum free energy and therefore the stable wavelength $2\pi/\tau$ of the helical magnetic structure. In figure 2.6, the exchange coupling along the c-axes of Gd, Tb, Dy and Ho as function of wave vector is reproduced from reference [48]. The exchange coupling is introduced as the difference of exchange energy in ferromagnetic and antiferromagnetic states, $\mathscr{J}(q) - \mathscr{J}(q=0)/(g-1)^2$, where $(g-1)^2$ is used as the scaling factor. These are experimental results derived directly from magnon dispersion relation measurements along the c-direction [51–54]. Gd possesses

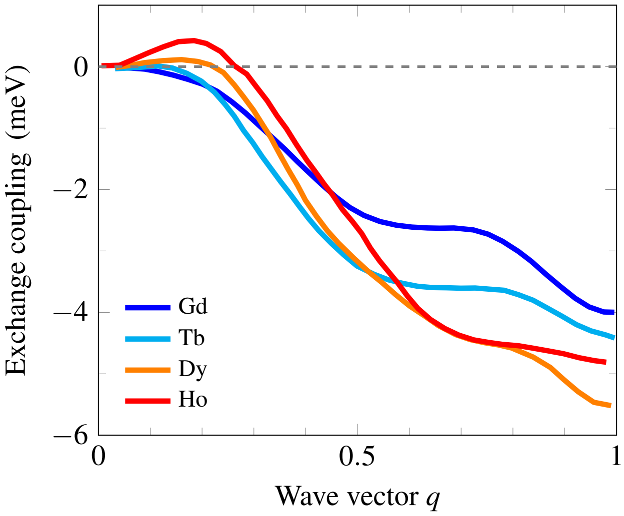

Figure 2.6.: The exchange coupling $\mathscr{J}(q) - \mathscr{J}(q=0)/(g-1)^2$ as function of wave vector for Gd, Tb, Dy and Ho is reproduced from reference [48]. These results are derived from magnon dispersion measurements for each element. The wave vector on the maximum of exchange coupling determines the periodicity of helical magnetic structure. For Gd, the maximum is at $q \approx 0$. For other heavy rare-earth metals, it is non-zero that points a periodic alignment.

the highest exchange at $\tau \approx 0$ pointing to a ferromagnetic coupling. For Tb, Dy and Ho the maximum of exchange coupling occurs at non-zero wave vectors and increases with increasing atomic number Z resulting in the decreasing periodicity that is related to lanthanide contraction [50]. This particular wave vector at the highest exchange energy is associated with the magnitude of the so-called “nesting vector” of the Fermi surface of rare-earth metals in the paramagnetic phase and this nesting vector might be responsible for the first occurance of helical magnetic structure at around T_N [55]. The calculated and measured Fermi surface of heavy rare-earth metals are presented and discussed in detail in reference [55].

2.2.2. Crystal-field anisotropy and magnetostriction

The crystal-field anisotropy and magnetostriction energies are usually much smaller than the exchange energy. However, especially at low temperatures, they become sufficiently large to induce changes of periodicity or even to drive magnetic phase transitions. In the following, these two contributions are more thoroughly discussed.

-Crystal-field anisotropy

The crystal-field anisotropy is the result of the electric field produced by the surrounding charge distribution around an ion in a crystal lattice. This has an effect on the shape of the orbitals and hence, the charge distribution in these orbitals. Thus, the crystal-field anisotropy is a one-ion interaction and reflects the crystal symmetry. Due to the strong spin-orbit coupling in the rare-earth elements, a deformation of the electronic cloud for each rare-earth ion via the crystal-field leads to an additional effect on the direction of the magnetic moment [9, 34, 40]. Rare-earth metals exhibit a rather large crystal-field anisotropy due to the large magnetic moment per ion and low symmetry in the hcp structure, which manifests in the fact that their easy magnetic axis lies in the basal plane and the *c*-axis is the hard magnetic axis [5].

-Magnetostriction

Magnetostriction is in general described as a relative dimensional change of a magnetic material in response to a change of its magnetization. It is the consequence of the so-called magneto-elastic coupling that is the coupling between the elastic properties of the crystal lattice and the magnetic properties of the material. It occurs due to a further modulation of the crystal-field anisotropy and exchange interaction in case of strain or a change of alignment of the magnetic moments. In elemental rare-earth atoms one has to include both, one-ion and two-ion interactions. The Hamiltonian $\mathscr{H}_{\mathrm{ms}}$ in equation 2.9 involves two contributions: elastic energy, which is quadratic in strain and associated with homogeneous strain components, and magneto-elastic energy, which is linearly proportional to the strain [56, 57].

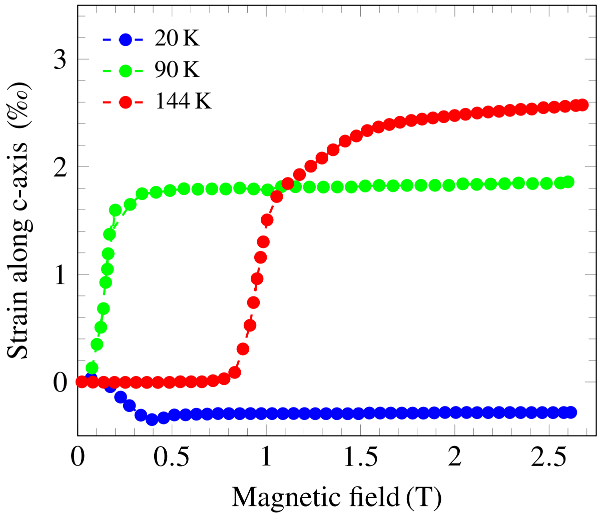

Figure 2.7.: The relative change of lattice constant along the *c*-axis of Dy in applied external magnetic fields parallel to *a*-direction in crystal is reproduced for different temperatures [58]. This length change is the magnetostriction and the lattice expansion is on order of 10^{-3} in magnetic fields up to 2.6 T.

All magnetic materials are magnetostrictive, however, a giant magnetostriction is a significant property of the rare-earth metals and their alloys with transition metals [39]. One example is depicted in figure 2.7 that shows the giant magnetostriction of Dy on the order of 10^{-3}, which is measured along the *c*-axis in applied external magnetic fields up to 2.6 T [58]. Another example is reproduced in figure 2.8, which indicates the temperature-dependent lattice constant without external magnetic field along the *c*-axis of a Dy single crystal measured by x-ray diffraction [44]. The discontinuous decrease of the *c*-axis lattice constant at T_C is a signature of the antiferromagnetic-ferromagnetic phase transition that involves pronounced changes of the lattice symmetry. The *c*-axis shows in the antiferromagnetic state an anomalous thermal expansion with decreasing temperature, which is observed also in the other heavy rare-earth metals [59, 60]. This anomalous temperature dependence of the lattice constant along the c-direction is associated with the helical magnetic structure that arises from the exchange magnetostriction and their relation is given in the molecular field approximation as shown in [61, 62] by

$$\left.\frac{\Delta c}{c}\right|_{\text{exc}} = \frac{cM_S^2}{Y}\left(\frac{d\mathscr{J}_1}{dc}cos\phi + \frac{d\mathscr{J}_2}{dc}cos2\phi + ...\right) \tag{2.13}$$

where c is the lattice constant, M_S the sublattice magnetization, Y the Young's modulus, $\mathscr{J}_1$ and $\mathscr{J}_2$ the exchange energies of the nearest neighbor and the next-nearest neighbor interaction, respectively, and ϕ denotes the interplanar turn angle. On the left of equation 2.13 the strain due to exchange magnetostriction is given as $(c - c_{ph})/c$ with c_{ph} being the lattice constant representing only phonon contribution, which does not include any magnetic interactions.

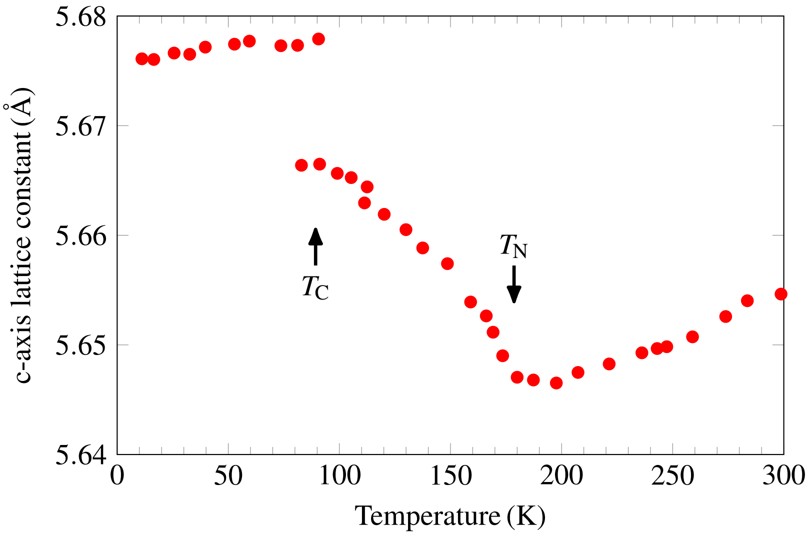

Figure 2.8.: The temperature dependence of lattice constant of Dy along the c-axis is reproduced from reference [44]. This is measured by x-ray diffraction on bulk Dy sample. Below $T_N = 179$ K, there is an anomalous thermal lattice expansion with decreasing temperature, which is related to exchange magnetostriction.

Equation 2.13 shows that the lattice strain due to magnetic interactions is proportional to the square of the sublattice magnetization. This relation is important for the effects observed in this thesis because the performed experiments include the measurements of the lattice constant by hard x-ray diffraction and the sublattice magnetization by resonant soft x-ray diffraction. These allow to crosscheck this proportionality experimentally in thermal equilibrium and dynamical results.

2.2.3. Heat capacity of rare-earth metals

The heat capacity of materials is a thermodynamic quantity that describes a certain amount of the energy required to change a unit temperature of a thermodynamic system. Using this definition, the total energy, ΔQ, that is deposited into the sample for example by the pump laser pulse in our time resolved experiments, can be calculated, which induces the temperature change, $\Delta T = T_2 - T_1$, of the sample. With the definition of the heat capacity at constant pressure, C_P, one obtains

$$\Delta Q = \int_{T_1}^{T_2} C_P(T)\, dT \quad . \tag{2.14}$$

The heat capacity consists of different contributions from the various degrees of freedom of the materials, in particular, in rare earth metals these contributions are stemming from electrons, C_e, the phonon, C_{ph}, and the magnetic system, C_m. There are other small contributions such as dilatation and nuclear contributions, which are negligible for the experiments in this work. It is important to remember that equation 2.14 is valid in case of thermal equilibration of all contributors.

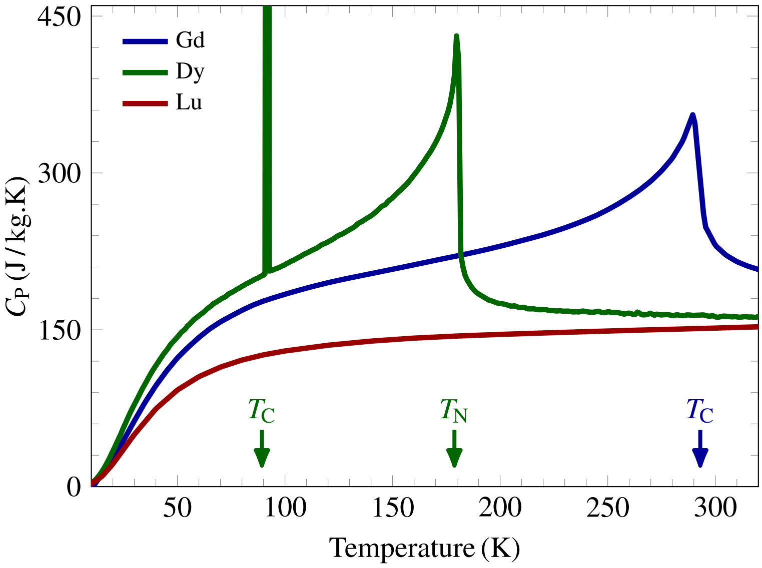

Figure 2.9.: The specific heat capacity at constant pressure of Gd, Dy, and Lu as function of temperature that are reproduced from the references [63–65], respectively.

The measured specific heat capacity of Gd, Dy and Lu as function of temperature are shown in figure 2.9 taken from the references [63–65]. The last element of heavy rare-earth series, Lu, possesses a fully filled $4f$ shell with the same number of valence electrons and thus is weakly paramagnetic. Therefore, the specific heat capacity of Lu contains only electronic and phononic contributions. The specific heat capacity of Dy in contrast shows two maxima at T_C and T_N, which indicate the associated phase transitions. The ferromagnetic Gd possesses only one peak at T_C. The specific heat capacity of Dy and Gd are much higher than the one of Lu in the ordered magnetic phases due to the contribution of the magnetic system. The continuous change of the specific heat capacity around the phase transition from the ordered to the disordered phase for Gd and Dy is a signature of a second order type phase transition.

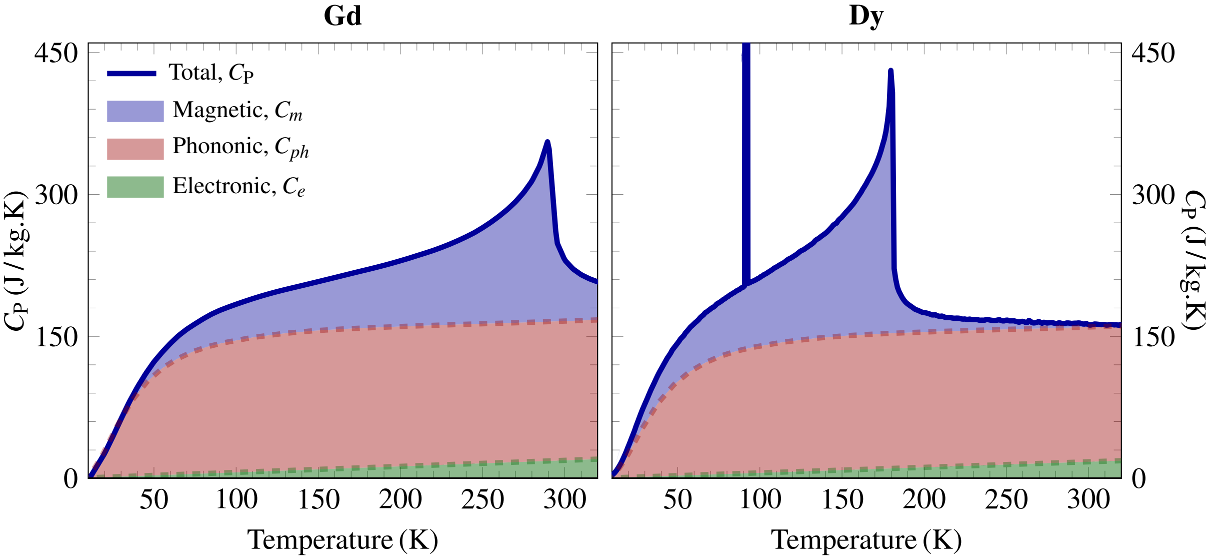

Figure 2.10.: The electronic, C_e, phononic, C_{ph}, and magnetic contribution, C_m, of the total specific heat capacity of Gd and Dy. The separation of each contributors is obtained with the same method as applied in reference [66] for Dy. This emphasizes the importance of the magnetic system in the magnetic phase of Gd and Dy as its fraction compared to the total specific heat capacity is quite high and becomes negligible in the PM phase above the transition temperature.

For the analysis of the experimental data in non-equilibrium of the contributing degrees of freedom, the seperation of each contribution to the total heat capacity of Dy and Gd is performed as applied for Dy in reference [66]: The electronic part is linear with temperature assuming the free electron model by Sommerfeld with $C_e = \gamma T$, where γ is the Sommerfeld constant, which has the values 10, 9.5 and 11.27 mJ/(mol·K^2) for Gd, Dy and Lu, respectively [67]. In order to extract the phononic part, the phononic heat capacity of Lu is rescaled using of the respective Debye temperatures, $\Theta_D = 152$ K and 158 K [68], of Gd and Dy as proposed in reference [69]. The magnetic contribution is then calculated by subtracting C_e and C_{ph} from the total heat capacity [70]. The results are presented in figure 2.10. The electronic contribution is quite small for the investigated temperature range. The phononic contribution is practically independent of temperature for temperatures above 100 K, the relevant range for the experiments presented in this thesis. The contribution of the magnetic system of Gd in its FM and Dy in the AFM phase is quite large, in particular close to phase transition and does not vanish instantaneously in the PM state that is associated with the existence of short-range magnetic ordering in PM phase.

2.2.4. Transport properties of rare-earth metals

The transfer of the thermal energy in a material is determined by the material-dependent heat conductivity coefficient, κ, and the temperature gradient, ∇T. It is important to note that the heat conductivity in the rare-earth metals is highly anisotropic, see for examples [71, 72]. However, this is not important for the presented experiments as c-axis response is dominant and hence anisotropy is not considered. For an isotropic system, the heat conductivity can in general be in the scalar form written as

$$\kappa = \frac{1}{3} C v l \ , \tag{2.15}$$

which is derived from the kinetic theory of gases [34]. Here, C denotes the heat capacity, v the particle velocity, and l the mean free path of particles between successive collisions during their movement. This general description can be specialized to different heat carrying quaseparticles that include the electrons, phonons, and magnetic system in the magnetic rare-earth metals. In normal metals, the thermal energy is transported dominantly by electrons [36].

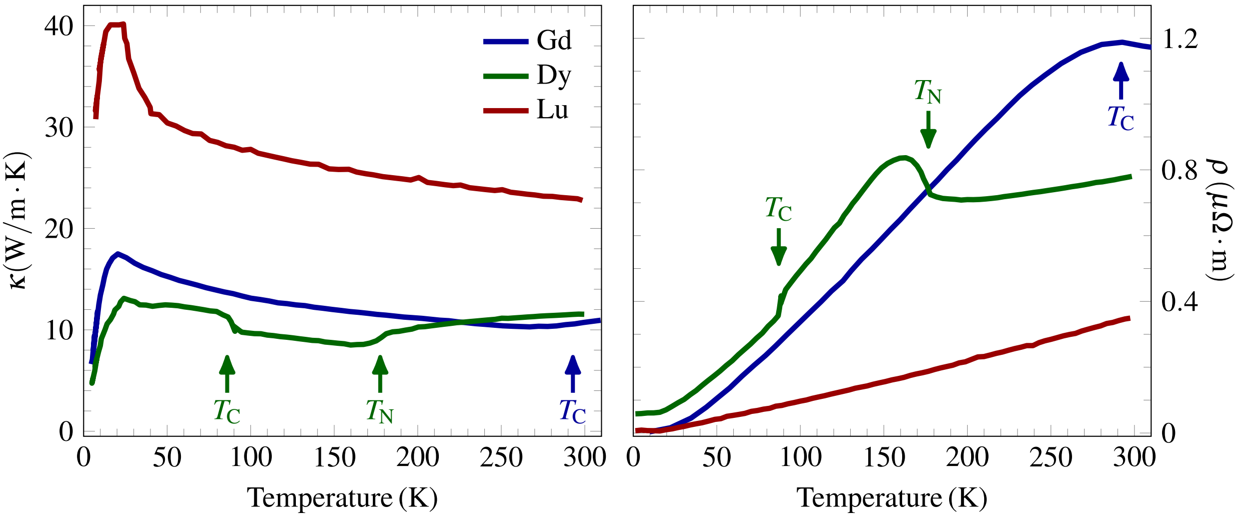

Figure 2.11.: The heat conductivity (left panel) and the electrical resistivity (right panel) of Lu, Dy and Gd as function of temperature measured along the crystallographic c-axis [71–73]. The weakly paramagnetic Lu represents a normal feature for a metal. On the other hand, the transport coefficients of Gd and Dy indicate anomalies that are related to their magnetic phase transition.

The heavy rare-earth metals are bad electrical and thermal conductors including Lu that is weakly paramagnetic compared to the normal metals [71]. This likely arises from additional collision of $5d6s$ conduction electrons with the large magnetic moments of the $4f$ electrons. This results in a reduced mean free path and thus a lower heat conductivity coefficient. Furthermore, there are characteristic features associated with the magnetic phase transitions observed in the temperature-dependence of κ and the electrical resistivity of the rare-earth metals that are not observed in other normal metals. In figure 2.11 in the left panel, the measured heat conductivity along the *c*-axis for Lu, Dy and Gd single crystals are reproduced from the references [71, 72]. Lu exhibits the temperature-dependence of κ for non-magnetic metals by contribution from electrons and phonons. In contrast to that, the heat conductivity of Gd and Dy are lower and more or less pronounced features are observed in the ordered magnetic phases. This indicates the existence of additional collisions of heat carriers, in particular the collisions of conduction electrons with the ordered large magnetic moments that reduces the heat conductivity effectively. In their PM phases, the heat conductivity increases other than the expected $1/T$ behavior for high temperatures confirming that the missing long-range magnetic order yields less scattering processes.

The right panel of figure 2.11 shows the electrical resistivities along the *c*-axis for Lu, Dy and Gd that are reproduced from the references [71, 73]. Similar to the case of the previously discussed heat conductivity, the resistivity of Lu shows the temperature-dependence of a normal metal whereas Gd and Dy have significantly higher resistances and clearly exhibit anomalies associated with the phase transitions.

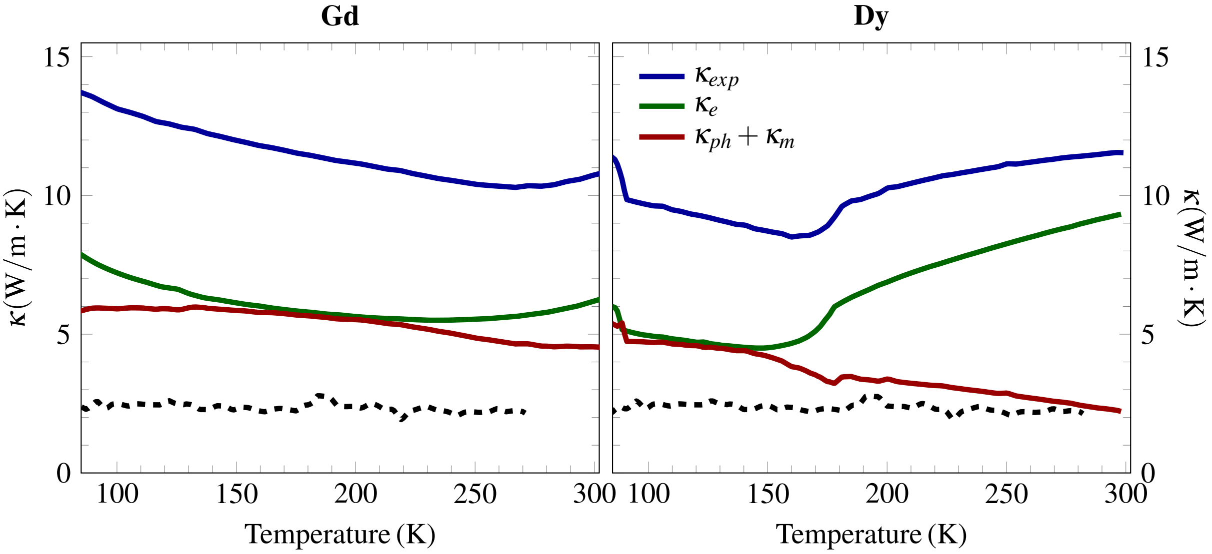

Figure 2.12.: Separation of the experimentally measured heat conductivity, κ_{exp}, into the electronic, κ_e, and cumulative phononic and magnetic contribution, $\kappa_{ph} + \kappa_m$, using Wiedemann-Franz law (equation 2.16) for Gd and Dy along the *c*-axis. The dashed black lines show only κ_{ph} obtained from the phononic heat conductivity of Lu neglecting the scattering of phonons by the magnetic system.

For metals, the Wiedemann-Franz law states that the Lorenz number, L, is a constant independent of temperature and metal given by the product of heat conductivity and electrical resistivity divided by the temperature:

$$L = \frac{\kappa_e \cdot \rho}{T} = 2.44 \cdot 10^{-8}\,\mathrm{W\Omega/K^2} \ . \tag{2.16}$$

One finds that the Wiedemann-Franz law is experimentally verified for temperatures above around 100 K. This emphasizes again the dominant role of the conduction electrons for the heat transfer in metals [36].

The separation of the heat conductivity into different contributions from each heat carrier is quite complicated as it is difficult to identify the various scattering mechanisms from the experimental data. The different quasiparticles interact with each other but also impurities, boundaries, etc. might in addition act as additional scattering centers. Yet, using the Wiedemann-Franz law, the electronic heat conductivity, K_e, of the rare-earth metals can be extracted using the measured electrical resistivity. The subtraction of K_e from the total heat conductivity provides then the sum of the phonon, κ_{ph}, and magnetic system, κ_m, conductivities. In figure 2.12, the separation of the total heat conductivity into the electronic and the sum of the phononic and magnetic part is displayed. Equation 2.16 and the previously shown electrical conductivity of Gd and Dy were used for this calculation. This analysis suggests that for both materials, κ_e and $\kappa_{ph} + \kappa_m$ are equally large in the magnetically ordered phases, however, they start to deviate significantly close to phase transition with increasing temperature. In the PM phase, κ_e increases almost linearly with increasing temperature as $\kappa_{ph} + \kappa_m$ decreases by the same amount. Especially for Dy, the proportionality of $\kappa_{ph} + \kappa_m$ to $1/T$ is clearly visible, which is consistent with a negligible magnetic contribution, in other words a negligible scattering from the magnetic system in PM phase due to short-range order. κ_{ph} of Gd and Dy is obtained from κ_{ph} of Lu by rescaling the respective Debye temperatures. Here, the scattering of phonons by the magnetic system is neglected. The result is shown in figure 2.12 with dashed black lines, which is ≈ 2 W/m.K for both materials and shows nearly constant temperature-dependence. Considering the results of the separation, one can conclude that the valence electrons are the dominant heat carriers also in the rare-earth metals.

2.3. Laser-induced dynamics in magnetic metals

The photoexcitation of the samples investigated in this thesis is performed by ultrashort laser pulses with a duration < 260 fs with wavelengths in near infrared region. The wavelength for the UXRD experiments is 1030 nm, in the RSXD, the excitation has been performed with 800 nm pulses. In this section, the excitation and response of the various degrees of freedom in the magnetic metals, i.e. valence electrons, phonon system, magnetic system, and the interaction between them is described in non- and quasi-equilibrium and the simplified models available in the literature are discussed. In general, by photoexcitation of a solid, Lambert-Beer's law describes the absorption of light as function of the sample depth, z, measured from the surface, by

$$I(z) = I_0 e^{-\alpha(\omega) z} \quad , \tag{2.17}$$

which results in an inhomogeneous spatial excitation profile in the solid. Here, I_0 is the intensity of the incoming light, $\alpha(\omega)$ the absorption coefficient of the solid for a certain frequency of the light, ω. The inverse of the absorption coefficient is the penetration depth, ξ, for the light with the wavelength, λ:

$$\xi = \frac{\lambda}{4\pi k} \ , \tag{2.18}$$

where k is the imaginary part of the refractive index, the so-called extinction coefficient, of the solid. Because of the high absorption and thus high reflectivity of metals in near infrared region, the penetration depth of the pump light is on the order of several 10 nm [74].

In metals, the energy of a near-infrared fs laser pulse is initially absorbed by the conduction electrons creating a non-thermal electronic distribution that does not obey the Fermi-Dirac distribution. Due to electron-electron collisions, the electronic system equilibrates thermally, typically on time scales of a few 100 fs [75, 76], resulting in an electronic temperature, T_e on order of a few 1000 K, depending on the excitation fluence. This is the consequence of the small electronic heat capacity as already shown in section 2.2.3. This quite high T_e, and at the same time still cold lattice and magnetic system leads to the thermal non-equilibrium. Thus, these three energy reservoirs interact with each other via different mechanisms and with different time constants. The coupling between these subsystems after ultrashort photoexcitation is widely described by the well-known three-temperature model (3TM) after ultrashort photoexcitation [77–79], which models the energy flow between the different reservoirs including non-equilibrium heat transfer. This model assumes a characteristic temperature for each energy reservoir, here T_e, T_{ph} and T_m for the electronic, phononic and magnetic systems, respectively, as function of spatial coordinate z, and time t. The energy transfer is given by the following three coupled differential equations

$$C_e \cdot \frac{\partial T_e}{\partial t} = \frac{\partial}{\partial z}\left(\kappa_e \frac{\partial T_e}{\partial z}\right) - G_{ep}(T_e - T_{ph}) - G_{em}(T_e - T_m) + P(z,t) \ , \tag{2.19}$$

$$C_{ph} \cdot \frac{\partial T_{ph}}{\partial t} = \frac{\partial}{\partial z}\left(\kappa_{ph} \frac{\partial T_{ph}}{\partial z}\right) - G_{ep}(T_{ph} - T_e) - G_{mp}(T_{ph} - T_m) \ , \tag{2.20}$$

$$C_m \cdot \frac{\partial T_m}{\partial t} = \frac{\partial}{\partial z}\left(\kappa_m \frac{\partial T_m}{\partial z}\right) - G_{em}(T_m - T_e) - G_{mp}(T_m - T_{ph)} \ , \tag{2.21}$$

where G is the energy exchange rate (called also coupling factor) between the participating subsystems denoted by the corresponding subscript, which is material specific and might depend on temperature [79]. $P(z,t)$ is the source term providing the initial excitation profile, which depends on the laser pulse duration and optical properties of the material. The first terms on the right describe the heat diffusion for the individual subsystems that is caused by the temperature gradient due to the inhomogeneous excitation profile.

A schematic representation of the possible interactions between the subsystems and the temporal evolution of the individual temperatures T_e, T_{ph}, and T_m as function of time are presented in figure 2.13 for two types of magnetic metal (I for transition and II for rare-earth ferromagnets) after excitation by a laser pulse [80]. It is necessary to remark here that the 3TM is questionable for the time scale of non-thermal electronic distribution (a few 100 fs).

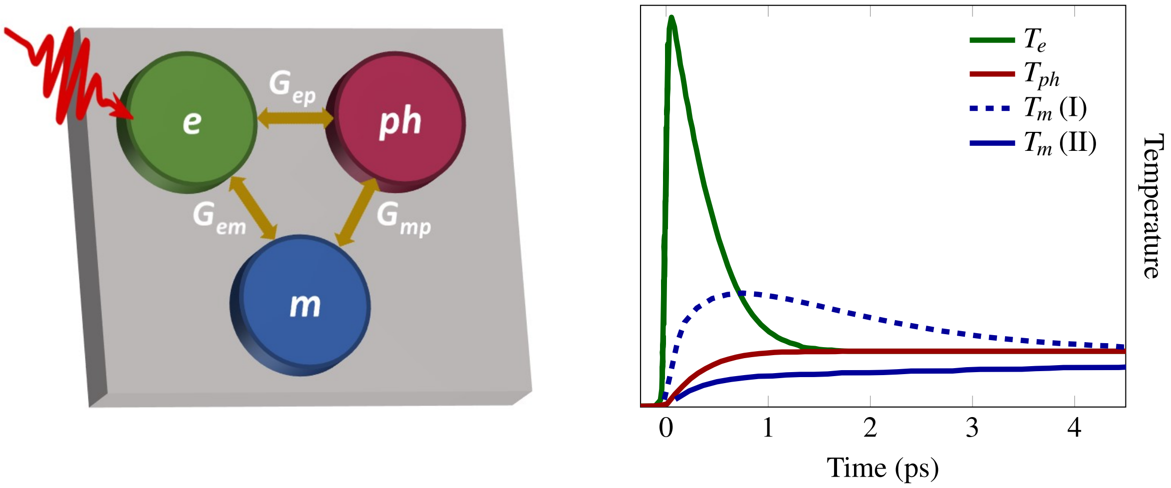

Figure 2.13.: Left panel: schematic representation of the three-temperature model for the possible energy flow between the different energy reservoirs: electron (e), phonon (ph), and magnetic system (m) in a magnetic metal after ultrafast photoexcitation. Right panel: An example of the temporal evolution for the different subsystems shown on the left panel, i.e. T_e, T_{ph}, T_m, respectively [80]. I and II indicates the type of the magnetic metal, a $3d$ and $4f$ ferromagnet, respectively.

After thermalization of the non-equilibrium electron distribution, the energy of the hot electrons is transferred to the phonon system by scattering processes, which leads to heating of the lattice due to electron-phonon interaction. The redistribution of the energy among them takes place untill the equilibration of their temperatures: $T_e = T_{ph}$. This occurs within the electron-phonon thermalization time, which typically is a few picoseconds for the metals [81, 82]. In addition to the thermal effects after photoexcitation, there are also non-thermal effects, such as ballistic electron transport and coherent phonon excitations [83, 84].

Another decay channel for hot electrons in magnetic metals is the magnetic system due to the coupling of the electron and magnetic systems. The hot electrons excite also spin excitations that are created for example by spin-flip processes, the change of the exchange energy, or the anisotropic character of spin-orbit coupling [85] leading to loss of magnetic order, the so-called demagnetization. This is observed as a reduction of the magnetization of ferromagnets or sublattice magnetization of antiferromagnets, which can be related to a temperature of the magnetic system, T_m. The first experimental determination of ultrafast demagnetization with 60 fs laser pulses has been reported by Beaurepaire et al. for a Ni thin film using time-resolved MOKE experiments [78]. They observed the maximal loss of remanent magnetization for Ni on the time scale of a few picoseconds and determined the electron-magnetic system coupling factor using 3TM. The following time-resolved experiments for ultrafast optical manipulation of magnetization report very short time scales on the order of a few 100 fs for the loss of magnetic order, which are related to Elliot-Yafett type spin-flip processes [19], superdiffusive spin transport [86], or angular momentum transfer [87, 88]. For a general review of different ultrafast demagnetization mechanisms, see reference [4].

The time for reaching the thermal equilibration of different temperatures, T_m and T_{ph} is the spin-lattice relaxation time, which occurs due to interaction of the magnetic and phonon systems. Microscopically the spin-phonon coupling is mediated by the spin-orbit coupling. I.e. phonons modify the crystal field causing anisotropic fluctuations, which couple to the spins [89]. The investigations presented in this thesis study most particularly the interaction of magnetic and phonon systems in recovery dynamics after photoexcitation.

Though the temperatures of three subsystems are equilibrated at later times, the temperature gradient due to the initial inhomogeneous excitation profile remains. The complete recovery of the system will occur then according to the heat diffusion equation

$$\frac{\partial T(z,t)}{\partial t} = D_{th} \frac{\partial^2 T(z,t)}{\partial z^2} \quad , \tag{2.22}$$

with the thermal diffusivity D_{th} of the metal.

2.4. Magnetic phase transitions

In fundamental thermodynamics, a phase transition is the change of a uniform thermodynamic property in a phase into another one by macroscopic variation of the thermodynamic parameters such as pressure, temperature, etc. The typical examples are solid to liquid, liquid to gas, paramagnetic to (anti-) ferromagnetic phase transitions. The different phases of matter are characterized by an order parameter, which is for example the macroscopic magnetization, M, in the ferromagnetic phase. It is non-zero below a critical temperature, T_{Cr}, and vanishes above. In the antiferromagnetic case, the order parameter is given by the sublattice magnetization, M_{S}.

Phase transitions are discussed and qualitatively described by the Landau theory of phase transitions, which is a consequence of the mean-field approach. In this theory, two concepts are considered: the Helmholtz free energy, F, and symmetry properties of the microscopic order parameter [90–92]. The order parameter and other thermodynamic quantities can be derived from the free energy of the system under constant macroscopic conditions. For example, the magnetization and heat capacity are given by the derivatives

$$M = -\frac{1}{V}\left(\frac{\partial F}{\partial H}\right)_T \quad \text{and} \quad C = -T\left(\frac{\partial^2 F}{\partial T^2}\right)_H \quad , \tag{2.23}$$

at constant temperature or external magnetic field, respectively. Here, V denotes the volume of the system and H the magnetic field strength.

In general, the phase transitions are classified after Ehrenfest by the discontinuity or continuity of the first derivative of the free energy at T_{Cr}. The former describes a 1st order phase transition and the latter defines the 2nd order. At a 1st order phase transition, the entropy exhibits a discontuinity at T_{Cr}, which is attributed to the latent heat that results in a co-existence of two phases: the ordered low temperature and the disordered high temperature phase. For the 2nd order phase transition, the change

Exponent	Quantity	Power Law
β	Magnetization	$M(T) \propto \epsilon^{+\beta}$
α	Specific Heat	$C(T) \propto \epsilon^{-\alpha}$
γ	Susceptibility	$\chi(T) \propto \epsilon^{-\gamma}$
ν	Correlation Length	$\xi(T) \propto \epsilon^{-\nu}$

Table 2.1.: The definition of static critical exponents of some thermodynamic quantities for second order phase transitions. $\epsilon = |(T - T_{\mathrm{Cr}})/T_{\mathrm{Cr}}|$ is the reduced temperature.

is continuous. As already mentioned, Dy undergoes transitions from a low-temperature ferromagnetic phase to an antiferromagnetic phase and finally to a paramagnetic phase. Both phase transitions are clearly observed in the measured temperature-dependent heat capacity shown in figure 2.9 [64]. One can distinguish here the abrupt 1st order FM-AFM transition at lower temperatures and the continuous 2nd order AFM-PM phase transition. The 2nd order FM-PM phase transition in Gd is also clearly observed in the heat capacity. The experiments performed during this thesis focused on the temperature regime of the AFM state of Dy and the FM state of Gd, hence the dynamics at the 2nd order magnetic phase transition has been studied.

A peculiarity of 2nd order phase transitions is that so-called critical phenomena become important close to phase transition temperature. In a critical regime below and above the critical temperature T_{Cr}, the correlation length, ξ, of fluctuations of the order parameter becomes larger and diverges at T_{Cr}. For magnetic phase transitions, the fluctuations of the magnetic moments become long-range as the transition temperature is approached. Thus, originating from the divergent length scale, the thermodynamic quantities magnetization, specific heat capacity etc. exhibit singularities in the critical regime in thermal equilibrium [93]. The temperature-dependence of these quantities can be described by a power law based on the reduced temperature $\epsilon = |(T - T_{\mathrm{Cr}})/T_{\mathrm{Cr}}|^{x}$ where the associated critical exponent, x, is different for each thermodynamic quantity. The important quantities and the associated power laws are listed in table 2.1 for zero external magnetic field.

These critical exponents are the same independent of the material, therefore they are universal. Yet, they differ for the different universality classes that are defined by the dimensionality of the system, d, and order parameter, D [38, 94]. These exponents provide the scaling law and the calculation of the critical exponents is successfully performed using the renormalization group theory [94–97]. In contrast to mean-field theory that does not consider fluctuations, the predictions by the renormalisation group are more precise. They have also been experimentally investigated and for spin systems in equilibrium, which are reviewed in detail in reference [98].

The 2nd order magnetic phase transitions observed in RE metals are part of the XY or Heisenberg magnets universality class with dimensionality of the magnetic moments of $D = 2$ or 3, respectively, and lattice dimension $d = 3$. Due to the strong in-plane anisotropy, Gd and Dy are XY magnets. For additional theoretical discussions about XY antiferromagnets and experimentally determined critical exponents of Dy in equilibrium, see references [99] and [100].

In addition to the critical behavior in equilibrium, the dynamical properties such as time- or frequency-dependent correlation functions, transport coefficients, relaxation times, ultrasonic attenuation, etc., exhibit anomalies in the non-equilibrium of the system close to T_{Cr} [101, 102]. This leads to a critical slowing down of the dynamics of the phase transition. For the systems out-of-equilibrium, the equilibration time of the order parameter in the critical regime diverges with a power law of the correlation length in equilibrium

$$\tau_{eq} \propto \xi^{z} \propto \epsilon^{-z\nu} \quad , \tag{2.24}$$

with the dynamical critical exponent $z \approx 2$ for the relevant universality class [93, 102, 103]. With $\nu = 0.669$ for XY magnets [97], the exponent of the equilibration relaxation time is expected to be around 1.34 for Dy.

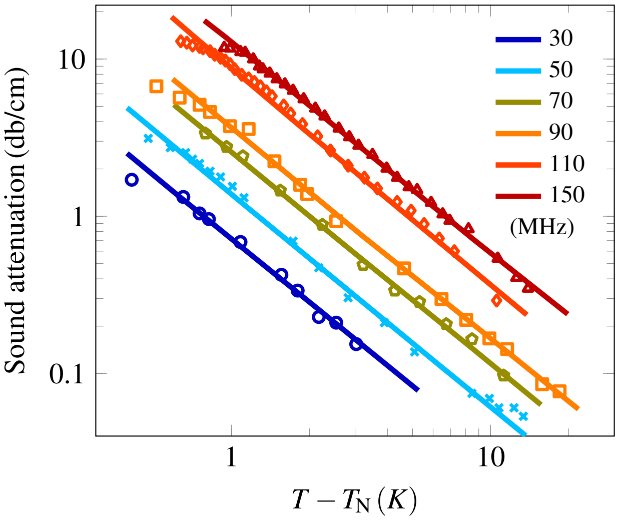

Figure 2.14.: Critical behavior of the longitudinal sound attenuation for different frequencies in the vicinitiy of T_{N} in a single crystal Dy sample that is reproduced from reference [104]. The symbols are the measured data points and the lines are the fit of a power law. The exponent of the exponential function is approximately 1.37.

In early experiments, the sound attenuation in heavy rare-earth metals is measured using the ultrasonic pulse echo technique [104, 105]. In figure 2.14, the critical attenuation of longitudinal sound waves along the c-axis for the frequence range of 30 to 150 MHz in the vicinity of T_{N} is reproduced from reference [104]. For higher frequencies, the attenuation increases. The critical exponent of 1.37 is obtained by fitting the experimental data with a power law.

Up to date, only few experimental investigations have been performed using quasi-instantaneous photoexcitation of Heisenberg ferromagnets using pump-probe experimental techniques [106–108]. In such experiments, also in the experiments performed during this thesis, it is important to take into account the critical dynamical response of the system due to the excitation into the non-equilibrium state. The ultrafast optical excitation might drive the system sufficiently close to or above T_{cr} and the critical slowing down is indeed observed.

3. X-ray diffraction

X-ray diffraction is widely used in science. After the discovery of the x-rays by W. C. Röntgen in 1895, x-ray diffraction from a periodic crystal lattice was first applied by Max von Laue in 1912 as an experimental tool for the experimental determination of the atomic static crystal structure [109]. The recent development of new x-ray sources with short and powerful x-ray pulses allowed the development and realization of time-resolved x-ray diffraction experiments. We have performed two different time-resolved x-ray diffraction methods in order to investigate the complete magnetization dynamics, which are on one side ultrafast x-ray diffraction with hard x-rays (UXRD), and resonant soft (elastic) x-ray diffraction (RSXD) on the other side. This chapter covers the basics of x-ray diffraction and is therefore split into two parts. First, the properties of x-rays and x-ray diffraction are briefly explained. In the second part, the principle of magnetic x-ray diffraction is described.

3.1. Fundamentals of x-ray diffraction

X-rays are electromagnetic waves in the classical description. In the quantum mechanical view, a monochromatic beam of x-rays is quantized into photons carrying the energy $E = \hbar\omega$ and the momentum $\mathbf{p} = \hbar\mathbf{k}$, where ω is the angular frequency and $\mathbf{k}$ the wave vector. The wavelength of x-rays, λ, is given by the following equation

$$\lambda = \frac{hc}{E} \longrightarrow \lambda[\AA] = \frac{12398}{E[\mathrm{eV}]} \tag{3.1}$$

with h being the Planck constant and c the speed of the light in vacuum. The wavelengths of x-rays range from several tenths to a few angstroms, which is commensurate with the typical interatomic distances of periodic lattice structures in crystalline materials. Thus, in case of exposing a cyrstalline sample to x-rays, constructive or destructive interference of the scattered x-rays occurs, the so-called x-ray diffraction [110].

The interaction between x-rays and matter can be in general classified as elastic and inelastic processes. For the former, the incoming photons are scattered from the electrons of the material conserving the initial energy, which is so-called Thomson scattering. The latter includes Compton scattering and the absorption of the x-rays. In both cases, the incoming photons lose their initial energy by different processes. For the structural investigations the elastic scattering is the dominant contribution and therefore it will be discussed first.

During the elastic process of the interaction between x-rays and matter, the electric field of the incoming x-rays forces the electrons to oscillate with the same frequency. This leads to the emission

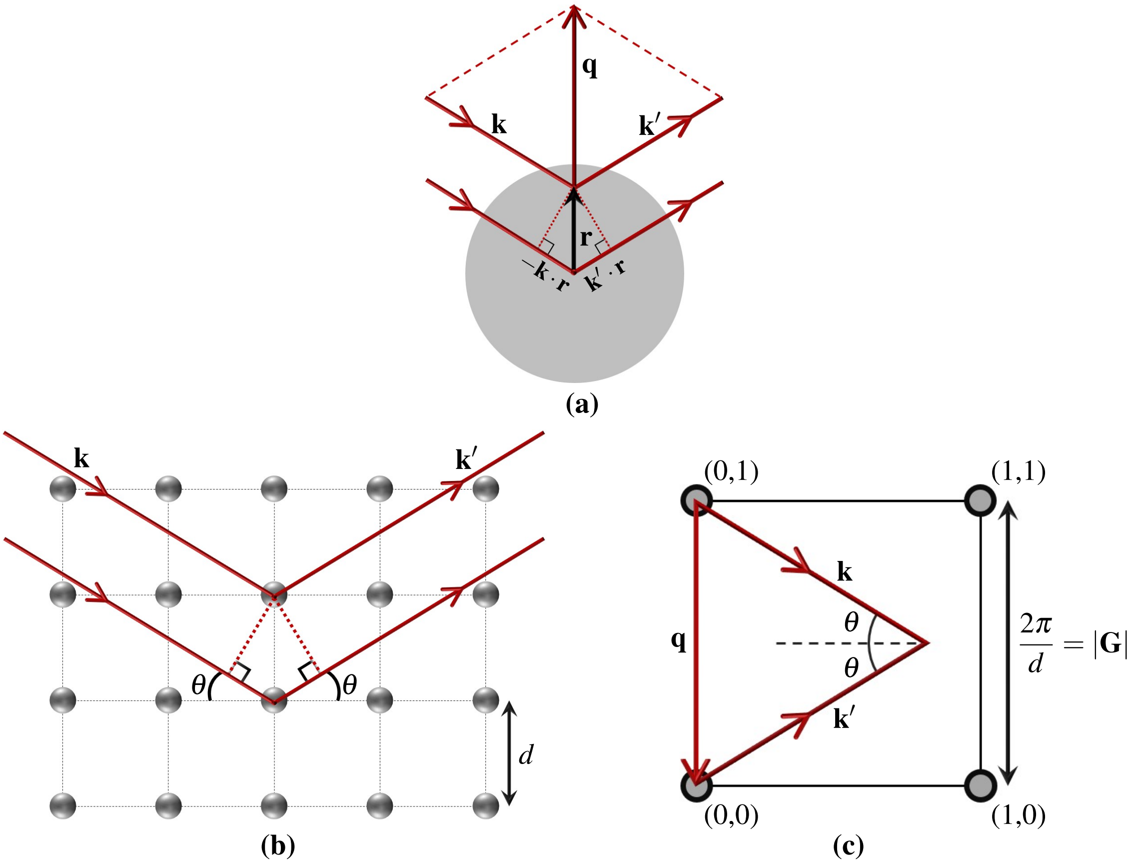

Figure 3.1.: a) Schematically representation of x-ray diffraction. a) Scattering of the incoming x-rays from one atom. b) Geometrical explanation of Bragg's law using a two dimensional crystal lattice in real space. c) Laue condition ($\mathbf{q} = \mathbf{G}$) in reciprocal space for constructive interference of scattered x-rays from a crystal. The sketches in this figure are reproduced from reference [111].

of x-rays in all directions as the charge acts as a dipole radiation source. If there are more than one scattering centers, the scattered waves with parallel wave vectors interfere constructively or destructively depending on the relative phase shift between them. Considering a single atom with the electron density $\rho(\mathbf{r})$ with $\mathbf{r}$ being the position vector, the relative phase shift $\Delta\phi$ between the scattered and incoming x-rays with the wave vectors $\mathbf{k}'$ and $\mathbf{k}$, respectively, is defined as

$$\Delta\phi(\mathbf{r}) = (\mathbf{k}' - \mathbf{k}) \cdot \mathbf{r} = \mathbf{q} \cdot \mathbf{r} \tag{3.2}$$

$$\mathbf{q} = \mathbf{k}' - \mathbf{k} \ , \tag{3.3}$$

with the scattering vector, $\mathbf{q}$ [111]. The wave vectors $\mathbf{k}'$ and $\mathbf{k}$ determine the scattering plane. An illustration of the scattering from a single atom is depicted in figure 3.1.a. The scattering amplitude $A(\mathbf{q})$

from one atom is calculated integrating over all scattering contributions and the relative phase shift

$$A(\mathbf{q}) = -r_0 P \int \rho(\mathbf{r}) e^{i\mathbf{q}\cdot\mathbf{r}} d\mathbf{r} \ , \tag{3.4}$$

where r_0 is the fundamental scattering length, which is equal to the classical electron radius, and P expresses the polarization factor [111]. The term without r_0 is the atomic form factor, $f^T(\mathbf{q})$, which quantifies the efficiency of the elastic scattering from an atom [112] and is usually referred to as Thomson contribution. For $q = 0$ f^T is equal to atomic number, Z, and decreases with increasing scattering vector as the phase shift becomes larger.

X-ray diffraction from a periodic crystalline structure is described geometrically by Bragg's law in real space and by the Laue condition that are sketched in figure 3.1.b and c, respectively. Considering the lattice planes as scattering centers in real space, the constructive interference occurs if the path difference between the scattered waves is an multiple integer of the wavelength, which depends on the interplanar lattice distance between two successive planes, d, and the angle of incidence θ:

$$2d \sin\theta = n\lambda \ , \tag{3.5}$$

where n is an integer. The angle that fulfills this condition is called Bragg angle of the specular reflection.

The translation of the unit cells in a crystal is given by the lattice vector $R_n = n_1\mathbf{a}_1 + n_2\mathbf{a}_2 + n_3\mathbf{a}_3$ defined in 3-dimensions, where $\mathbf{a}_{1-3}$ are the primitive lattice vectors along the corresponding directions. The moduli of the lattice vectors yield the lattice constants. The reciprocal lattice vector $\mathbf{G}$ is defined with the reciprocal primitive lattice vectors, $\mathbf{a}^*_{1-3}$, which fulfill the condition $\mathbf{a}_i \cdot \mathbf{a}^*_j = 2\pi\delta_{ij}$ as $\mathbf{G} = h\mathbf{a}^*_1 + k\mathbf{a}^*_2 + l\mathbf{a}^*_3$. Here, h, k,l are integers, the so-called Miller indices that define families of lattice planes with related orientation. The Laue condition demands that diffraction peaks at reciprocal space position occurs only if the scattering vector corresponds to a reciprocal lattice vector, which is equivalent to Bragg's law [111]:

$$\mathbf{k}' - \mathbf{k} = \mathbf{q} = \mathbf{G} \ . \tag{3.6}$$

The lattice distance for a given plane and the reciprocal lattice vector is related by $|\mathbf{G}| = 2\pi/d$. The scattering amplitude from a crystalline structure is then expressed as

$$A(\mathbf{q}) = -r_0 \underbrace{P \sum_j f^0_j(\mathbf{q})\, e^{i\mathbf{q}\cdot\mathbf{r}_j}}_{F(\mathbf{q})} \underbrace{\sum_{n=1}^{N} e^{i\mathbf{q}\cdot\mathbf{R}_n}}_{F_N(\mathbf{q})} \ , \tag{3.7}$$

where $F(\mathbf{q})$ denotes the unit cell structure factor that adds the scattering amplitudes from each atom in the unit cell. The term $F_N(\mathbf{q})$ is the lattice sum that accounts for all contributing unit cells exposed with x-rays [111].

The intensity measured by x-ray diffraction is proportional to $|A|^2$. As the modulation of the intensity depends particularly on unit cell structure factor, the peak intensity changes with the number of the unit cells, N, which is calculated by [113]

$$I(\mathbf{q}) \propto |F_N(\mathbf{q})|^2 = \left| \sum_{n_1=1}^{N_1} \sum_{n_2=1}^{N_2} \sum_{n_3=1}^{N_3} e^{i(q_1 a_1 n_1 + q_2 a_2 n_2 + q_3 a_3 n_3)} \right|^2$$

$$= \frac{\prod_{i=1}^{3} \sin^2\left(\frac{1}{2} N_i q_i a_i\right)}{\prod_{i=1}^{3} \sin^2\left(\frac{1}{2} q_i a_i\right)} \,. \tag{3.8}$$

For a semi-infinite crystal, this gives the sharp diffraction peak observed at the Bragg angle with the intensity proportional to $(N_1 N_2 N_3)^2$ [113]. The x-ray diffraction experiments in this thesis are performed on thin film samples with thickness of several ten nanometers. Because the out-of-plane dynamics along the c-axis of Dy and Gd was investigated, diffraction peaks perpendicular to the sample surface were selected. In this case, the number of the unit cells in-plane is infinite as the one along the out-of-plane direction is finite. The sketch in figure 3.2.a defines the directions of the corresponding scattering vectors. The measured intensity of the out-of-plane scattering vector in a thin layer is derived from equation 3.8

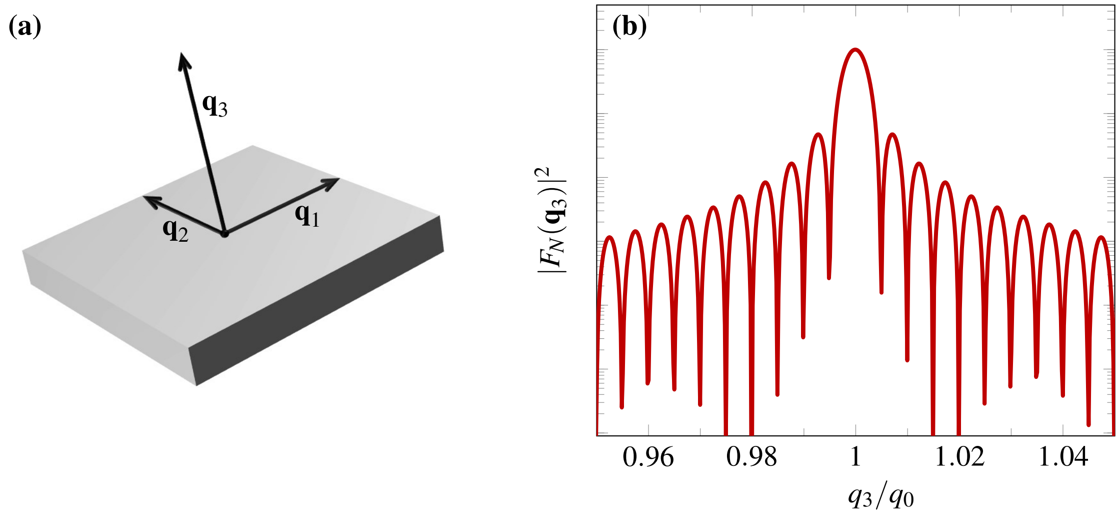

Figure 3.2.: a) Sketch of the directions of scattering vectors in a thin film crystals used in this thesis. b) Calculated term $|F_N(\mathbf{q}_3)|^2$ using equation 3.9 for a thin film with 50 nm thickness and out-of-plane lattice parameter of $c = 5$ Å. This term determines the scattering intensity. q_3 is normalized to the resulting scattering vector at maximum intensity q_0 that provides the Laue condition.

as

$$I(\mathbf{q}) \propto |F_N(\mathbf{q}_3)|^2 = N_1^2 N_2^2 \frac{\sin^2\left(\frac{1}{2}N_3 q_3 c\right)}{\sin^2\left(\frac{1}{2}q_3 c\right)} \quad . \tag{3.9}$$

The function $|F_N(\mathbf{q}_3)|^2$ calculated for a 50 nm thick crystal using equation 3.9 is presented in figure 3.2.b as function of the normalized scattering vector. The reflection at $q_3 = 1$ with the maximum intensity satisfies $q_3 c = 2\pi n$ for the out-of-plane component as given by the Laue condition. The oscillations on both sides of the diffraction peak with spacing Δq_3 are so-called Laue oscillations and provide the number of unit cells in case of the perfect ordering of the lattice planes, the coherent region, by the relation $\Delta q_3 = 2\pi/N_3 c$ [114]. Therefore, they provide information about the sample quality, particularly the crystallinity of the sample [114].

The calculations shown in this section do not consider the continuous intensity loss via reflection and transmission at each plane and also further interactions of the scattered x-rays with the sample. Therefore, the intensity is overestimated [110]. This approximation is called kinematical diffraction theory. A more realistic result is obtained if all possible interactions of the x-rays in the crystal are considered as it is done in the dynamical diffraction theory, see for example references [111, 115].

3.2. Magnetic x-ray diffraction

The structural investigations are performed off-resonance, that is, with an x-ray energy far away from the atomic absorption edges of Dy. Hence, the contribution of the magnetic scattering to the measured diffracted intensity is negligibly small: Considering one single electron, the ratio of the magnetic scattering crosssection to charge scattering contribution is given by the factor $(\hbar\omega/m_0 c^2)^2$, where $m_0 c^2 = 511\,\text{keV}$ [116]. This factor is on the order of approximately $3 \cdot 10^{-4}$ for the x-ray photon energy of 9 keV used for the structural investigations in this thesis.

Tuning the x-ray energy to the absorption edge of an element, the magnetic scattering becomes enhanced. In case of resonant elastic scattering at an absorption edge, electrons are excited by the incoming x-rays from core states into unoccupied intermediate electronic levels. Now these excited electrons relax back into their initial states and emit a photon with the same energy. The transition rate between two states depends on the polarization vector and the matrix element of the electric dipole [117] and thus, resonant x-ray diffraction is sensitive to charge, orbital and magnetic moment configuration of the atoms in the unit cell. The scattering amplitude is expected to be enhanced for the rare-earth metals for electric dipole transitions from $3d \rightarrow 4f$ at the $\mathrm{M_{IV}}$ and $\mathrm{M_V}$ edges [116]. This is theoretically predicted to be on the order of $100 r_0$ [118] starting with total atomic form factor $f(\mathbf{q},E)$ of an atom given by

$$f(\mathbf{q},E) = f^T(\mathbf{q}) + \underbrace{f^1(E) + i \cdot f^2(E)}_{\substack{\text{Dispersion}\\ \text{Correction}}} + f^M(\mathbf{q}) \ . \tag{3.10}$$

where $f^T(\mathbf{q})$ and $f^M(\mathbf{q})$ denote the non-resonant electronic and magnetic contributions, respectively. All terms include the polarization factor. The complex dispersion correction reveals the resonant scattering amplitude. It varies strongly as function of the x-ray energy, especially near the absorption edges and relates to refractive index of x-rays, $n = 1 - \delta + i\beta$ [119]. The dispersion and absorption indices, δ and β, of the refractive index of Dy is shown in figure 3.3.a measured near the $\mathrm{M_V}$ absorption edge at $E = 1293\,\mathrm{eV}$ reproduced from reference [120]. The contribution of the resonant scattering amplitude is calculated considering the dispersion correction of the atomic form factor and only for electric dipole transitions [116, 118]

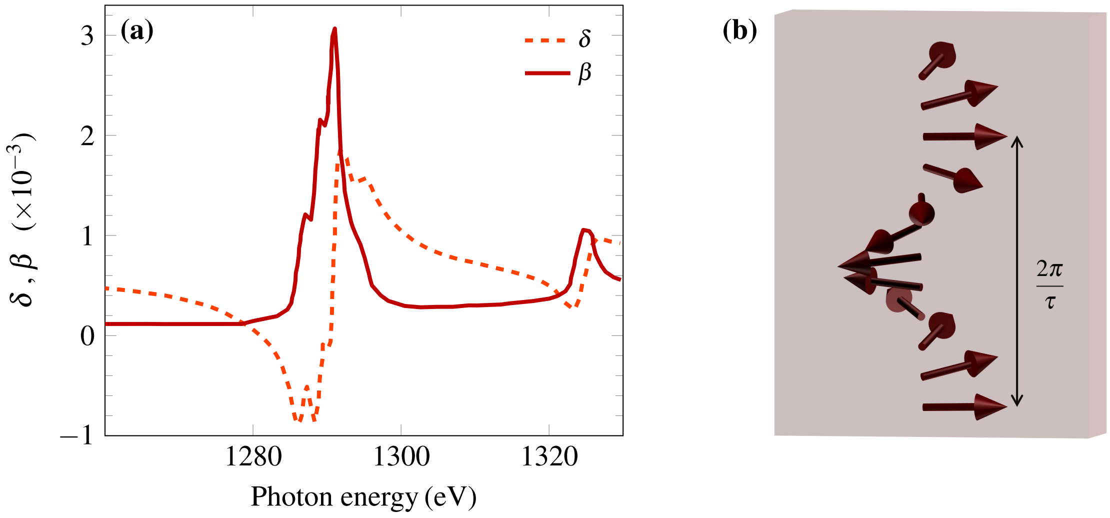

Figure 3.3.: a) The imaginary, δ, and real part, β, of the refractive index of Dy in the x-ray region near the $\mathrm{M_V}$ absorption edge. The data is reproduced from reference [120]. b) Sinusoidal modulation of the direction of the magnetic moments along the c-axis in antiferromagnetic Dy [27]. τ is the modulation vector in reciprocal space, which is measured by resonant magnetic diffraction.

$$f^M_{res}(E) \propto F^0(\hat{e}' \cdot \hat{e}) - iF^1(\hat{e}' \times \hat{e}) \cdot \hat{m} + F^2(\hat{e}' \cdot \hat{m})(\hat{e} \cdot \hat{m}) \ . \tag{3.11}$$

where F^{0-2} are the energy-dependent resonance factors and contain matrix elements, and $\hat{e}$ and $\hat{e}'$ denote the polarization vectors of the incoming and scattered x-rays, respectively. The unit vector, $\hat{m}$, points into the direction of the local magnetic moment [116, 121]. The first term in equation 3.11 is independent of $\hat{m}$ and is the resonance charge scattering. The second term is linear in $\hat{m}$ and is responsible for the first-order magnetic Bragg peak of an helical antiferromagnetic order, which is investigated in this work for the case of antiferromagnetic Dy. The helical antiferromagnetic structure is a sinuosidal out-of-plane modulation of the in-plane magnetization with a period of $2\pi/\tau$ as illustrated in figure 3.3.b that is described by a rotation of $\hat{m}$. The third term in equation 3.11 is quadratic in $\hat{m}$ and leads to a second-order magnetic Bragg peak. From equation 3.11 can be seen that the polarization of the x-rays is changed during the magnetic scattering. For a linearly π-polarized incoming x-ray beam with polarization parallel to scattering plane as used in the experiments in this work, the second term leads to scattered x-rays with mixed σ and π-polarization, where also the polarization perpendicular to the scattering plane occurs. A polarization analysis of the scattered x-rays would be useful in order to suppress the charge scattering because it does not affect the polarization [27].

4. Ultrafast x-ray diffraction experiments

In the first experimental part of this work, the structural dynamics of two rare-earth metals, Dy in the antiferromagnetic phase and Gd in the ferromagnetic phase, are investigated, in particular the recovery dynamics of the lattice under the influence of the magnetic system after the ultrafast photoexcitation. The influence of the excited magnetic system on the lattice arises due to the strong coupling of the phonon and magnetic systems through the large magnetostriction. Therefore the indirect measurement of the magnetic response by a structural experiment is possible. For this purpose, time-resolved ultrafast x-ray diffraction experiments (UXRD) are performed using femtosecond optical pulses as pump and hard x-rays the probe.

This chapter is split into three parts. In the first part, the experimental concepts are described including the setup, the samples, and the data acquisition process. In the second part, the experimental results of Dy are presented. First, the structural properties in thermal equilibrium of two Dy samples are shown and discussed. Then the results of the time-resolved UXRD experiments are presented and their analysis is discussed in order to show how the interaction of phonon and magnetic systems and the heat transport in the multilayer thin films can be obtained from the experimental data. The last part covers the experimental results and their analysis on the Gd sample.

The results shown in sections 4.2.3 and 4.3 are already published in [122] and [123], respectively.

4.1. Technical details

4.1.1. Experimental setup

The UXRD experiments have been performed at the KMC3-XPP beamline at the storage ring BESSY II, which is a third generation synchrotron source. At BESSY II, the electron bunches are accelerated to 1.7 GeV energy and circulate in the synchrotron ring with 1.25 MHz repetition rate. The pulse duration of the x-ray pulses is either 5 ps in low-alpha or 80 ps in single bunch or standard hybrid operation mode. The storage ring was operated in hybrid mode during the experiments presented in the following. In figure 4.1, a sketch of the beamline is shown. The electron bunches produce at the dipole bending magnet a broad energy spectrum of x-ray pulses. The spectrum transmitted through the Kapton window of the beamline ranges between 2 and 18 keV. The divergent beam after the bending magnet is collimated by the toroidal x-ray mirror M1 and directed to the double-crystal monochromator (Kristall-MonoChromator, KMC) that consists of two (111)-oriented Si single crystals, which allows an energy resolution of $\Delta E/E = 10^{-4}$ [124]. The second toroidal mirror M2 focuses the monochromatized beam in a distance of 7 m with a vertical divergence of 0.52 mrad to the spot size of 150 µm × 400 µm onto the sample. Several variable apertures and also Al and Pb absorbers are available between the source and the sample in order to shape and block the x-ray beam. At the focus point, the sample is placed on a 3+1 circle goniometer. A spherical aperture with a diameter of 50 µm or 100 µm can be introduced in a distance of around 50 mm before the sample [125]. With this aperture a small footprint of the focused x-rays is achieved, which has a FWHM of around 100 µm × 100 µm at normal incidence during the experiments according to the divergence. With this setup 10^8 ph/s or 10^6 ph/s are available at the sample position for static and time-resolved experiments, respectively. Due to the high photon flux of the well-collimated beam, the setup reliably measures lattice constant changes down to 10^{-6} [124].

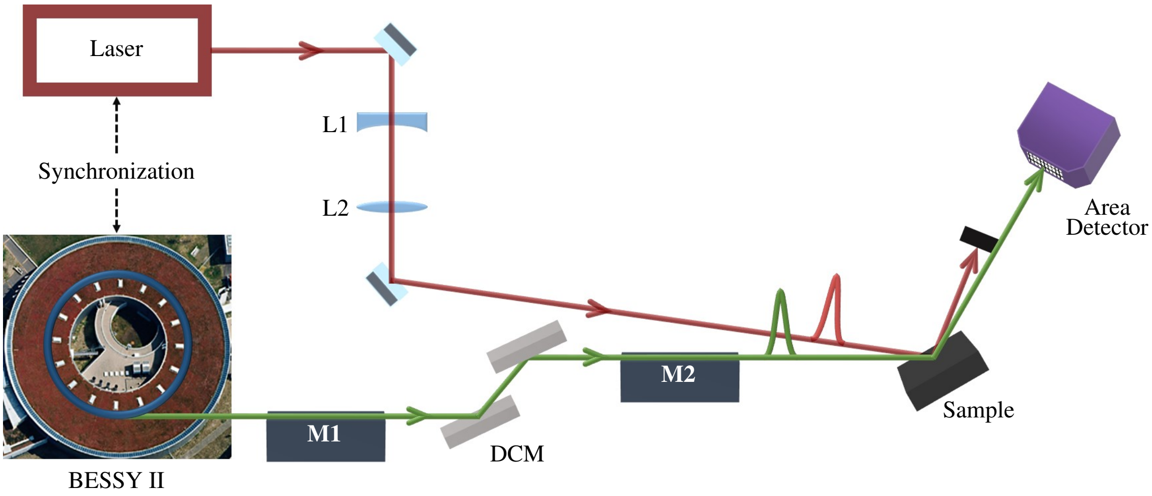

Figure 4.1.: Schematic of the UXRD setup at the KMC3-XPP beamline at BESSY II. M1 and M2: toroidal x-ray mirrors, DCM: double-crystal monochromator, L1 and L2: optical lenses.

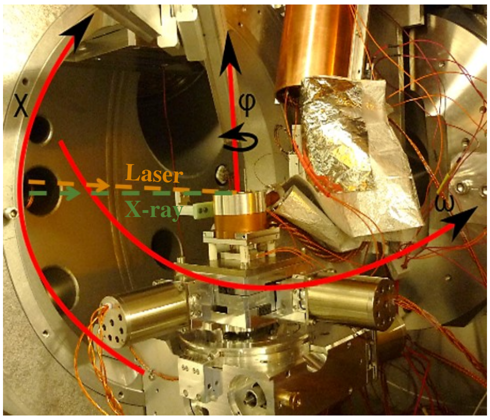

Figure 4.2.: 3 circle diffractometer in the vacuum chamber at the XPP endstation. The sample is mounted on the goniometer that allows rotating the sample with the three rotational degrees of freedom χ, ϕ, ω with respect to the incoming x-ray beam [126]. The direction of x-ray beam and the optical laser have a 2° angular offset as depicted by the dashed lines.

The sample is mounted on a thermally insulated sample holder that is connected by copper braids to the cold finger of a closed-cycle He cryostat allowing to cool the sample down to 20 K in a vacuum chamber with a pressure of 10^{-6} mbar. The goniometer in the diffraction chamber is shown in figure 4.2 and allows to measure out-of-plane and also in-plane Bragg reflections by rotating the sample around the beam axis, χ, its surface normal, ϕ, and perpendicular to the beam direction, ω. The sample is aligned to the center of rotation using the linear x, y, z stages mounted on the goniometer circle.

The optical laser is a commercial Yb-doped fiber laser (Impulse, Clark MXR) emitting optical pulses with a pulse duration of 250 fs at the central wavelength of 1030 nm ($E_{\text{photon}} = 1.2\,\text{eV}$). The oscillator of the laser is synchronized to the synchrotron frequency by a commercial synchronization unit (Menlo Systems) that allows to electronically adjust the delay between laser pulses and the x-ray probe pulses. The laser is operated at repetition rates between $f_{\text{rep}} = 208\,\text{kHz}$ and 1.25 MHz in order to utilize either only every eighth or every single bunch from the storage ring. Hence, measurements with a delay between optical pump pulse and x-ray pulse up to $\sim 5\,\mu\text{s}$ are possible. At 208 kHz repetition rate, the laser has a maximal average power of 2.1 W and 10 µJ pulse energy.

A telescope is setup with the lenses L1 and L2 as shown in figure 4.1. They have focal lengths of -500 and 500 mm, respectively. The telescope focuses the laser on the sample with an angular offset of 2° with respect to the incoming x-ray beam (see figure 4.2) and allows a variable laser spot size by changing the position of L1. The laser illuminates an area with FWHM of $240\,\mu\text{m} \times 290\,\mu\text{m}$ at normal incidence in our experiments. L2 is mounted in a motorized holder at a fixed distance to the sample of around 800 mm. This lens is moved perpendicular to the beam for the optimization of the spatial overlap between laser and the x-ray beam [125]. The reflected laser beam is blocked with an aluminum foil in order to protect the detector.

Diffracted x-rays from the sample are recorded by an area detector (Pilatus 100k [127]) that is mounted on the +1 rotational arm of the diffractometer outside of the vacuum chamber. With an electronic gate of 60 ns, which is sufficiently short for isolating the camshaft pulse in hybrid mode, the detector records selectively the x-ray pulses emitted by the single bunch [128]. Because the detector gate is synchronized to the laser repetition rate, only the x-ray pulses with a selected delay to the pump pulses are recorded. The other x-ray pulses that are emitted in the hybrid mode of the storage ring are rejected and hence do not contribute to the signal.

The samples investigated in this work are multilayer samples consisting of thin metal layers as sketched in figure 4.3. They are grown on the substrates by molecular beam epitaxy. Sample I and II are of 100 nm thick (0001)-oriented Dy layers that are sandwiched between two (0001)-oriented layers in order to prevent oxidation and to stabilize the helical antiferromagnetic order of Dy [129]. The thickness of Y layers is 10 nm in Sample I and 50 nm in Sample II. A 100 nm thick (110)-oriented Nb buffer layer connects this metallic sandwich structure to the $(11\bar{2}0)$-oriented Al_2O_3 substrate. As a remark, Y, Dy and Al_2O_3 crystallize in the hexagonal close packed (hcp) structure whereas Nb crystallizes in the body centered cubic structure (bcc) [122]. Sample III is a $\sim 90\,\text{nm}$ thick Gd layer grown on a (110)-oriented W single crystal substrate with bcc structure. A polycrystalline Y cap layer of 10 nm thickness is deposited to protect the sample [123]. Apart from the latter layer, all sample layers are epitaxially grown and exhibit a very good crystallinity.

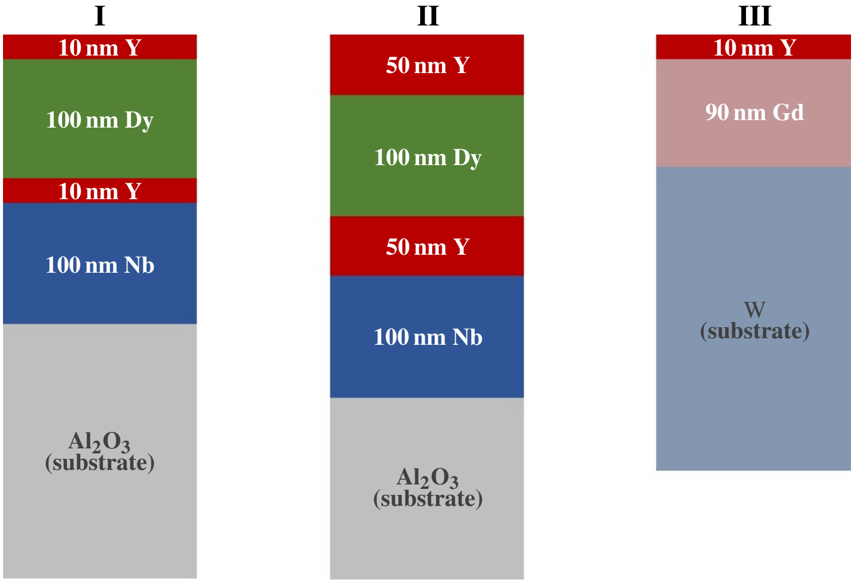

Figure 4.3.: Schematic structure of the samples investigated in this work. The rare-earth metals Dy and Gd are protected by Y capping layers, Dy is sandwiched between two Y layers. The Dy samples are grown on sapphire substrates with Nb buffer layers, the Gd layer is directly grown on the W substrate. All layers are single crystalline except the polycrystalline Y layer on the top of sample III.

The temperature-dependent refractive index of sample I and II are measured by spectroscopic ellipsometry. For the excitation wavelength of 1032 nm it yields a complex refractive index which is nearly independent of the temperature. From these measurements the optical penetration depth is determined using equation 2.18.

4.1.2. Data acquisition

The UXRD experiments are performed in the reflection geometry schematically depicted in figure 4.4.a and the symmetric out-of-plane z component, of the scattering vector is directly measured. In other words, $\omega - 2\theta$ scans with $\phi = \chi = 0$ were performed. Using the advantage of the area detector, additionally the in-plane component, x, can be extracted by mapping the diffracted intensity in reciprocal space [130]. Figure 4.4.b shows the scattering geometry in reciprocal space with the directions of incoming and scattered wavevectors, $|\mathbf{k}'| = |\mathbf{k}| = 2\pi/\lambda$, and the resulting scattering vector, $\mathbf{q}$, with respect to the sample surface. A wavelength $\lambda = 1.377$ Å (9 keV) of hard x-rays was used for the UXRD experiments presented in this thesis. At 9 keV, the extinction length of the x-rays is on the order of several µm [131], which makes the detection of the diffracted x-rays from all layers in the sample possible. The q_x component contains microscopic information such as mosaicity, coherently scattering domains etc. caused by non-specular scattering contributions [132] whereas q_z satisfies the Laue condition at $\omega + \theta = 2\theta$ and therefore yields the out-of-plane lattice constant with $c = 2\pi n/q_z^{\max}$, where n is an integer denoting the structural Bragg peak's order.

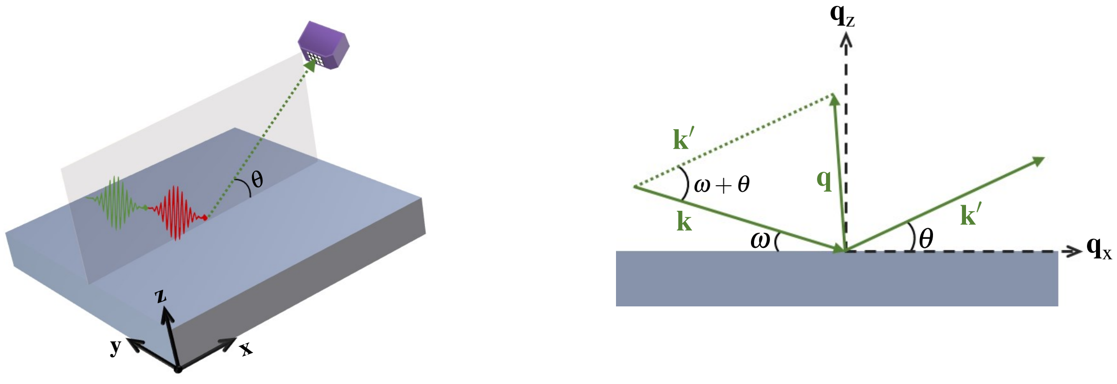

(a) (b)

Figure 4.4.: Experimental geometry of the time-resolved x-ray diffraction measurements a) in real space and b) in reciprocal space in two dimensions. The green wave packet indicates the x-ray pulse and the red one the pump laser pulse.

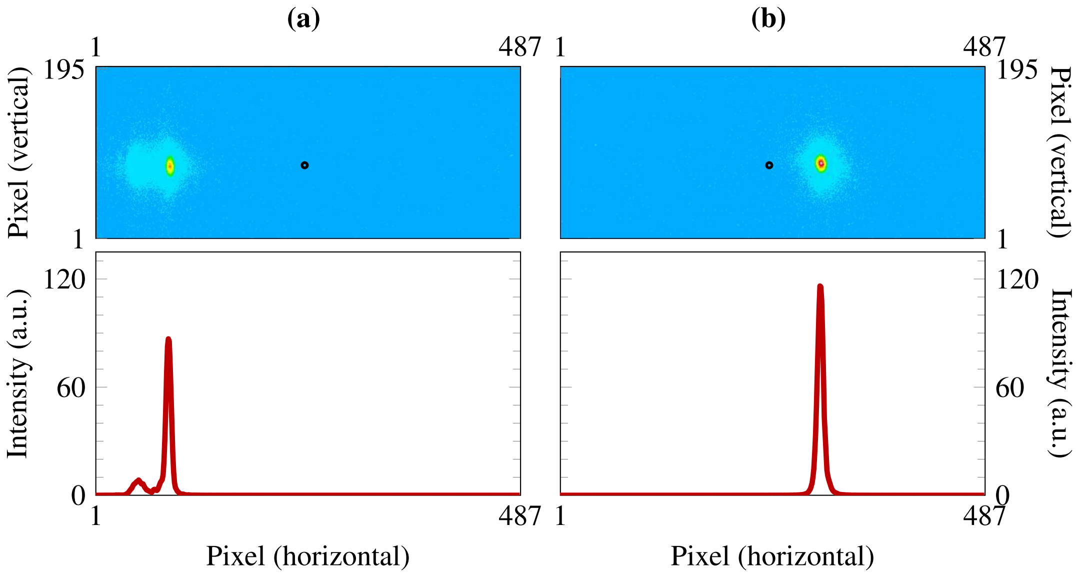

Figure 4.5.: Top row: The raw data captured with the area detector at fixed angle for one incidence angle ω. Bottom row: The integrated intensity of the raw data along y-axis (vertical pixels). a) and b) The diffraction signal from the Y and Dy layers at $\omega = 14^\circ$ and from the Nb layer at $\omega = 17.1^\circ$. The black symbol indicates the reference pixel at the fixed detector position. The presented data are measured on sample II at $T = 165\,\mathrm{K}$.

For the experiments on sample I and II, so-called ω-scans are performed where the incident angle ω is varied around the specular reflection and the detector is fixed at an angle and the scattering intensity is recorded as function of the ω angle. ω is varied for Y and Dy layer between 12.8° and 14.8° and the detector angle was fixed to $\theta = 30.4^\circ$. For Nb, ω is varied between 16.7° to 17.6° with the detector at 33.6°. The recorded raw data at one ω for such a measurement series is presented on the top of figure 4.5.a for

Y, Dy and figure 4.5.b for Nb of sample II at $T = 165$ K. The black symbol visualizes the reference pixel corresponding to the fixed angle of the detector. The horizontal pixel axis can be converted into $\theta(x)$ by a simple trigonometric calculation considering the relative shift along the horizontal pixels and the distance of the detector to the sample. On the bottom of figure 4.5, the integration of the data along the vertical pixel axis is shown. The pixel positions of the Bragg peaks of the layers are already visible, yet the corresponding scattering vectors are unknown. The conversion of the raw data to a reciprocal space map with q_x and q_z is performed using the following relation [132]

$$\mathbf{q} = \begin{pmatrix} q_x \\ q_z \end{pmatrix} = k \begin{pmatrix} \cos\theta - \cos\omega \\ \sin\omega + \sin\theta \end{pmatrix} . \tag{4.1}$$

with the knowledge of the corresponding θ values of each pixel. This transformation for $q_y = 0$ yields the results presented in this thesis. The complete reciprocal space map (RSM) of sample II at 165 K is

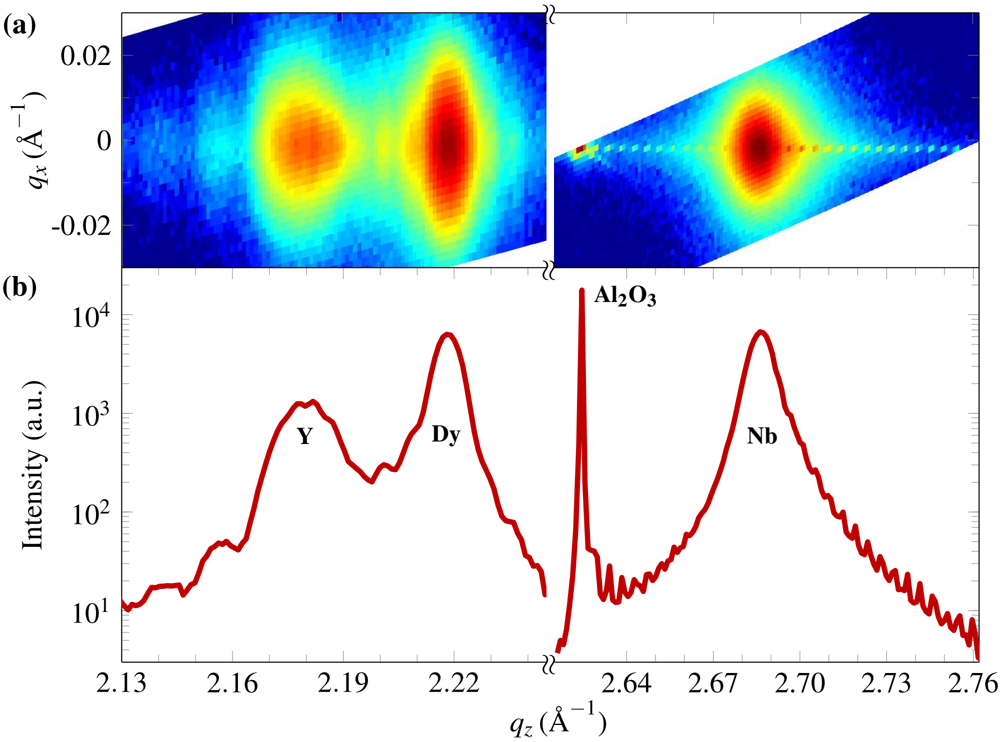

Figure 4.6.: a) Reciprocal space map of sample II at $T = 165$ K showing the 0002 reflections of Y and Dy layers and $22\bar{4}0$ reflection of the Al_2O_3 substrate and 220 reflection of Nb, respectively. b) The Bragg peaks of each layer are obtained after the integration along the q_x direction of the RSM shown in a) [122].

derived using equation 4.1 and shown in the top panel of figures 4.6.a and b that show the broad Bragg peaks of the metal layers and the sharp Bragg reflection of the substrate. The broadening in q_z of the thin layers occurs due to the limited film thickness and the broadening in q_x mainly suggests a mosaic structure of the sample [122]. Figure 4.6.b shows the corresponding out-of-plane Bragg reflections as function of q_z after the integration of the RSM along q_x.

The measurements on sample III were performed with a specular reflection geometry where ω and θ were varied at the same time, which conserves the symmetric scattering geometry, the so-called $\omega - 2\theta$ scan. Figure 4.7 shows the RSM and the Bragg reflection as function of q_z of the Gd layer. A Gaussian line shape is used as a fit function for the Bragg peaks of all layers and also the center of mass is calculated, in order to extract the out-of-plane scattering vector at maximum intensity q_z^{max} and the peak width, w, at FWHM of the Bragg reflections. A broad peak occurs not only due to the limited thickness of the layers but also due to a slight variation of their distribution along the measured direction, hence, it is a measure of the mosaic domain structure in the layer.

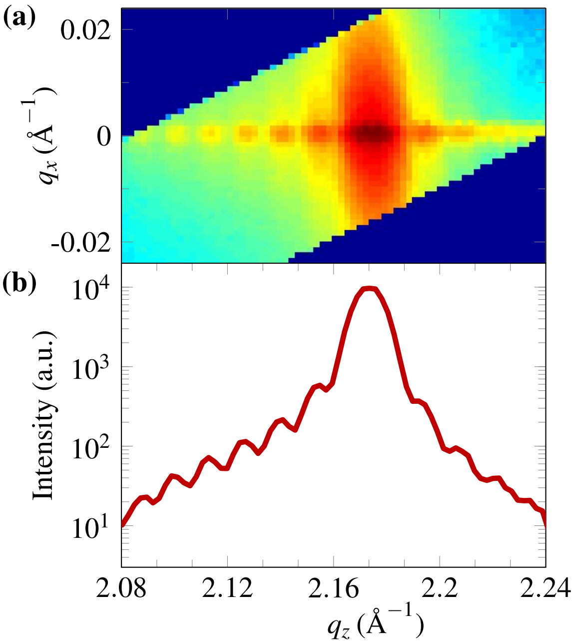

Figure 4.7.: a) Reciprocal space map of the 0002 Gd reflection of sample III at 275 K. b) The Bragg peak of Gd layer obtained after the integration of the RSM along q_x [123].

Up to now only static experiments have been presented. The second set of measurements are the time-resolved measurements. The time-resolved experiments need some preparations that are explained in the following:

i) For the correct interpretation of the UXRD experiments, the incidence fluence F_i needs to be known. It is calculated by

$$F_i = \frac{P}{A \cdot f_{\mathrm{rep}}} \sin(\theta + 2^\circ) \ , \tag{4.2}$$

with A being the pumped area at normal incidence and P the measured average power of the incident laser. An offset of 2° is added because of the angular offset between the laser and the x-rays.

ii) The spatial overlap of the laser and x-ray beam is optimized by translating lens L2 (see figure 4.1), perpendicular to the laser beam: This results in a movement vertically ($L_{\|}$) and horizontally ($L_{\perp}$) corresponding to a motion of the laser spot parallel and perpendicular in the scattering plane, respectively. The laser illumination of the sample, especially at high repetition rates, results in an average heating of the sample that leads to a static shift of the Bragg peak. Now the area detector is used as a point detector with an ω set to the maximum intensity of Bragg reflection. The integrated intensity recorded by the detector is measured while the laser spot is scanned across the sample by varying the position of L2. Figure 4.8 shows a typical overlap measurement on Dy while L2 was scanned along $L_{\|}$ and $L_{\perp}$. The observed minima in both directions indicate the spatial overlap region between laser and x-ray spots: The maximum shift of the Bragg reflection results in a reduction of the scattered intensity on the detector.

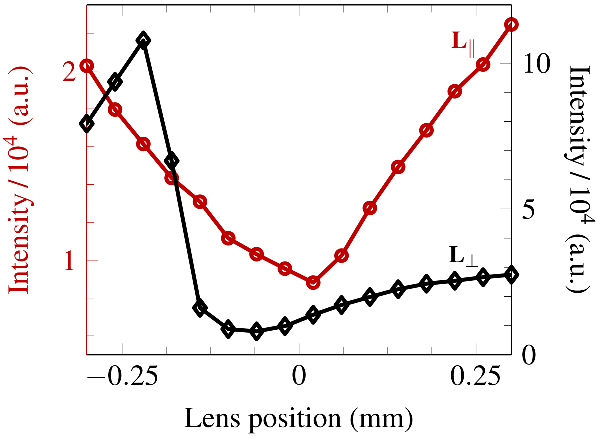

Figure 4.8.: The typical lens scan for optimization of the spatial overlap: The intensity detected by varying the position of the lens L2 vertically ($L_{\|}$) and horizontally ($L_{\perp}$) where ω is set to the maximum intensity of the Bragg reflection of Dy.

In a second step a more accurate overlap is achieved by calculating the RSM at each lens position because the heat-induced surface distortion leads to a shift in q_x. Further details of these measurements are explained in reference [125].

iii) The temporal overlap of the laser and x-ray pulses is determined by recording the diffracted intensity as function of the delay between laser and x-rays. For this measurement, typically the highest laser power below the damage threshold of the sample is used in order to minimize the integration time required to obtain a good signal to noise ratio. The induced transient temperature rise, which leads to an intensity decrease is the measure of the temporal overlap, that is, when x-rays and laser pulses arrive simultaneously at the same sample position. This procedure yields accurate values for t_0 only because the sample response to the photoexcitation at room temperature occurs quasi-instantaneously, much faster than the experimental time-resolution of 80 ps [24].

After this adjustment and optimization procedure, it is now possible to measure the out-of-plane lattice constant c at each delay t between laser and x-ray pulses. Consequently, the transient lattice strain

$\epsilon(t)$ is defined by

$$\varepsilon(t) = \frac{c(t) - c(t < 0)}{c(t < 0)} = \frac{\Delta c}{c} \ . \tag{4.3}$$

4.2. Results: dysprosium

In this section, the static and time-resolved results of the UXRD experiments on the Dy samples I and II introduced in figure 4.3) are presented. In sample I, only the Dy layer is investigated in the AFM phase in order to study the interaction of the magnetic and phonon systems after the ultrafast photoexcitation. The coupling between these two subsystems results in a pronounced magnetostriction that is observed in the measured static and transient lattice strain. For sample II, the static and dynamical responses of all metal layers are simultaneously measured in the temperature range of the AFM state of Dy using the advantage of large penetration depth of the hard x-rays. This yields a layer-specific measurement of the transient temperatures after photoexcitation and hence allows to study the heat transport through the nanolayers.

4.2.1. Static characterization

The equilibrium lattice constants of Dy in sample I and Y, Dy, and Nb in sample II were measured as function of temperature. During the static experiments the sample temperature is varied between 20 K and 270 K and the Bragg peak of each layer is measured in order to extract the lattice constants and the peak widths.

Figure 4.9.a shows the measured out-of-plane lattice constant as inferred from the 0002 reflection of Y and the 220 reflection of Nb from sample II as function of temperature. The measured Bragg peaks of Y consist of contributions from the top and bottom Y layers. The monotonous increase of the lattice constant with increasing temperature is typical for the materials with only electronic and phononic degrees of freedom. On the contrary, the out-of-plane lattice constant deduced from the 0002 reflection of Dy exhibits pronounced characteristic anomalies due to the magnetic phase transitions. In figure 4.9.b the results for sample I and II are plotted together where the lattice constants for sample I are shifted by 0.063 $\AA$. The phase transition from the FM to the AFM state occurs around $T = 50$ K and is characterized by a discontinuous decrease of the lattice constant around the phase transition temperature. After a slow and subsequent cooling cycle of the sample, a hysteresis becomes visible, which is a signature of the first order nature of the FM to AFM phase transition [44]. In the temperature range of the AFM phase, the lattice contracts with increasing temperature up to T_N, which is observed in these samples around 180 K. In the PM phase, the lattice expands again, thus, it indicates the absence of magnetic order and only the existence of the the phononic and electronic degrees of freedom, similarly as in non-magnetic Y and Nb.

The width, w, of the structural Bragg peak of Dy has an interesting temperature-dependence that is shown in figure 4.10.a. It is important to note that the peak widths of Y and Nb exhibit no significant temperature-dependencies. The peak width of Dy increases close to the phase transition temperatures

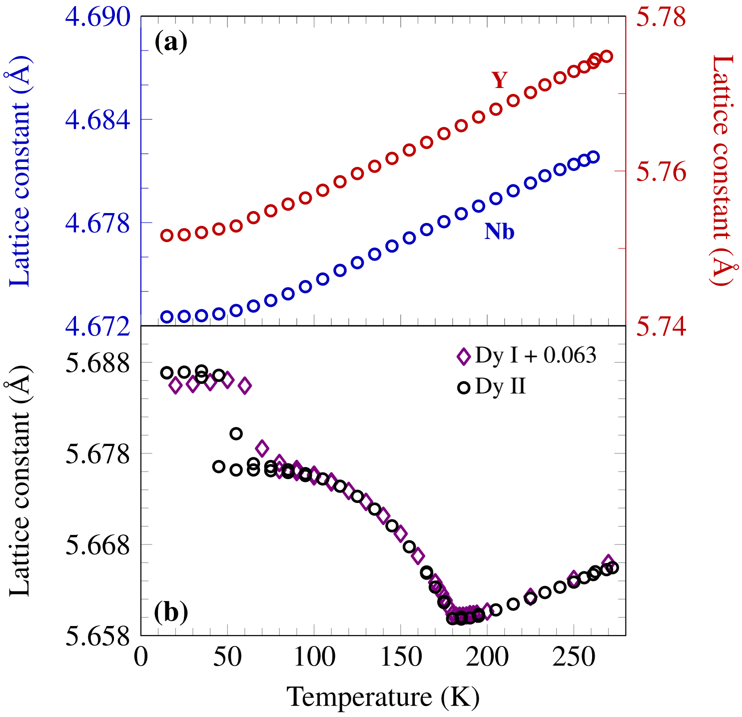

Figure 4.9.: Temperature-dependent out-of-plane lattice constants deduced from a) 0002 reflection of Y and 220 reflection of Nb in sample II and b) 0002 reflection of Dy. Dy I and Dy II denote the layers in sample I and II, respectively.

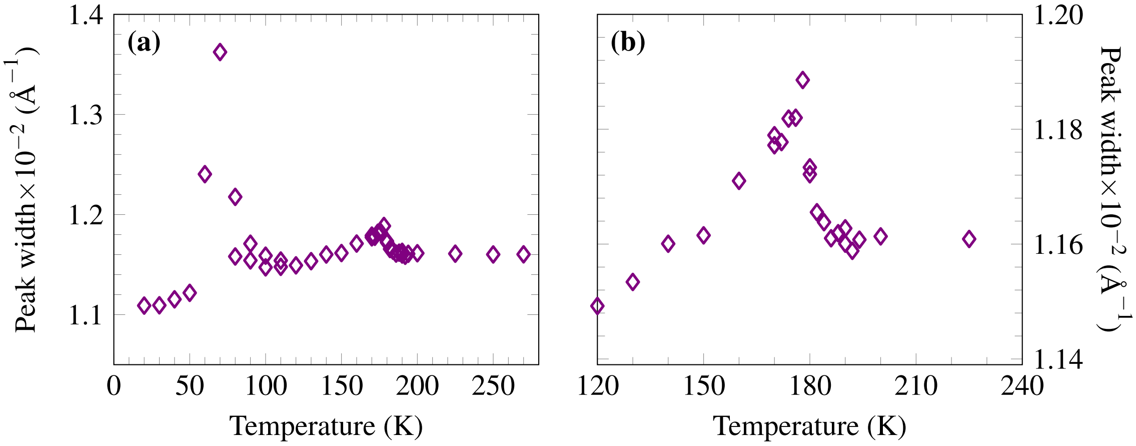

Figure 4.10.: a) The peak width of the structural Bragg peak of Dy as function of temperature in thermal equilibrium. b) The peak width in a) is shown in the AFM phase and at the phase transition from the AFM to the PM phase.

T_C and T_N. Interestingly, the rapid change at the first order phase transition from the FM to the AFM phase is more pronounced than the increase close to T_N where the second order transition from the AFM to the PM state occurs. In addition, it seems that w increases continuously in the AFM phase as T_N

is approached, which is visible in the magnified view in figure 4.10.b. Above T_N, w decreases again and remains constant in the PM phase. This interesting temperature-dependence of the peak width in equilibrium can likely be attributed to the formation of the magnetic domains. As already discussed in section 2.2, the magnetic structure is strongly correlated with the lattice due to the magnetostriction in the rare-earth metals. At a first order phase transition, the spontaneous formation of domains, the so-called droplets of co-existing phases at the phase transition, is predicted [92]. Thus, the spontaneous increase of the peak width at the FM to the AFM phase transition can be related to this structural inhomogeneity. The hysteresis feature observed in the measurements of the lattice constant (see figure 4.9.b) justifies this scenario. On the contrary, for a continuous second order phase transition, the formation of big domains is shown theoretically to occur as the phase transition temperature is approached from the disordered phase [103]. If the temperature is slowly moved away from the phase transition, the domains are getting smaller, which is exactly the behavior that the temperature-dependent value of w shows at T_N of the AFM to the PM phase transition.

4.2.1.1. Thermal expansion coefficient of antiferromagnetic dysprosium

Thermal expansion coefficient, α, of a solid is the consequence of the anharmonic effects of the potential lattice energy that is given in one dimension by [36]

$$\alpha = \frac{1}{c}\frac{dc}{dT} \ , \tag{4.4}$$

where c is the lattice constant. Using the temperature-dependencies of the measured lattice constants shown in figure 4.9.a and b, the linear thermal expansion coefficients of Y, Dy and Nb are derived and shown in figure 4.11.a. Non-magnetic Y and Nb exhibit a nearly constant thermal expansion coefficient in this temperature range that resembles the heat capacity as function of T. On the other hand, for the antiferromagnetic Dy, α is negative in the AFM phase and around T_N additionally exhibits a strong temperature-dependence with a peak around T_N. The measured expansion coeffient of Dy, $\alpha_\mathrm{Dy} = \alpha_{ph} + \alpha_m$, can be separated into the phonon and magnetic contributions using a theoretical decomposition of the thermal expansion coefficient in the Heisenberg ferromagnets in reference [133]:

$$\alpha = \alpha_{ph} + \alpha_m = \frac{1}{9}\frac{1}{c^2 K}\left(\frac{3\Gamma_{ph}}{c}C_{ph} + \frac{1}{\mathscr{J}}\frac{\partial \mathscr{J}}{\partial c}C_m\right) \ , \tag{4.5}$$

where K is the effective elastic constant, and Γ the Grueneisen coefficients of the materials [133]. The first term in the brackets describes the non-magnetic materials and is derived from anharmonic effects of the ionic potential energy. The second term gives the magnetic contribution and explains the negative thermal expansion with a peak around the second order phase transition by the negative exchange interaction derived from the Heisenberg energy [133]. The decomposition of α_Dy then is performed by assuming α_{ph} to be equal to the measured α_Dy in the PM phase far from T_N where no magnetic order exists. The magnetic contribution is extracted by simply subtracting the extrapolated phonon contribution from the measured expansion coefficients [66, 123] that are shown in figure 4.11.a with the dashed

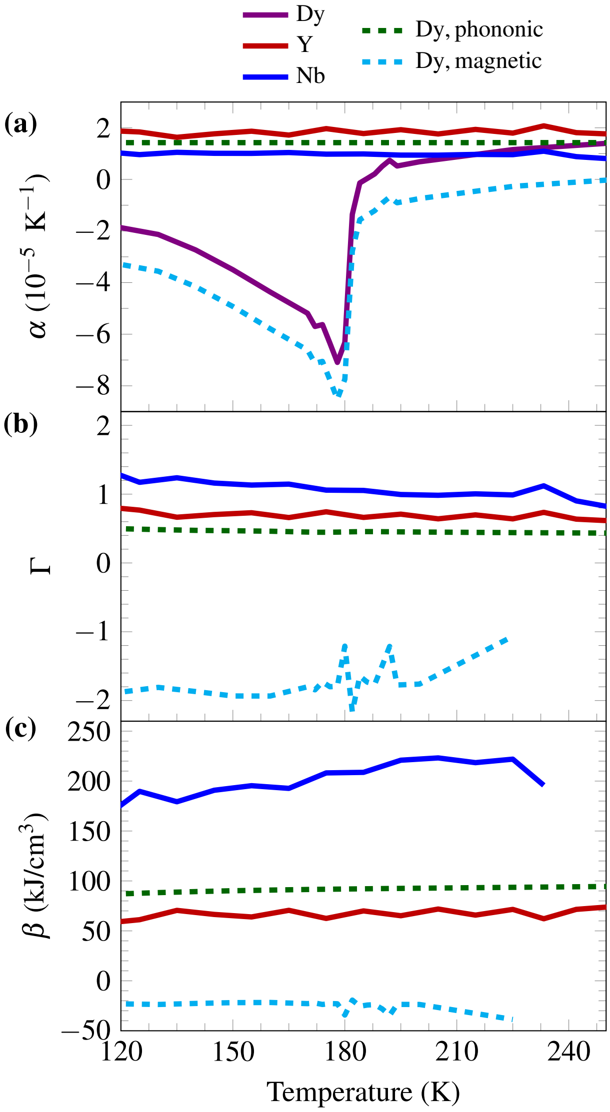

Figure 4.11.: a) The linear thermal expansion coefficients, α, b) macroscopic Grueneisen coefficients, Γ, and c) β constants of Y, Dy and Nb as function of temperature. Dashed lines indicate the contribution of the phonon and the magnetic systems in Dy (see text).

lines. One can immediately see that α_{ph} and α_m vary strongly with T and also resemble the temperature-dependencies of the individual heat capacities C_{ph} and C_m (see figure 2.10) as equation 4.5 suggests. α_m above T_{N} is not immediately going to zero, which indicates the influence of the magnetic system on the strain with the short-range order.

Additional material parameters can be derived using the results of the static measurements and the resulting thermal expansion coefficients. The macroscopic Grueneisen coefficient, Γ, is a dimensionless quantity and nearly independent of the temperature for the phonon system. For Y and Nb, Γ is calculated by the relation

$$\Gamma = \frac{\alpha(T)K}{C(T)} \tag{4.6}$$

with the temperature-dependent heat capacity $C(T)$. The decomposition of Γ_{Dy} into the phonon and magnetic contributions, Γ_{ph} and Γ_m, uses the already separated thermal expansion coefficients and heat capcities $\alpha_{\mathrm{Dy}} = \alpha_{ph} + \alpha_m$ and $C_{\mathrm{Dy}} = C_{ph} + C_m$. Figure 4.11.b depicts the macroscopic Grueneisen coefficients obtained using equation 4.6 for the different subsystems. For the calculation of the Grueneisen coefficients, the heat capacities of Y and Nb are taken from references [66, 69]. The effective elastic constant K is calculated using the elastic constants from references [134–136]. As can be seen in figure 4.11.b, the phononic Grueneisen coefficient of Dy is practically temperature-independent in the relevant temperature range, the same is true for the coefficients for Y and Nb and the obtained average values are $\Gamma_{ph} = 0.46$, $\Gamma_{\mathrm{Y}} = 0.67$, and $\Gamma_{\mathrm{Nb}} = 1.08$. The magnetic Grueneisen coefficient of Dy is negative and also quasi-independent of temperature and the average value of $\Gamma_m = -1.83$ is found, which is approximately 4 times larger than Γ_{ph}. This shows that the excitation of the magnetic system more efficiently generates stress in the material compared to an excitation of the phonon system with the same energy density.

For the simplification of the further analysis of the time-resolved data, another temperature-independent parameter β is defined, which relates to the Grueneisen coefficient by

$$\beta = \frac{C(T)}{\alpha(T)} = \frac{K}{\Gamma} \ . \tag{4.7}$$

In figure 4.11.c the parameter β for Y, Nb, and phonon and magnetic contributions of Dy is plotted as function of temperature.

4.2.2. Structural dynamics in the antiferromagnetic phase

In this section, the time-resolved results of the structural Bragg peak dynamics of Dy in sample I are presented where the pump laser excites the Dy layer directly. Despite a 10 nm Y layer on the top, the penetration depth of 30 nm of the pump light results in an effective excitation of Dy. The measurements were performed with delays up to 200 ns after the ultrafast photoexcitation and the start temperature was varied between 136 K and 301.5 K. The transient strain is measured at the two incident fluences of $F_i = 0.7\,\mathrm{mJ/cm^2}$ and $F_i = 2\,\mathrm{mJ/cm^2}$. For the given start temperatures, a static temperature increase due to the laser excitation of 51.5 K for the fluence of $2\,\mathrm{mJ/cm^2}$ (11 K at $0.7\,\mathrm{mJ/cm^2}$) are already added. This temperature rise is determined from static measurements with the same incident fluence conditions.

Figure 4.12.a depicts the transient strain $\varepsilon_{\mathrm{Dy}}(t)$ in directly excited Dy at $F_i = 2\,\mathrm{mJ/cm^2}$ for different start temperatures. At $T = 301.5\,\mathrm{K}$, the lattice expands within the time-resolution of 80 ps as expected for a system where only the phonon system is heated. The relaxation to its half of the initial value occurs after 0.7 ns by heat diffusion through the layers into the substrate. At the temperatures below T_{N},

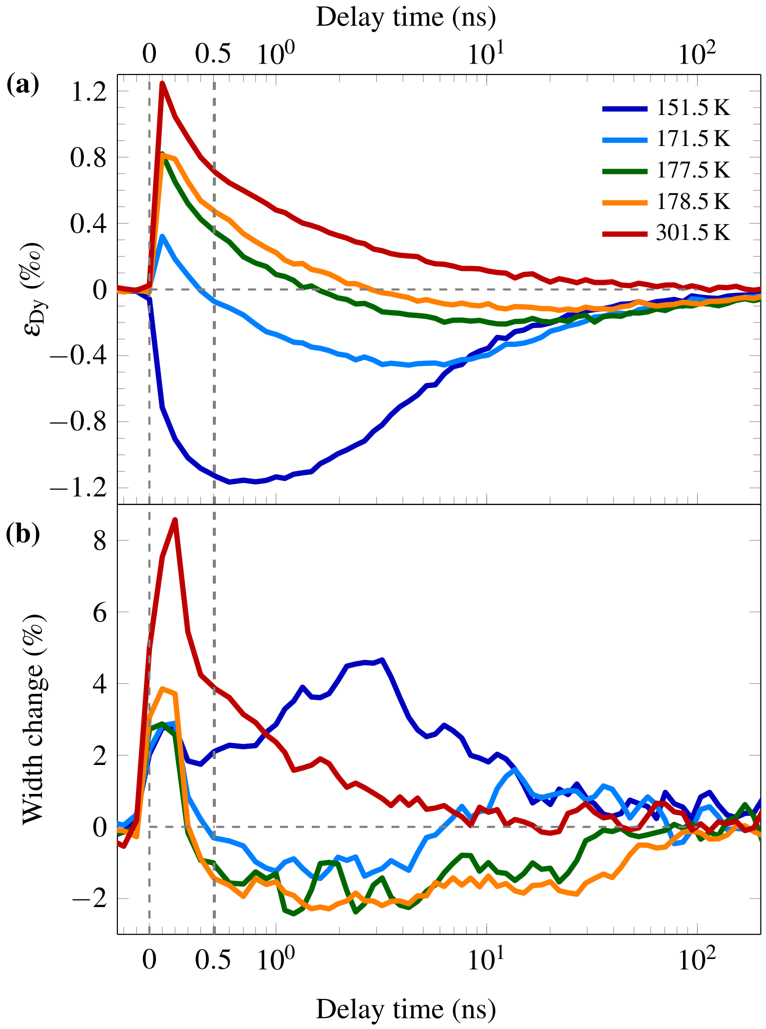

Figure 4.12.: Temperature-dependence of the structural dynamics in directly excited Dy in sample I after the ultrafast photoexcitation with an incident fluence of $F_i = 2\,\mathrm{mJ/cm^2}$. a) The transient strain and b) the peak width change of the structural 0002 Bragg peak of Dy are displayed for five start temperatures. Note that the x-axis is split into a linear and a logarithmic part. The dashed gray lines indicate $t = 0$, $\varepsilon = 0$, and the time where the x-axis is split into the linear and logarithmic scales at 0.5 ns.

different dynamics are observed, strongly dependent on the start temperature. At $T = 151.5$ K, the lattice contracts due to the negative thermal expansion coefficient driven by the antiferromagnetic order. The contraction in the AFM state emphasizes the strong coupling between the lattice strain and spin order due to exchange magnetostriction. However, the contraction is not instantaneous and reaches a minimum after approximately 0.8 ns. As the start temperature approaches T_{N}, the lattice expands at early times and contracts at later times. At these temperatures, the initial expansion and the subsequent contraction is reduced. On the other hand, the transient strain dynamics slow down and the time at which the minima occur depends on the start temperature. In addition to this, the minima become more and more extended as T approaches T_{N}.

In figure 4.12.b, the peak width change of the Bragg peak of Dy is shown. The plotted data are smoothed over three data points in order to improve the signal-to-noise ratio. At all start temperatures, an instantanenous increase of the peak width is observed within the time-resolution of the experiment. This initial increase is associated with a strain wave that is generated at the sample surface and propagates through the film. Although the sound wave propagation takes less than 0.1 ns [24], the peak width is still broader at $T = 301.5\,\mathrm{K}$ and reduced to half of its initial value only after 0.5 ns. This delay might be caused by an inhomogeneous heat distribution in the phonon system in Dy layer. The initial increase of the peak width is not the same for all temperatures as a reduced increase is observed with increasing temperature although the initially deposited energy is expected to be temperature-independent because the optical constants of the sample do not change in this temperature range. For the start temperatures close to T_{N}, the peak width is reduced and remains essentially constant. At temperatures far below T_{N}, for example for $T = 151.5\,\mathrm{K}$, the peak narrowing is not observed, even on the contrary, the peak width increases. From the temperature-dependence of the peak width change in thermal equilibrium shown in figure 4.10.b, a peak broadening is indeed expected for the excitation of the magnetic system to a temperature below T_{N}. This might be the case for the start temperature 151.5 K. In contrast, a peak narrowing is possible after the magnetic order is destroyed by excitation into the PM phase. This is consistent with the observed static 2% change of the peak width between 178.5 K and in the PM phase. Another interesting experimental result is that the time after which the peak width recovers to the initial value coincides with the time at which the minima of the lattice strain for temperatures close to T_{N} are observed. The transient strain at fluence $F_i = 0.7\,\mathrm{mJ/cm^2}$ is presented in figure A.1 in the appendix.

These results directly indicate that different amounts of the initial deposited energy by ultrafast laser pulses are distributed into the phonon and magnetic systems. In particular, the initial rise of the transient strain and peak width change depend strongly on the start temperature. Using the equilibrium measurements, one can simply show that the laser heating leads to a strong non-equilibrium between phonon and the magnetic systems. It is possible to estimate the sample temperature in the quasi-equilibrium conditions after the laser excitation by taking the experimentally measured strain. In figure 4.13, this is exemplarily shown for three start temperatures $T = 301.5\,\mathrm{K}$, $T = 171.5\,\mathrm{K}$ and $T = 151.5\,\mathrm{K}$. From the start temperature a horizontal arrow indicates the temperature increase that has to be balanced by the vertical arrow, which is the experimentally determined strain at, for example, $t = 0.1$ ns. From the graph 4.13 one can draw the following conclusions:

i) 301.5 K is far above T_{N} and no magnetic effects affect the lattice expansion in Dy, hence, it reveals the total energy density deposited in Dy at $F_i = 2\,\mathrm{mJ/cm^2}$. At this temperature, an initial strain of $1.24 \cdot 10^{-3}$ corresponds to the temperature change of $\Delta T = 85\,\mathrm{K}$ in thermal equilibrium shown in figure 4.12 by the red arrows. The deposited energy density $\Delta\rho^{Q}_{\mathrm{tot}} \approx 118\,\mathrm{J/cm^3}$ is given by equation 2.14 after integrating the heat capacity over the temperature change. Since the optical absorption of the pump pulse does not change with temperature, this total amount of heat $\Delta\rho^{Q}_{\mathrm{tot}}$ deposited should be the same for all starting temperatures.

ii) At 171.5 K close to T_{N}, the initial lattice expansion of around $3.2 \cdot 10^{-4}$ corresponds to a temperature increase of $\Delta T = 90\,\mathrm{K}$ (see light blue line in figure 4.13). This corresponds to an energy density of $\Delta\rho^Q \approx 153\,\mathrm{J/cm^3} > \Delta\rho^Q_{\mathrm{tot}}$ considering the equilibrium properties. This can not be the case, because the sample reflectivity is essentially temperature-independent.

iii) At 151.5 K well below T_N, an initial negative expansion of $7.2 \cdot 10^{-4}$ is measured. The transient peak width change indicates that the system is excited to a temperature below T_N. This results in a temperature change of $\Delta T = 15\,\mathrm{K}$ corresponding to $\Delta\rho^Q \ll \Delta\rho^Q_{\mathrm{tot}}$. Even the maximal negative expansion $\varepsilon(t = 0.6\,\mathrm{ns}) = 1.17 \cdot 10^{-3}$ only corresponds to a $\Delta T = 23\,\mathrm{K}$, which also requires much less energy density compared to the total energy density deposited in the Dy layer according to the measurement at 301.5 K discussed under i).

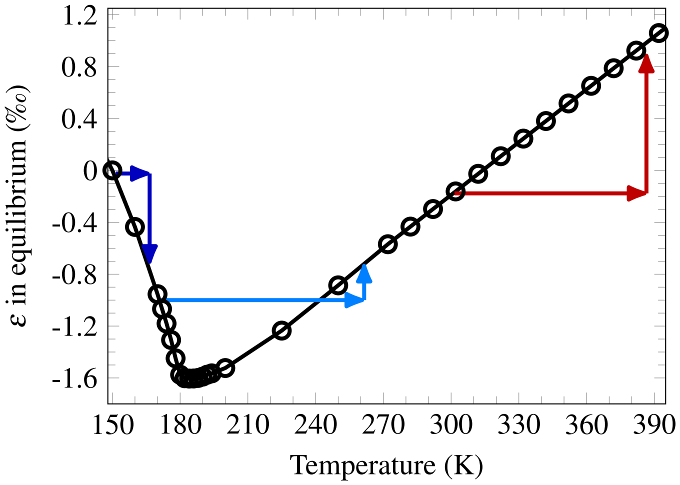

Figure 4.13.: Strain as function of temperature for Dy in thermal equilibrium. For three start temperatures, the temperature increase (horizontal arrows) is determined by the experimentally observed transient strain in quasi-equilibrium at $t = 0.1$ ns (vertical arrows).

These examples clearly show the non-equilibrium of the magnetic and phonon systems. A quantitative decomposition of the deposited energy densities into each subsystem and also the resulting individual transient temperature changes can be calculated with the two-thermal-energies-model (TTEM) [24, 122, 123].

4.2.2.1. Non-equilibrium of the transient magnetic and phonon energies

The TTEM assumes that the initial total energy density $\Delta\rho^Q_{tot}$, which is supplied by the ultrafast laser heating, is distributed between the phonon and the magnetic systems. $\Delta\rho^Q_{tot}$ is derived from the measurement at 301.5 K because the temperature is far above T_N and the magnetic order is absent. Additionally, the measured strain $\varepsilon_{\mathrm{Dy}}$ is a superposition of the positive strain driven by phonon excitations and negative strain by magnetic excitations as a result of the deposited individual energy densities, which is summarized by the following set of equations:

$$\Delta\rho^{Q}_{tot} = \Delta\rho^{Q}_{ph} + \Delta\rho^{Q}_{m} \tag{4.8}$$

$$\varepsilon_{\mathrm{Dy}} = \varepsilon_{ph}(\Delta\rho^{Q}_{ph}) + \varepsilon_{m}(\Delta\rho^{Q}_{m}) \ . \tag{4.9}$$

Note that the electronic contribution is included in the phonon system because the electron-phonon thermalization time is typically on the order of a few picoseconds for metals [81, 82]. This model is only applicable for the time scale that is smaller than the heat propagation in-plane because the laser spot size is large compared to the thickness of the layer. This time scale is also longer for the sound propagation through the layers. Therefore, Hooke's law, which relates linearly stress and strain in a solid by $\sigma = K\varepsilon$, is valid and the Grueneisen coefficient defined in equation 4.6 measures how efficiently the deposited energy density is transformed into stress, $\sigma = \Gamma\Delta\rho^{Q}$. The relation of the strain and the deposited energy density for the subsystem i can be written as

$$\Delta\rho^{Q}_{i} = \frac{K\varepsilon_i}{\Gamma_i} = \beta_i\,\varepsilon_i \ . \tag{4.10}$$

It is important to note that the relation between energy density and strain is linearly given by β, which is temperature-independent as shown in figure 4.11.c.

In order to calculate the energy densities deposited into the phonon and magnetic systems and also the resulting strains in each subsystem separately, the equations 4.8, 4.9 and 4.10 are combined and one obtains

$$\Delta\rho^{Q}_{tot} = \beta_{ph}(\varepsilon_{\mathrm{Dy}} - \varepsilon_m) + \beta_m\,\varepsilon_m \ , \tag{4.11}$$

which allows to extract ε_m and finally $\Delta\rho^{Q}_{m}$, ε_{ph} and $\Delta\rho^{Q}_{ph}$ can be derived analytically. One needs to emphasize here that the energy densities and the resulting strain exhibit a spatial distribution over the layer thickness. The results shown here are averaged over the complete Dy layer.

In figure 4.14.a the transient energy densities of the phonon and magnetic subsystems for different start temperatures are plotted. These results clearly show the different distribution of the initial energy density because initially always $\Delta\rho^{Q}_{ph} > \Delta\rho^{Q}_{m}$ is observed. At $T = 151.5\,\mathrm{K}$ the magnetic system receives 27% of the total energy and this value is decreased to 6% at $T = 178.5\,\mathrm{K}$. The rest of the energy is deposited into the phonon system. This shows that as T approaches T_{N}, the initial energy density in the magnetic system is reduced and the energy of the phonon system increases as can be seen in the inset of figure 4.14.a. The transient strains of the subsystems are shown in figure 4.14.b. This analysis supports that the energy deposited into the magnetic system is more efficiently converted into strain, which is particularly visible for the data obtained $T = 151.5\,\mathrm{K}$ although $\Delta\rho^{Q}_{m}$ is much less than $\Delta\rho^{Q}_{ph}$. This is also in agreement with the calculated Grueneisen coefficients $\Gamma_m \approx 4 \cdot \Gamma_{ph}$. Additionally, one can easily see that the magnetic strain resides unchanged at the temperatures close to T_{N} and the phononic strain relaxes on a much faster time scale.

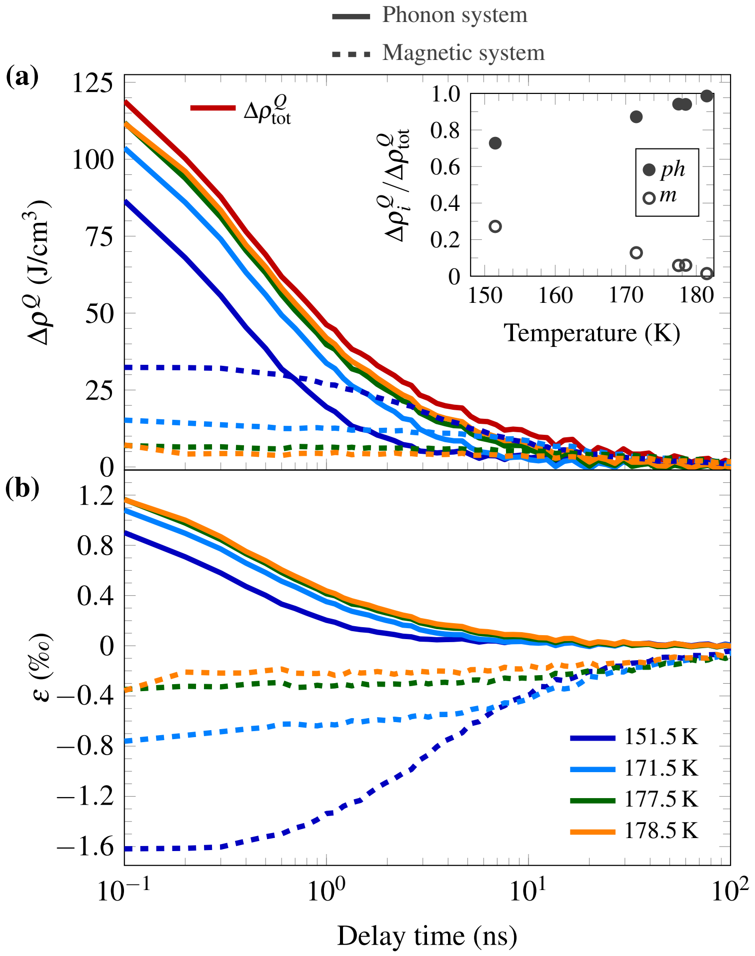

Figure 4.14.: The results of the TTEM analysis of the transient strain of Dy after the ultrafast laser heating with $F_i = 2\,\mathrm{mJ/cm^2}$. a) The transient energy densities deposited into the phonon and magnetic subsystems for different start temperatures. In the inset: The fraction of the initial energy density into each subsystem i as function of the temperature. b) The resulting strain by the deposited energy density for each subsystem shown in a). The solid and dashed lines denote the phonon and magnetic systems, respectively.

The interaction between the different subsystems and also the heat transport is given by the individual temperatures of each subsystem in a material as explained in section 2.3. Therefore, the converted temperature changes of the phonon and magnetic systems are shown in figure 4.15, which are obtained with equation 2.14 for each subsystem from the individual energy densities shown in figure 4.14.a and the heat capacities shown in figure 2.10. The extracted temperature changes show at the beginning always $\Delta T_{ph} > \Delta T_m$ as also expected by the three-temperature-model in figure 2.13. The phonon system cools much faster than the magnetic system, which is related to the fact that the adjacent metal layers are non-magnetic. Thus, the phonon system can release energy via phonon diffusion to the other layers but the magnetic system has no available channel to transport the deposited energy. Interestingly, for later times than the equilibration time, $t > t_{eq}$ on which $\Delta T_{ph} = \Delta T_m$ occurs, the magnetic system starts

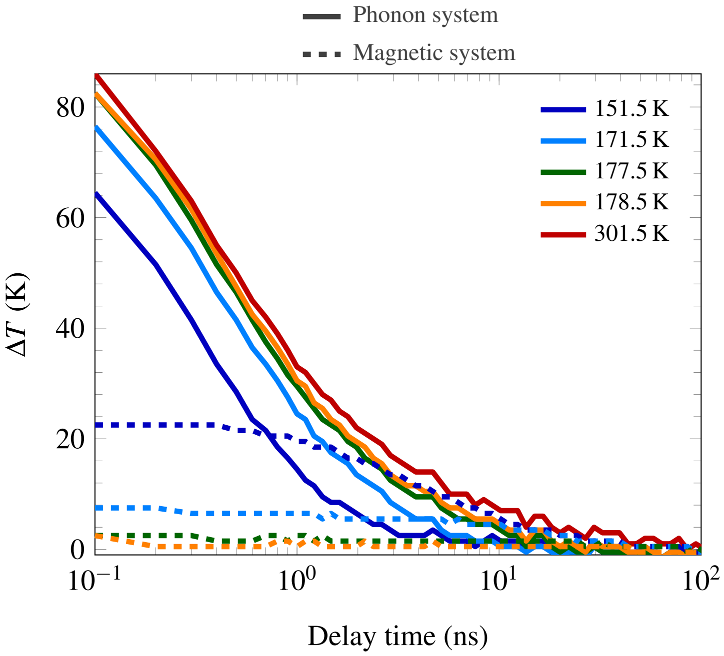

Figure 4.15.: The transient temperature change ΔT of the phonon and the magnetic systems in Dy after ultrafast laser heating with $F_i = 2\,\mathrm{mJ/cm^2}$ for different start temperatures. ΔT is derived from the individual energy densities calculated via the TTEM.

to cool by energy transfer into the phonon system because now $\Delta T_{ph} < \Delta T_m$ allows the heat transport. This behavior is observed for each start temperature. Additionally, the recovery time of the magnetic system significantly increases for the temperatures close to T_N and therefore the equilibration occurs at very late times. This is caused by the initial distribution of the energy densities just after absorption of the pump pulse: Close to T_N the energy deposited into the phonon system is more and therefore the relaxation takes longer, as the magnetic system can only cool after the lattice temperature falls below the spin temperature. For the start temperatures close to T_N, the equilibration time t_{eq} corresponds within the experimental uncertainty to the time on which the peak width starts to broaden again and also when the minima of the measured transient strain ε_{Dy} are observed in figure 4.12. For example one sees at 171.5 K that $t_{eq} \approx 5$ ns and $\Delta T \approx 6$ K. It is important to note here that the cooling rate of the phonon system is likely to be different for $t > t_{eq}$, because now the phonon subsystem receives additional energy from the magnetic system. This results in a slightly different temperature change of both subsystems given by the TTEM for $t > t_{eq}$.

These experimental results and the analysis show clearly that a non-equilibrium between the phonon and magnetic systems in Dy exists after the direct excitation of Dy by ultrafast laser heating.

4.2.3. Influence of magnetic excitations on the heat transport through nanolayers[1]

In this section, the heat transport through the metal layers in sample II (see figure 4.3) is investigated as an example of a complex heat flow problem on the nanoscale, where several different quasiparticles transport the heat. The structural Bragg peak positions of each layer represent layer-specific thermometers that measure the energy flow through the sample after excitation of the Y top layer with a laser fluence of $F_i = 2\,\mathrm{mJ/cm^2}$. The excitation depth of 32 nm is determined by ellipsometry studies. The measurements were performed with delays up to 100 ns after the ultrafast laser heating and the start temperature T is varied from 136 K through T_N up to 276 K. The static temperature increase due to the laser excitation of 26 K for the fluence of $2\,\mathrm{mJ/cm^2}$ is already included for the given start temperatures.

In figure 4.16.a, the transient strain of both Y layers as the average of the upper and bottom Y layer is shown for different start temperatures T. At 276 K the laser-heated Y layer shows a maximum expansion within the time-resolution limit given by the pulse duration of the x-rays at the beamline. It relaxes by the heat diffusion into the other adjacent thin layers. At lower T the identical dynamics are observed, however, the maximal strain value decreases with decreasing T. The transient strain of the indirectly heated Dy layer is shown in figure 4.16.b together with the simulated average strain $\varepsilon^{av}_{\mathrm{Dy}}(t)$ by the one dimensional heat diffusion equation 2.22 using the UDKM1Dsim toolbox [137]. The transient strain of Dy shows very different dynamics depending on the start temperature. At 276 K the paramagnetic Dy layer expands and reaches the maximal expansion after about 300 ps. In the AFM phase below T_N the Dy layer contracts upon heating, which is driven by the excitation of the magnetic system. The simulated strain of Dy is not in agreement with the measured strain because the different contributions of the magnetic excitations and phonons are not considered by this simulation. The transient strain in the Nb layer is depicted in figure 4.16.c. The maximal expansion of the Nb layer at $T = 276\,\mathrm{K}$ is observed at about 1.8 ns. At lower start temperatures the maximal expansion shifts to larger time delays and the magnitude of the maximal expansion is reduced. The inhomogeneous spatial heat distribution in the three materials not only changes the Bragg peak positions but also the Bragg peak width (see figure A.2 in the appendix). For Dy, a maximum peak width increase of 8% is observed in the first 100 ps when strain waves propagate from the surface through the film. The inhomogeneous thermal strain in Dy increases the peak width by less than 4%. In the Y layer the peak width change is more pronounced since the strongly excited layer above Dy contributes equally to the signal as the layer below Dy, which is almost not excited. Here the peak width increase rapidly decreases from 30% to 8% within 400 ps. In Nb, the initial peak width increase is always less than 2%.

The analysis of the measured transient strain of each layer provides the determination of layer-specific temperature changes. The change of the integral heat in subsystem i

$$\Delta Q_i = V_i \cdot \Delta\rho_i^Q = V_i \beta_i \varepsilon_i \tag{4.12}$$

in the volume V_i of a system is proportional to the lattice strain ε_i. At temperatures above T_N, the

---

[1] This section essentially follows my publication [122], therefore a large fraction of the section is identical to the publication.

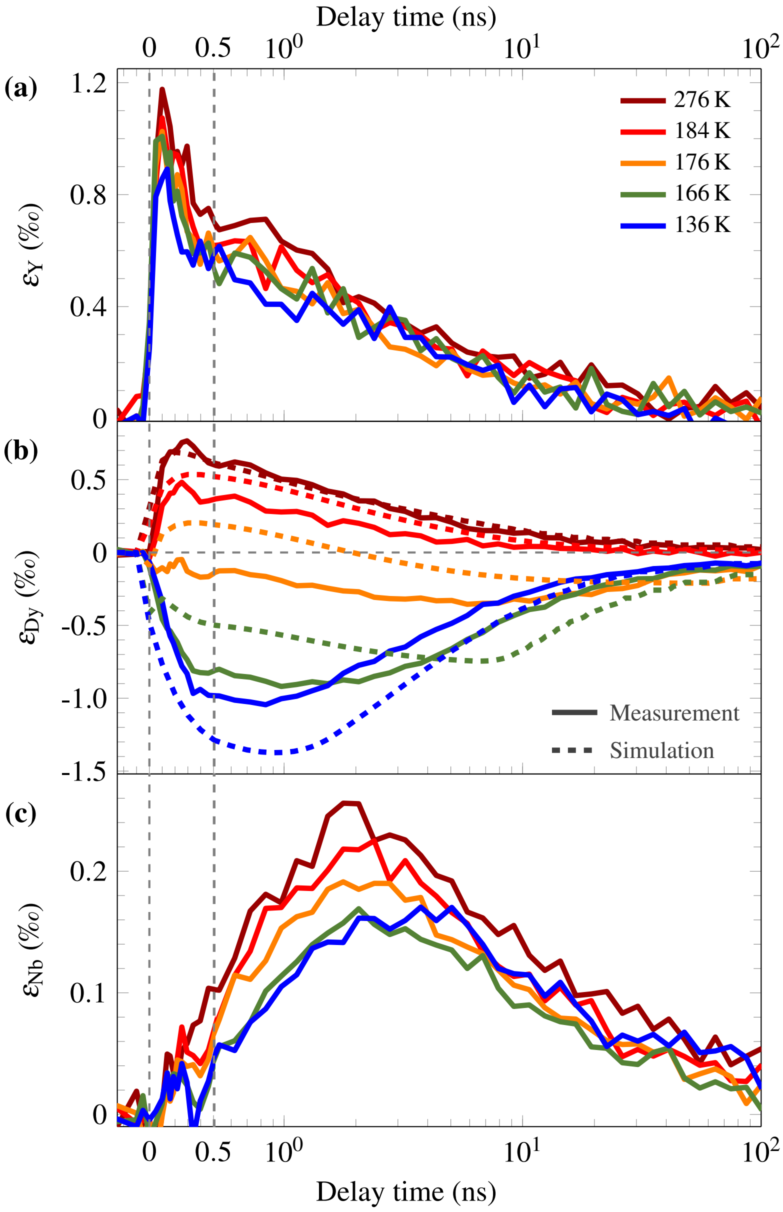

Figure 4.16.: Transient strain $\varepsilon(t)$ for different initial temperatures T after ultrafast laser heating with the fluence of $F_i = 2\,\mathrm{mJ/cm}^2$: Solid lines depict the measured transient strain of a) the two Y layers, b) the Dy layer, and (c) the Nb layer. The dashed lines in panel b) represent the unsuccessful attempt to simulate the strain $\varepsilon^{av}_{\mathrm{Dy}}(t)$ by the heat transport equation without taking into account the fact that the magnetic excitations and phonons contribute to the heat transport and the strain.

increase of the energy densities $\Delta\rho^{Q}_{\mathrm{Y,Dy,Nb}}$ in Y, Dy, and Nb can be directly found from equation 4.12. The temperature-independent β values are taken from figure 4.11.c. Essentially, the energy density of excited phonons in each material drives the lattice expansion since the electrons carry a negligible fraction of the specific heat when the electrons have cooled to approximately the lattice temperature. Thus, the electron and phonon contributions are not taken into account separately. In contrast, the specific heat of the magnetic system below T_N is very large. Below T_N four heat carrying degrees of freedom in the system coexist, namely the magnetic excitations in Dy and the phonon excitation in Dy, Nb, and Y. In addition to the three measured transient lattice strains $\varepsilon_\mathrm{Y,Dy,Nb}$ shown in figure 4.16, a fourth equation is required in order to find the solution to the heat transport problem. The temperature-dependent ellipsometry measurements prove that the absorbed energy density of the multilayer does not change considerably with temperature, because the sample reflectivity does not change with T in this range. Assuming that no substantial fraction of the initial heat is transported to the substrate, one can identify the total amount of energy deposited in the multilayer at any temperature ΔQ^T_{tot} with the value $\Delta Q^{276\,\mathrm{K}}_{tot}$ that drives the Dy expansion. This is measurement at $T = 276$ K is a good approximation for high temperatures, where only phonons contribute and time scales up to 100 ns because the heat transport into the sapphire substrate is similar at all temperatures. When one writes

$$\Delta Q^T_\mathrm{Dy} = \Delta Q^{276\,\mathrm{K}}_{tot} - \Delta Q^T_\mathrm{Y} - \Delta Q^T_\mathrm{Nb} \ , \tag{4.13}$$

only ΔQ^T_Dy at low temperatures is overestimated by the rather small fraction $\Delta Q^T_{err} = \Delta Q^T_{tot} - \Delta Q^{276\,\mathrm{K}}_{tot}$ of heat that is transported into the substrate more than it would be transported at 276 K. For convenience, this error can be identified by the difference of dark red and blue lines in figure 4.17.b where the total energy Q transported into substrate is used in order to calculate a change of energy density $\Delta\rho^Q$ that has left a 100 nm thick layer. The energy densities $\Delta\rho^Q_\mathrm{Dy} = \Delta Q^T_\mathrm{Dy}/V_\mathrm{Dy}$ in Dy derived for several different start temperatures are plotted in figure 4.17.a. This shows that with lower start temperature a larger and larger fraction of the energy is rapidly transferred from the excited Y layer into Dy.

In order to determine the individual contributions of magnetic and phononic system to the energy density and expansion of Dy at temperatures below T_N, the two-thermal-energies-model is used as described in the previous section. One can combine equations 4.8 and 4.9 to

$$\Delta\rho^Q_\mathrm{Dy} = \beta_{ph}(\varepsilon_\mathrm{Dy} - \varepsilon_m) + \beta_m \varepsilon_m \ . \tag{4.14}$$

Here, $\Delta\rho^Q_\mathrm{Dy}$ is the experimentally determined energy density plotted in figure 4.17.a for each start temperature. By solving this equation, the following equations are obtained for the contractive strain ε_m driven by magnetic order and the phonon-driven expansive strain ε_{ph} that only depend on measured quantities:

$$\varepsilon_m = \frac{(\Delta\rho^Q_\mathrm{Dy} - \beta_{ph}\varepsilon_\mathrm{Dy})}{(\beta_m - \beta_{ph})} \tag{4.15}$$

$$\varepsilon_{ph} = \varepsilon_\mathrm{Dy} - \varepsilon_m \ . \tag{4.16}$$

Now together with equation 4.12 the contributions to the time-dependent energy densities $\Delta\rho^Q_{m,ph}$ in Dy can be calculated. The corresponding energy densities $\Delta\rho^Q_\mathrm{Y,Nb}$ of the adjacent layers are determined directly from the measured quantities $\varepsilon_\mathrm{Y,Nb}$. The resulting energy densities in each material derived from the experiment are plotted in figure 4.17.c and compared to a simple calculation of the heat trans-

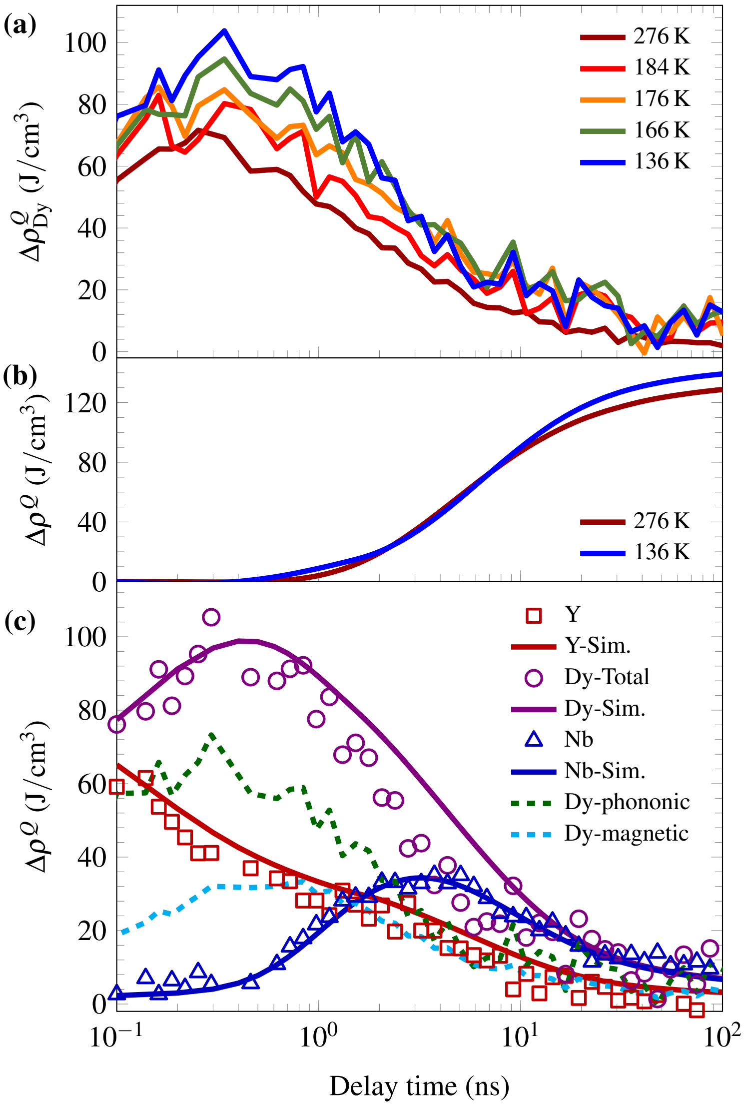

Figure 4.17.: a) Transient increase of the energy density in the Dy layer $\Delta\rho^Q_{\mathrm{Dy}}$ after optical excitation derived from the measurement according to equation 4.13. b) Simulation of the energy density transported into the substrate according to the heat transport equation. c) Symbols show the experimentally determined transient energy densities $\Delta\rho^Q_{\mathrm{Y,Dy,Nb}}$ in each material. Solid lines represent simulations according to heat equation. Dotted lines show the experimentally derived energy densities in the magnetic and phonon system of Dy $\Delta\rho^Q_{m,ph}$.

port according to the heat transport equation [137]. Assuming a small thermal interface resistance of 200 MW/m^{2}K only between Nb and sapphire, a very good simultaneous agreement of the experimentally derived total energy density in Dy $\Delta\rho^Q_{\mathrm{Dy}} = \Delta\rho^Q_{ph} + \Delta\rho^Q_m$ and the simulations is found at 276 K and 136 K. In contrast, the simulated thermal expansion $\varepsilon^{av}_{\mathrm{Dy}}(t)$ averaged over the film thickness (dashed lines in figure 4.16.b) considerably deviates from the measured strain $\varepsilon_{\mathrm{Dy}}$, because the spin and phonon system are not even locally in thermal equilibrium. Closer to the phase transition the deviations get stronger and

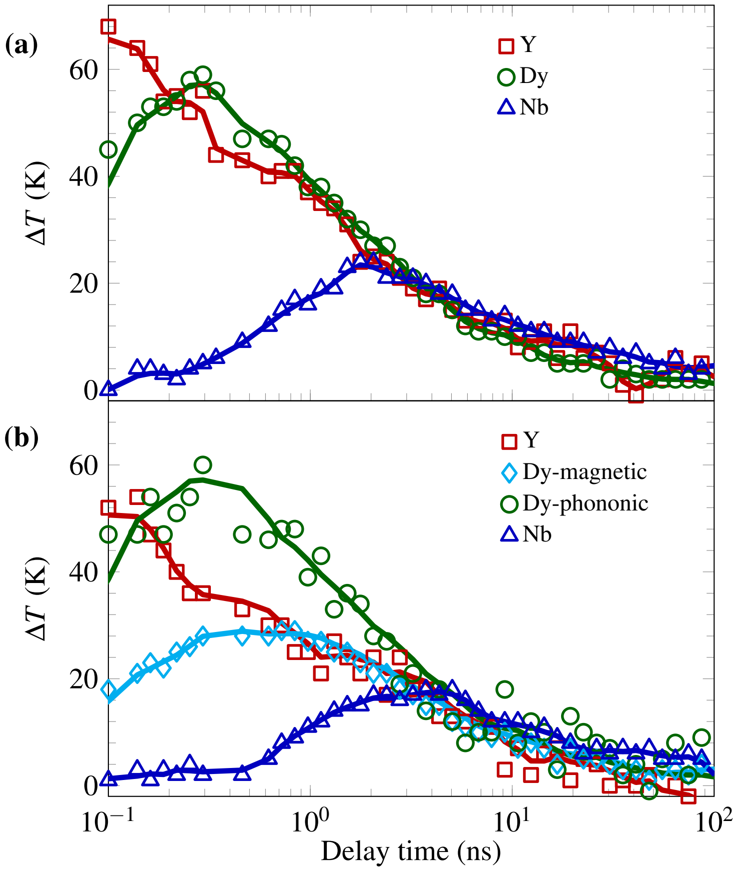

Figure 4.18.: Temperature change in each layer after excitation at (a) 276 K and (b) 136 K. The temperature in the magnetic system is only well defined at $T < T_\mathrm{N}$. Solid lines are running averages as a guide to the eye.

last longer.

Heat transport is driven by temperature gradients. Therefore, the transient temperature changes of the magnetic and phononic systems $\Delta T_{m,ph}$ in Dy and $\Delta T_{\mathrm{Y,Nb}}$ in Y and Nb are plotted in figure 4.18 as the experimental solution of the heat transport problem through the three layers as a function of time for two temperatures above and below T_N. The temperature rise ΔT is calculated from equation 2.14 for each subsystem. The most striking result is that, within the time resolution, the Y layer is heated by $T = 50$ K at low and $T = 68$ K at high temperature, although ellipsometry proves that the same amount of energy was deposited by the light pulse. This suggests that the additional energy dissipation channel into spin excitations at low temperatures dramatically speeds up the heat transport across the Y/Dy interface.

Another robust feature seen in figure 4.18 is the delayed temperature rise in the Nb layer, indicating a reduced heat transport through Dy. The temperature rise in the phonon system of Dy at both start temperatures is nearly the same, and therefore the heat arriving in the magnetic system effectively is additional to the phonon heat, explaining the observation in figure 4.17.a that the increase of the energy density in Dy is higher at low temperature. Note that the kinetics of the temperature rise in the spin and phonon systems of Dy are clearly different. The fact that the energy density in the magnetic system of Dy drives a lattice contraction counteracting the expansion initiated by phonon heating explains the strong deviations of the observed lattice strain $\varepsilon_{\mathrm{Dy}}^{av}(t) \neq \varepsilon_{\mathrm{Dy}}$ from the simulated strain (figure 4.16.b) when magnetic and phononic systems are not in a thermal equilibrium.

4.3. Results: gadolinium[2]

In this section, the static and time-resolved results of the UXRD experiments on the Gd sample III (see figure 4.3) are presented in the temperature range of the FM state of Gd.

4.3.1. Static characterization

The equilibrium out-of-plane lattice constants of Gd were measured in the temperature range between 90 K and 335 K. Figure 4.19.a shows the measured lattice constants of Gd as obtained from the 0002 reflection. The temperature-dependence of the lattice constant exhibit anomalies as seen in Dy. Decreasing the temperature from T_{C} the lattice constant expands due to the strong interaction of the lattice and the magnetic system by magneto-elastic coupling. The linear thermal expansion coefficient of Gd is presented in figure 4.19.b that is calculated from the temperature-dependence of the lattice constant using equation 4.4. The strong negative thermal expansion coefficient of Gd is closely related to the specific heat contribution of the ferromagnetic order shown in figure 2.10, as both clearly peak around 293 K. Using equation 4.6 the macroscopic Grueneisen coefficients Γ_m and Γ_{ph} are evaluated and shown in figure 4.19.c. The magnetic and phononic contributions follow from the appropriate decomposition of the thermal expansion coefficient $\alpha_{\mathrm{Gd}} = \alpha_m + \alpha_{ph}$ and the specific heat $C_{\mathrm{Gd}} = C_m + C_{ph}$. Here, the difference between thermal expansions driven by electrons and phonons is neglected, since it is only relevant on the few picosecond timescale, when the electron system is significantly hotter than the lattice [81, 82]. The thermal expansion above 350 K is approximated by the phonon driven expansion in the Debye model and extrapolated to low temperatures. In the relevant temperature range α_{ph} is essentially constant [59, 138]. The effective elastic constant K_{Gd} is calculated using the elastic constants from reference [139] and depends only weakly on the temperature.

4.3.2. Structural dynamics in the ferromagnetic phase

The time-resolved results of Gd are presented in this section. The penetration depth of the pump light is about 23 nm and effectively excites the Gd layer together with 10 nm Y layer on the top. For these measurements the initial temperature T of the sample was tuned across T_{C} between 212 K and 322 K, while the excitation was kept constant at an incident fluence of $F_i = 1.7\,\mathrm{mJ/cm^2}$. The given start temperatures are including a temperature increase of 12 K that results from the heat deposited at the high repetition rate. Figure 4.20 depicts the transient lattice strain in the Gd layer $\varepsilon_{\mathrm{Gd}}(t)$ after ultrafast laser heating. The lattice response at $T = 322\,\mathrm{K} > T_{\mathrm{C}}$ shows an initial expansion of the lattice as expected from phonon

---

[2] This section essentially follows my publication [123], therefore a large fraction of the section is identical to the publication.

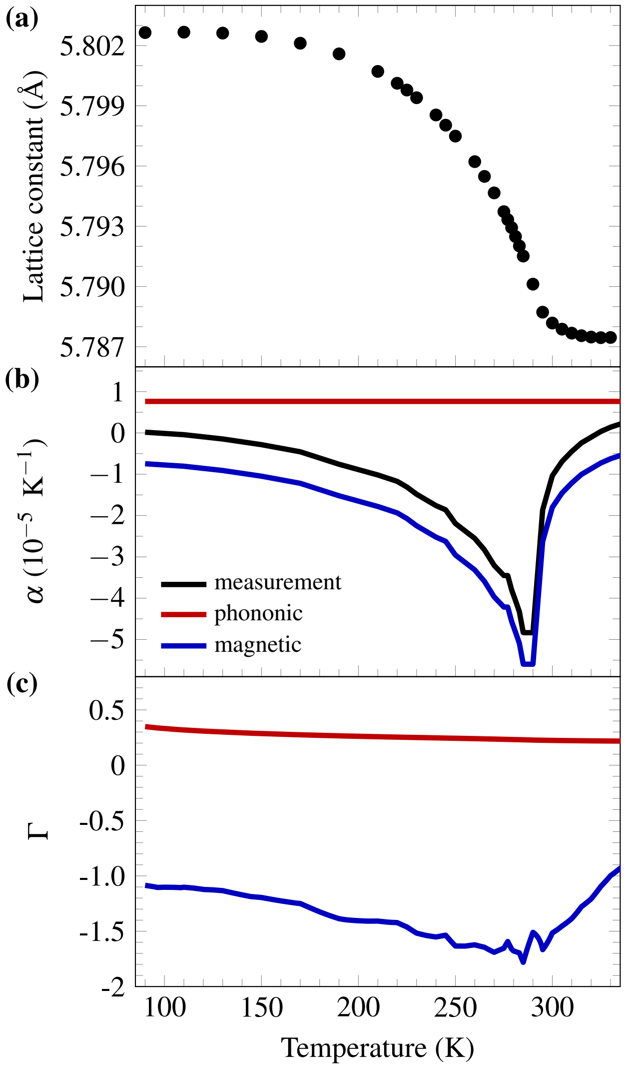

Figure 4.19.: Temperature-dependent parameters of Gd in equilibrium: a) out-of-plane lattice constant deduced from the 0002 reflection, b) the linear thermal expansion coefficient α, c) the macroscopic Grueneisen constant, Γ.

heating. Maximum strain is reached within the time-resolution. The lattice expansion relaxes within about 500 ps via heat diffusion into the substrate. All transients recorded for a start temperature below T_C show a lattice contraction at all time delays. This reflects the intimate coupling between interatomic distances and exchange interaction. The strongest negative expansion of about $-9 \cdot 10^{-4}$ at $T = 267$ K even exceeds the positive expansion measured at $T = 322$ K. With T approaching T_C, the contraction amplitude decreases while the relaxation of the transient strain slows down, with considerable contraction persisting longer than 10 ns. Close to the Curie temperature at $T = 292$ K an initial expansion is observed that is followed by a contraction for delays > 150 ps.

Qualitatively, the experimental results directly prove that a substantial fraction of the initial deposited

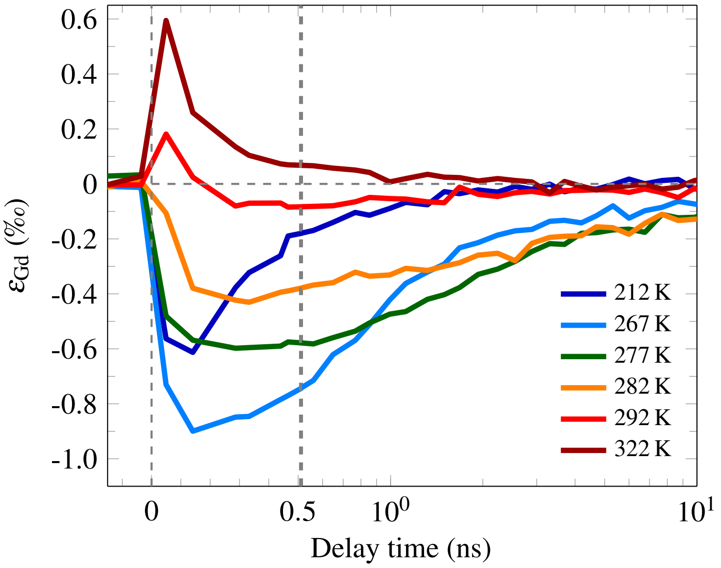

Figure 4.20.: Transient strain $\varepsilon_{\mathrm{Gd}}(t)$ in the Gd layer for different start temperatures T after ultrafast laser heating at $F_i = 1.7\,\mathrm{mJ/cm^2}$.

energy heats up the magnetic system because only $\Delta\rho_m^Q$ drives the negative expansion according to the Grueneisen coefficient. The contraction observed for $T = 292\,\mathrm{K}$ indicates that this is also true close to T_C, when the magnetic order is almost lost. Even when the thermal expansion coefficient turns positive above T_C, the phonon driven expansion is significantly reduced by magnetic contributions.

In the following, a strong non-equilibrium between the magnetic and phononic subsystems is shown and their different transient temperatures are estimated. It is important to note here that the electron and phonon systems have essentially equilibrated within the time resolution. Therefore one can describe both subsystems by a single temperature and only consider different heating of the magnetic and phononic systems. For the first analysis of the data an equilibrium model is assumed that both subsystems have the same temperature at all delay times. This enforces the static lattice constant $c(T)$ depicted in figure 4.19.a to map the transient temperature $\Delta T(t)$ via $c(t) = c(T)$. Likewise the transient strain would mimic the transient temperature via $\varepsilon(t) = \varepsilon(t)$. Three different examples are explained in the following that this equilibrium approach is incorrect:

i) Figure 4.21 illustrates two situations for different start temperatures T. In equilibrium, the maximum transient strain of $-4.3 \cdot 10^{-4}$ observed for $T = 282\,\mathrm{K}$ would correspond to a temperature rise of 9 K. In contrast, the maximum strain for $T = 212\,\mathrm{K}$ is $-6.1 \cdot 10^{-4}$, which would reflect a temperature rise of 42 K. These values can be directly obtained from the dashed and dash-dotted orange and blue lines in figure 4.21. The maximum temperature change extracted from the change in $\varepsilon(T)$ varies by about a factor of 5 for the two different starting temperatures, although the optical absorption coefficient is constant and consequently the same amount of energy is deposited. One can conclude from the observation at $T = 212\,\mathrm{K}$ that the deposited energy by the laser pulse must at least lead to a temperature rise of $\Delta T > 42\,\mathrm{K}$. At $T = 282\,\mathrm{K}$ the total heat capacity of Gd is at most 25% larger

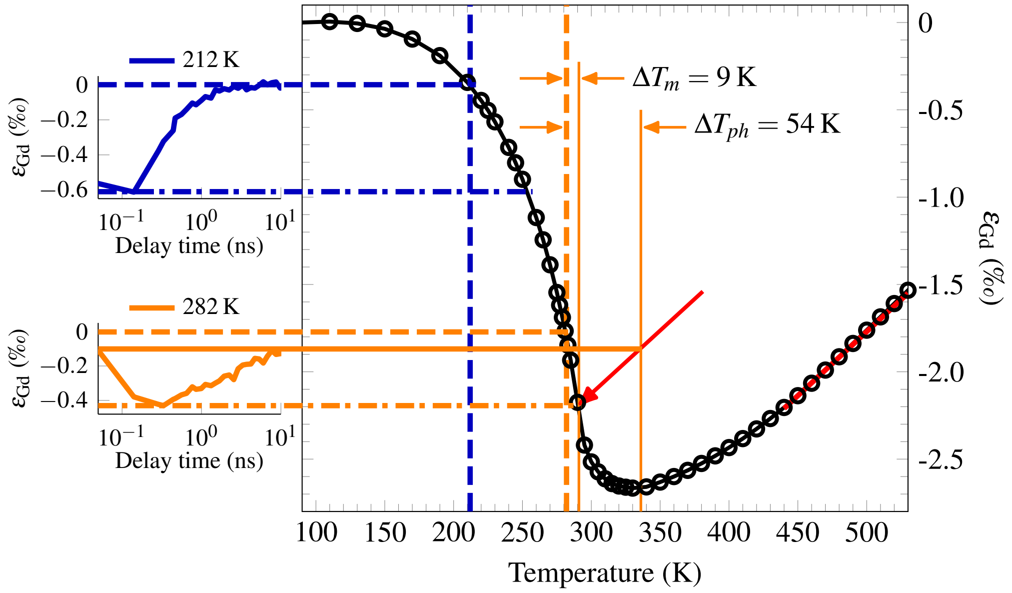

Figure 4.21.: Illustration of the temperature rise in the Gd layer after ultrafast laser excitation. The insets show the transient lattice response $\varepsilon_{\mathrm{Gd}}(t)$ for two selected start temperatures $T = 212$ K (blue) and $T = 282$ K (orange) reproduced from figure 4.20. The solid circles represent the measured lattice strain from static heating experiments (figure 4.19.a) extrapolated by using high temperature values from reference [59]. The thick dashed lines indicate the start temperature T and the corresponding $\varepsilon_{\mathrm{Gd}} = 0$. The dash-dotted lines show the maximum contraction, which yields a lower estimate of the temperature rise ΔT_m of the magnetic system. The solid lines highlight the initial non-equilibrium response that explains the tiny initial contraction at $t = 50$ ps resulting from a near cancellation of the contractive stress from heating magnetic system by $\Delta T_m = 9$ K and the expansive stress from heating the phonon system by $\Delta T_{ph} = 54$ K. The red line indicates the linear thermal expansion of Gd for high temperatures. The red arrow with the same slope symbolizes a fictitious exclusive cooling of the phonon system towards the equilibrium at $\Delta T_m = \Delta T_{ph} = 9$ K.

than at $T = 212$ K. Therefore, the temperature jump would at least be 24 K, contradicting the simple equilibrium description.

ii) Consider the situation at a $t = 50$ ps (solid orange line in figure 4.21), the failure to assume $T_m = T_{ph}$ becomes even more obvious. The lattice response shows a strain of $-1 \cdot 10^{-4}$ corresponding to a temperature rise of only 1 K. In fact this can only be explained in a non-equilibrium model by assuming a simultaneous heating of magnetic and phonon systems with an almost exact cancellation $\alpha_m \Delta T_m \approx \alpha_{ph} \Delta T_{ph}$ of the lattice contraction and expansion. If this relation is written in terms of the energy densities it follows $-\Gamma_m \Delta\rho_m^Q = \Gamma_{ph} \Delta\rho_{ph}^Q = \Gamma_{ph}\left(\Delta\rho_{\mathrm{Gd}}^Q - \Delta\rho_m^Q\right)$. From the latter identity one can immediately conclude that the magnetic system initially takes the fraction $\Delta\rho_m^Q / \Delta\rho_{\mathrm{Gd}}^Q = \Gamma_{ph}\left(\Gamma_{ph} - \Gamma_m\right) = 14\%$ of the total deposited energy $\Delta\rho_{\mathrm{Gd}}^Q$ Gd at $T = 282$ K. This analysis is robust, because strain and energy density are linearly related, and it implies a similarly large difference in ΔT_m and ΔT_{ph}, since the heat capacity C_m at 282 K is only 20% smaller than $C_{ph} + C_e$. Figure 4.22

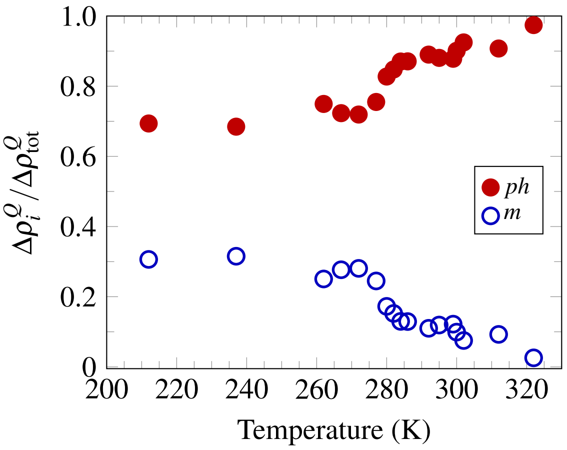

Figure 4.22.: Fraction of the initial energy density in the magnetic and the phonon system as a function of start temperature.

shows the distribution of energy density $\Delta\rho_m^Q$ and $\Delta\rho_{ph}^Q$ for different start temperatures, determined 50 ps after the excitation by the TTEM explained in the next section.

iii) The third important example is the estimation of the temperature rise required to rationalize the contraction of $-6.1 \cdot 10^{-4}$ for $T = 212\,\mathrm{K}$. In equilibrium the temperature rise is expected to be at least $\Delta T > 42\,\mathrm{K}$ to account for the contraction. In non-equilibrium, one can also explain the observation by a larger temperature rise ΔT_m of the magnetic system assuming that the phonon system receives even more energy. This situation is graphically explained in figure 4.21 for the example of $T = 282\,\mathrm{K}$. At $t = 50\,\mathrm{ps}$, the dynamics start at a small negative strain level indicated by the solid orange line. This is the strain level given by an approximate balance of expansive and contractive stresses. The dash-dotted orange line indicates the maximum negative strain at $t \approx 300\,\mathrm{ps}$. At this time the magnetic and the phonon systems must at least still be heated by 9 K. In order to explain the strain balance just after excitation, one has to assume an excessive heating of the phonon system beyond the temperature of the magnetic system. The red line in figure 4.21 indicates the slope at which the phonon heating leads to strain according to the high-temperature thermal expansion. Assuming an initial temperature jump of the magnetic system by $\Delta T_m = 9$ K the phonon system must exhibit an initial temperature jump of $\Delta T_{ph} = 54\,\mathrm{K}$ to compensate the negative strain of the magnetic system. This yields a lower estimate of the energies leading to the non-equilibrium. Starting from this fictitious non-equilibrium state, the red arrow would indicate the path of the system via exclusive phonon cooling towards a fictitious equilibrium at the maximum contraction for $\Delta T_{ph} = \Delta T_m = 9\,\mathrm{K}$. The real non-equilibrium state is determined by the TTEM presented in the next section, where the initial temperature jumps are obtained as $\Delta T_{ph} = 70\,\mathrm{K}$ and $\Delta T_m = 15\,\mathrm{K}$, respectively.

4.3.3. Grueneisen-approach for transient spin and phonon energies

In order to decompose the measured lattice strain and the initial energy density quantitatively into the magnetic and phononic contributions at temperatures below T_C, the TTEM model is used. The laser-induced change of the energy densities $\Delta\rho^Q_{ph,m}$ generates the stresses $\sigma_{ph,m}$ which superimpose to yield the proportional strain:

$$\varepsilon_\mathrm{Gd} = \frac{\sigma_{ph} + \sigma_m}{K_\mathrm{Gd}} = \frac{1}{K_\mathrm{Gd}} \left(\Gamma_{ph}\Delta\rho^Q_{ph} + \Gamma_m \Delta\rho^Q_m \right) \ . \tag{4.17}$$

The parameters $\Gamma_{ph,m}$ are K_Gd are known (see section 4.3.1) and ε_Gd is measured. Individual energy densities $\Delta\rho^Q_{ph,m}$ are determined using the relation $\Delta\rho^Q_\mathrm{Gd} = \Delta\rho^Q_{ph} + \Delta\rho^Q_m$. It was not possible to conduct the UXRD experiment on Gd at high temperatures for determination the total energy density. Therefore the $\Delta\rho^Q_\mathrm{Gd}(0\,\mathrm{ps})$ is calibrated with the total energy density in Dy sample I already shown in section 4.2.2.1 taking into account the absorbed fluence using the advantage of the similar sample structures on the top of sample I and III (see figure 4.3). Additionally, the dynamics $\Delta\rho^Q_\mathrm{Gd}(t)$ is also an estimate for the phonon cooling at lower T, since for $T = 322\,\mathrm{K}$ the energy is essentially fed into the phonon system. Figure 4.23 depicts the results of the decomposition by the TTEM. Figure 4.23.a shows the energy densities in the magnetic and phonon systems. For $T = 267\,\mathrm{K}$ as much as 30% of the deposited energy enters the magnetic system. The phonon system cools faster than the spins, and already after 200 ps less than 50% of the energy resides in the phonons. For $T = 322\,\mathrm{K}$ the contribution of the magnetic system starts with less than 10%. The transport of heat and the interconversion of energy between subsystems should be governed by the temperature, which is plotted in figure 4.23.b. The increase of the temperature of the magnetic system is reduced at temperatures just below T_C. This in part explains why the cooling of the spins for $T = 267\,\mathrm{K}$ and $T = 282\,\mathrm{K}$ is slowed down. For higher start temperature, the fraction of energy initially deposited in the magnetic system is reduced (see figure 4.22), and the specific heat increases near the phase transition. Both facts reduce the change of the magnetic temperature ΔT_m and hence it takes a longer time until the phonon temperature T_{ph} has cooled below T_C. The main reason for the reduced energy deposition in the magnetic system is the decreasing spin contribution of the specific heat above T_C. Although this contribution diverges at T_C, the integral over a finite ΔT is finite and decreases when the effective end-temperature is above T_C. The phonon contribution is approximately constant in the relevant temperature range, and hence the fraction of energy exciting the phonon system increases. In the limit of very high temperatures, the $\Delta\rho^Q_m$ must converge to zero, and 100% of the energy remain in the phonon system.

In the results for all start temperatures $T < T_\mathrm{C}$, the phonon system is initially heated more than the spin system. Not only is the contribution to the energy density higher $\Delta\rho^Q_{ph} > \Delta\rho^Q_m$ but also the temperature rise $\Delta T_{ph} > \Delta T_m$. The phonon system cools faster than the spin system, after the time t_{eq}, they reach equal temperatures. However, the phonon system keeps cooling faster and therefore the temperature rise is inverted ($\Delta T_{ph} < \Delta T_m$). This inversion of the temperatures observed for all transients below T_c shows that the magnetic system is decoupled from the electron-phonon system on the $100\,\mathrm{ps} - 1\,\mathrm{ns}$ timescale,

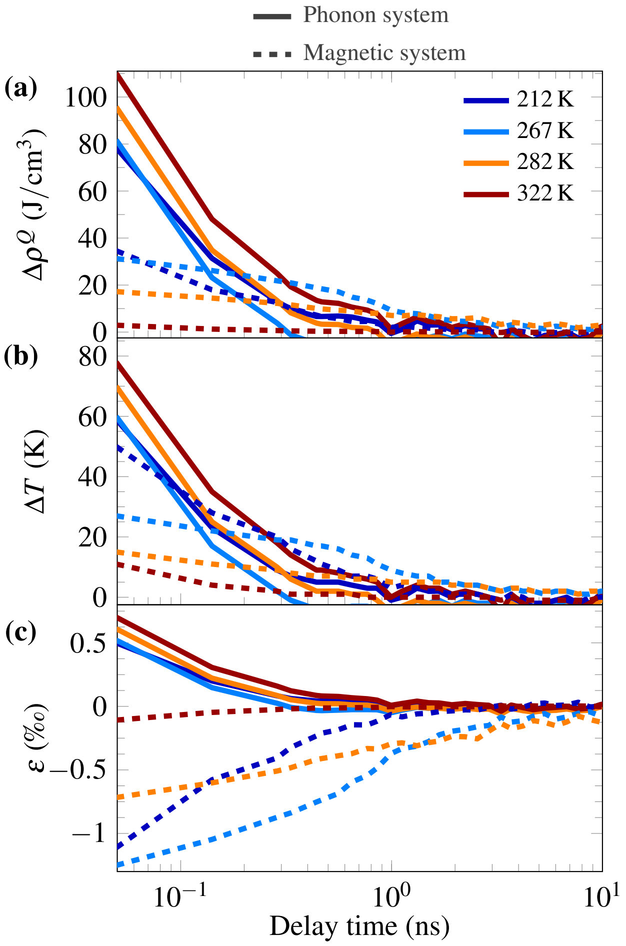

Figure 4.23.: Result of the data analysis by the TTEM for selected start temperatures. Solid and dashed lines represent the results for phonon and spin systems, respectively. a) Transient energy density, b) temperature change and c) transient strain.

although the initial transfer of energy from electrons to phonons and spins is very rapid. Note that t_{eq} is smaller for low temperatures and the inversion is more pronounced towards the phase transition. The results measured at the lowest temperature of $T = 212$ K, the phonon temperature increase decays to half of its value within 120 ps and the temperature rise of the magnetic system requires about 200 ps to decay to its half value. Taking into account the larger thermal conductivity at 100 K, the results are consistent with relaxation times of about 80 ps reported in references [14, 16, 140].

5. Resonant soft x-ray diffraction experiments

In this second experimental part of this work, the magnetic order and in particular recovery dynamics of the magnetic order in Dy in the ps up to the µs range after ultrashort photoexcitation is investigated by time-resolved RSXD, where we have used femtosecond optical pump and soft x-ray probe pulses. RSXD experiments provide a direct measurement of long-range periodic antiferromagnetic order in solids due to the transition between the core energy levels by tuning the photon energy to the corresponding element-specific resonance energy [116]. In the experiments discussed in this chapter, the magnetic structure of Dy is directly probed as the soft x-ray energy is tuned to the M_V absorption edge of Dy that is characterized by a strong $3d \rightarrow 4f$ transition at about 1293 eV, because the localized $4f$-electrons are mainly responsible for the long-range helical antiferromagnetic order, HAF, in Dy. The wavelength at the M_V edge of about 9.59 Å has the right magnitude to diffract from the magnetic modulation periodicity of about 21-28 Å depending on the investigated samples and temperature in Dy. These experiments will also allow us to compare the recovery dynamics of HAF order in Dy with the dynamical structural response, which has been presented and analyzed in the context of TTEM in section 4.2.2.1. This comparison allows us to crosscheck the applicability of dynamical structural diffraction measurements for the analysis of magnetization dynamics for materials with strong magneto-elastic coupling and hence large magnetostrictive properties.

This chapter includes three parts. At first, the technical details and the data acquisition are explained. In the last part, the results of static sample characterization and dynamics of the antiferromagnetic order as a function of the excitation fluence and the sample temperature are presented. These cover the slow dynamics observed in the ps up to µs range.

5.1. Experimental setup

The experiments have been performed at the FemtoSpex slicing facility at the storage ring BESSY II (UE56-1_ZPM). The beamline offers many different experimental techniques which include XMCD, resonant and non-resonant x-ray diffraction, and x-ray absorption spectroscopy in the soft x-ray regime [141]. By means of these methods, magnetization dynamics after optical excitation of the sample is investigated in the time range from fs up to µs. The beamline can be operated in the FEMTO-slicing mode, where femtosecond x-ray pulses are produced in the undulator [142, 143]. However, the data presented in this thesis have been obtained in the ps-mode and only the experimental prerequisites for this mode will be covered in the following.

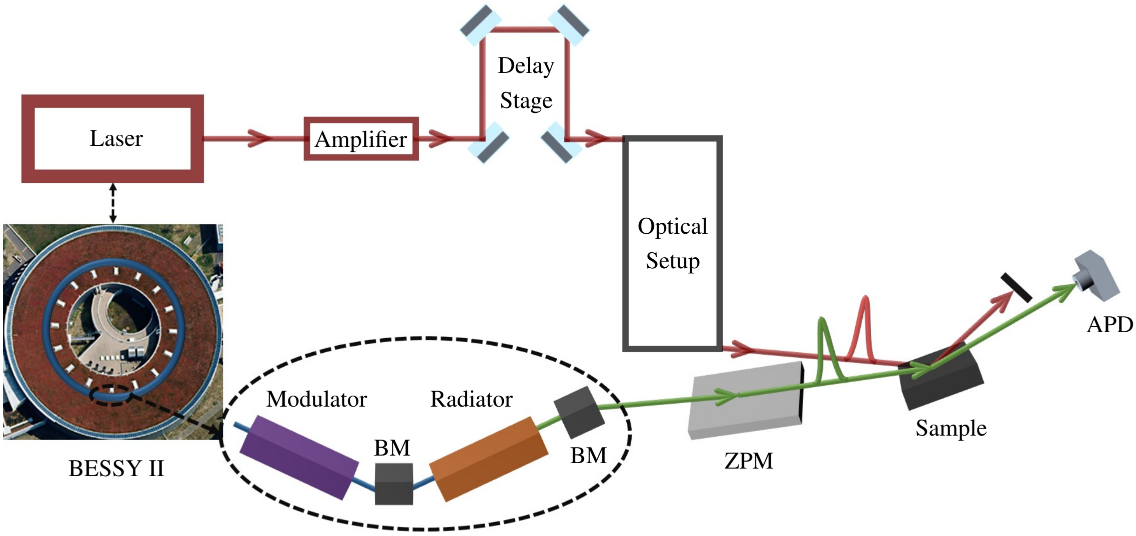

Figure 5.1.: Schematic of the RSXD experimental setup at the Femtospex beamline at BESSY II [143]. BM: bending magnet, ZPM: zone plate monochromator, APD: avalanche photodiode. Modulator, bending magnets and radiator are installed in the storage ring.

A schematic layout of the beamline and experimental setup of time-resolved RSXD experiments in ps-mode is shown in figure 5.1. Electron bunches in the storage ring are directed via a bending magnet into undulator U139, the so-called modulator, which is relevant particularly for the slicing operation. The radiator UE56/1, an undulator with 30 periods with 56 mm length, is positioned after the modulator in order to produce x-ray pulses with desired polarization and energy range. In our case, linearly π-polarized x-ray pulses with photon energies between 250 to 1400 eV are emitted from the undulator. The electron storage ring was operated in the single bunch mode, therefore x-ray pulses are generated with ~ 80 ps pulse duration at 1.25 MHz repetition rate. After the undulator, x-ray pulses are guided to a high-flux zone plate monochromator (ZPM) that is used for energy selection and horizontal and vertical focusing of the beam onto the sample. The reflected or diffracted x-ray photons from the sample are detected with a fast avalanche photodiode (APD) operated in single photon counting mode at the bias reverse voltage of about 290 V. Due to the ZPM and a quartz vertical slit with about 100 µm aperture in front of the detector, an energy resolution of $\Delta E/E = 10^{-2}$ is achieved. The sample is mounted on the cold finger of a cryostat in an ultrahigh vacuum chamber, which allows cooling of the sample down to 77 K or 6 K using liquid nitrogen or helium.

Photo excitation of the samples is performed with 50 fs laser pulses with a central wavelength of 800 nm ($E_{\text{photon}} = 1.5$ eV) , which are generated from a Ti:Sa oscillator. A regenerative amplifier produces laser pulses with 3 kHz repetition rate and 2 mJ pulse energy. The optical setup before the diffraction chamber direct the laser beam into the diffraction chamber and focus it onto the sample. In addition, they include optical components for controlling the polarization state and power of the laser beam.

The laser excites the sample with an angular offset of 1.5° with respect to the incoming x-ray beam.

The laser illuminates an area with FWHM of 300 × 270 µm that enables homogeneous pumping of the area that is probed by the x-ray beam, which has a FWHM of 140 × 100 µm at normal incidence. Because pump and probe beams are almost collinear, the detector is protected by a 250 µm thick aluminum window, which is transparent for x-rays, but blocks the reflected laser light from the sample.

5.2. Data acquisition

The RSXD experiments are performed in a specular reflection geometry as explained in section 4.1.2 and displayed in figure 4.4.a. The optical pump and x-ray probe pulses are focused almost collinearly onto the sample. The sample is set to the Bragg angle θ and the detector is positioned at 2θ. The x-ray photon energy is set to the $\mathrm{M_V}$ absorption edge energy of Dy. During a θ - 2θ scan in the angular range between 4° and 17°, the diffracted signal intensity is monitored. It includes the signal from the scattering of x-rays from the charges in the sample and diffraction of the x-rays from the helical arrangement of the local magnetic moments of Dy at the reciprocal space position (000+τ) with τ being the modulation vector that denotes the inverse period of the HAF order. In this thesis, this signal is mostly presented as a function of the scattering vector, q, denoting the momentum transfer along the c-axis that is calculated by

$$q = \frac{4\pi}{\lambda} \sin\theta \quad . \tag{5.1}$$

In figure 5.2.b, a typical θ - 2θ scan at 130 K is shown. The origin of the decreasing intensity as q increases is the reflectivity originating from the scattering of x-rays from the charge density. In this regime, the intensity is proportional to q^{-4}. The first-order magnetic Bragg reflection of Dy occurs at around $\theta = 9.5°$ at 130 K. The scattering vector at the maximum of the magnetic peak corresponds to the modulation vector at the given temperature. From the FWHM of the magnetic peak,w, the magnetic correlation length can be extracted. However, it will be shown in section 5.3.1 that the limited penetration depth of the soft x-rays at small angles determines the observed value of peak width. The integrated intensity I is proportional to the square of the order paramater $I \propto O^2$ [144], that is the sublattice magnetization for the HAF order. In order to extract the inverse helix period from the raw experimental data, the peak width and the integrated intensity of the magnetic peak, a fit function is used that is the sum of the charge reflectivity background and an asymmetric pseudo-Voigt profile with two different peak widths on the right and left hand side of the peak center, w_R and w_L, respectively. The fit result is shown as black line in figure 5.2. In order to extract the magnetic peak independent of charge reflectivity, the fit result of the charge reflectivity is subtracted from the measured signal prior to the numerical integration. The extracted magnetic peak from the raw data is displayed in the inset of figure 5.2.

The first set of measurements has been performed without photoexcitation and yields the static characterization of the magnetic scattering properties of each sample. The second part deals with time-resolved measurements, that is optical pump-soft x-ray probe experiments. In the latter case, the sample is excited with 50 fs laser pulses and the magnetic response of Dy is investigated with soft x-ray pulses.

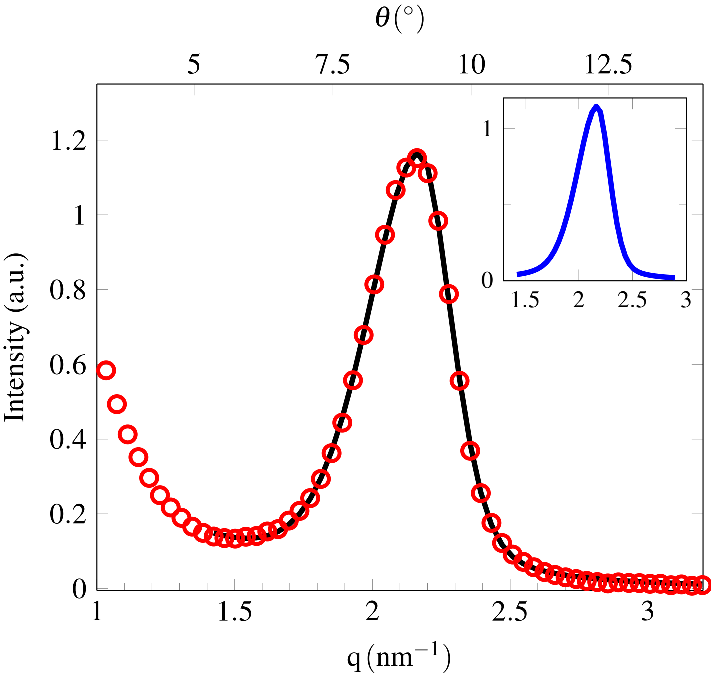

Figure 5.2.: A typical signal with θ - 2θ scan in the angular regime from 4° to 17° (red circles) from sample I (see figure 4.3). The decreasing intensity at small angles is the charge reflectivity and the first-order Dy magnetic peak occurs at about 9.5° at 130 K. Black solid line is the fit result of the data with the function of sum of charge reflectivity and an asymmetric pseudo-Voigt profile. The inset presents extracted magnetic Bragg peak of Dy layer via subtracting the fit result of charge reflectivity from the measurement.

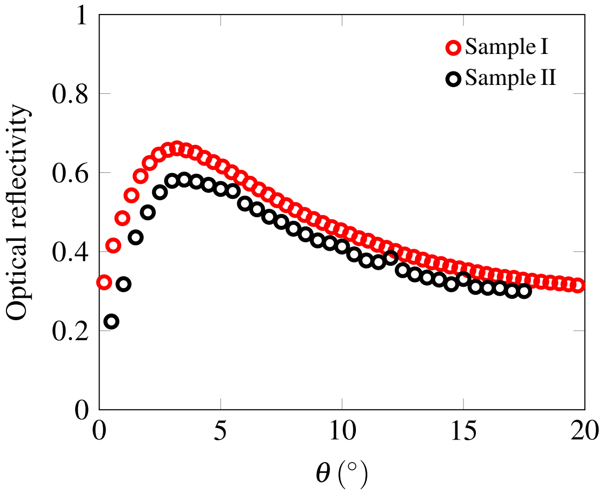

Figure 5.3.: The angle-dependent optical reflectivity of the sample surface from sample I and sample II for pump beam with the central wavelength of 800 nm. For the definition of sample I and II, see figure 4.3.

Therefore a delay between the pump and probe pulses is introduced.

Before we started the time-resolved investigations, the following adjustments were performed:

i) The power P of the laser is calibrated with the motorized waveplate and powermeter before the vacuum chamber in order to determine and, if necessary adjust the power.

ii) The angle-dependent optical reflectivity, R, of the sample surface for the pump beam is measured. The result for both samples is shown in figure 5.3. Now, the absorbed fluence F_a can be calculated using

$$F_a = \frac{P}{A \cdot f_\mathrm{rep}} \sin\theta(1-R) \ . \tag{5.2}$$

Here f_rep denotes the pulse repetition rate and A is the pumped area at normal incidence. This correction is necessary because the sample reflectivity changes quite drastically at grazing incidence. In order to excite the samples at each Bragg angle with the same fluence, the laser power is automatically adjusted to compensate for the variation of the reflectivity.

iii) Spatial and temporal overlap between the pump and probe pulses is determined similarly to the XPP measurements discussed in section 4.1.2.

We have performed two types of time-resolved experiments with different time resolution and different maximum measured delay, which we call synchronous and asynchronous measurements. Both modes are explained in following in detail:

a) Synchronous measurements: The pump laser is synchronized directly to the ring bunch clock (1.25 MHz) and a delay stage is used to introduce the temporal delay between optical pump pulse and x-ray probe pulse. The delay is limited to 4 ns and the x-ray pulses are approximately 80 ps, which determines the time resolution. Two pump laser pulses are seperated by the time period of about 333 µs and in this time interval many x-ray pulses with 800 ns repetition period probe the sample. As the laser is synchronized to the bunch clock, this allows a measurement of the sample response with and without laser excitation at every measured delay, i.e. the pumped and unpumped signal [141]. The unpumped signal is used for the normalization of experimental data. The diffraction signal is measured performing θ - 2θ scans at different delays. All extracted parameters p via synchronous measurements are presented in form of relative changes, RC, in section 5.3.2, that is calculated by

$$RC = \frac{p_{pu} - p_u}{p_u} \ , \tag{5.3}$$

where the subscripts pu and u denote the parameter of the pumped and unpumped signal, respectively.

In figure 5.4.a the diffraction intensity of pumped magnetic Bragg peaks of the Dy helix in sample I at two delay are presented. These have been measured in the synchronous measurements at 150 K and an absorbed fluence of 1 mJ/cm^2. In the inset, the corresponding unpumped data are shown. The temporal variation of the integrated intensity as function of delay time for both pumped and unpumped signal is shown in figure 5.4.b.

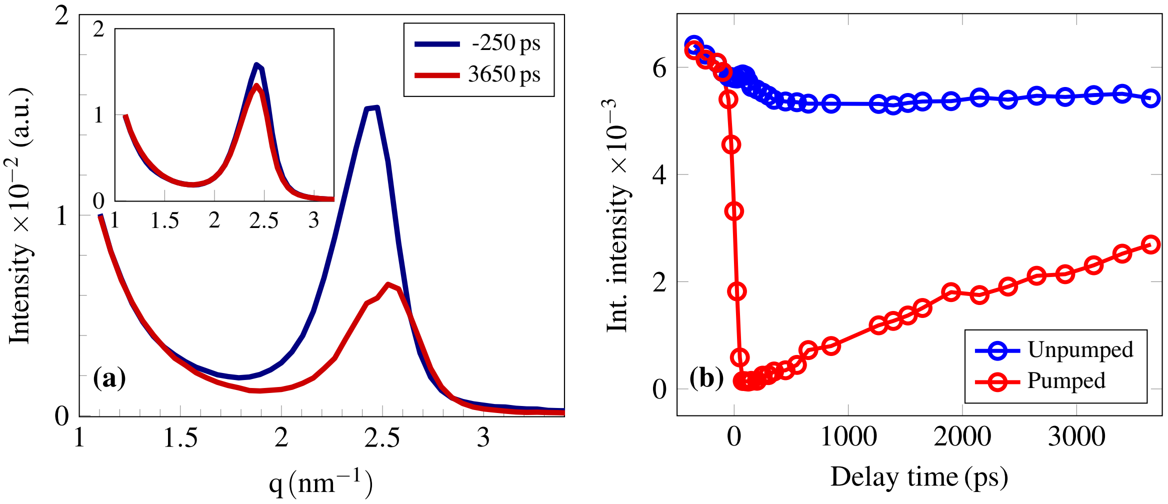

Figure 5.4.: a) Data acquisition in synchronous mode: the measured intensity of sample I as function of q is shown for two delays between pump and probe pulses. The data have been acquired at 150 K and an absorbed excitation fluence of 1 mJ/cm^2. The inset displays the signal without photo excitation (unpumped). b) Integrated intensity of pumped and unpumped magnetic peaks as function of delay time.

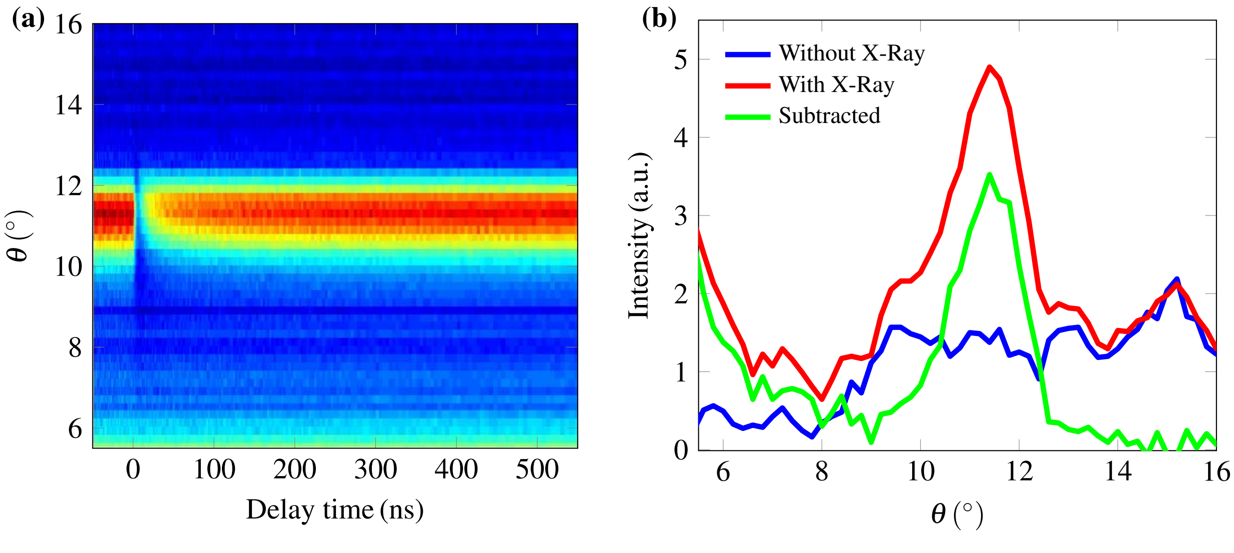

Figure 5.5.: Data acquisition in asynchronous mode: measurements at 160 K and 1 mJ/cm^2 absorbed fluence of sample I. a) Contour plot of each data sequence that is recorded at one $\theta - 2\theta$ as a delay trace up to 500 ns. The electronic background has been subtracted from the data. b) Electronic background, the measured signal and the diffraction signal after subtracting the electronic background. The traces are taken from time delay 51 ns.

b) Asynchronous measurements: In this mode, the pump and probe pulses are not synchronized. The oscilloscope is triggered with the laser repetition rate and records the signal of the APD. The laser pulse is static on the oscilloscope and a complete delay trace with all x-ray pulses arriving between two laser pulses is monitored at one angle. The same is repeated for several Bragg angles between 4 ° and 17 °. This type of measurement allows us to measure long delays up to µs after photo excitation. However, the time resolution is limited to ~ 4 ns by the electronics. For reduction of further time resolution limitation, only delays up to 20 µs of 333 µs measurable regime are displayed on the oscilloscope. In order to reduce the electronic noise, the same measurement is performed at each angle without x-ray beam and it is subsequently subtracted from the measured sample signal. An asynchronous measurement at 160 K and 1 $\mathrm{mJ/cm^2}$ absorbed fluence is shown in figure 5.5.a as a contour plot for the delay time up to 500 ns. The electronic background for this data set has been subtracted. The data is a line parallel to the time axis and measured in one oscilloscope trace for each θ angle. By means of this contour plot, the magnetic Bragg peak at each delay time is reconstructed. Figure 5.5.b shows the electronic background, the detected signal and the difference of the two at delay 51 ns. In this measurement, the spatial overlap remains the same and the time zero is given by the fixed position of the laser pulse on the oscilloscope. All extracted parameters p via asynchronous measurements are also presented in form of relative changes in section 5.3.3, that is calculated by

$$RC = \frac{p(t>0) - p(t<0)}{p(t<0)} \quad . \tag{5.4}$$

5.3. Experimental results

5.3.1. Static characterization

The temperature-dependence of the first order Dy helical antiferromagnetic Bragg peak is determined for sample I and sample II. The sample has been cooled down and heated up without applied magnetic field. For the static measurements, the sample temperature is varied from 130 K up to 185 K and for each temperature a θ - 2θ scan is performed. The measured intensity of the magnetic peak as function of the scattering vector q is presented in figure 5.6 for both samples. At small q vectors the signal is dominated by x-ray reflectivity, which does not exhibit Kiessig fringes because the penetration depth of the soft x-rays at their absorption edge is less than the film thickness. The scattering of the soft x-rays from long-range sinusoidally arranged magnetic moments occurs for sample I at q vectors $>$ 2.1 nm^{-1} and is characterized by a decreasing intensity and shift of the observed maxima towards higher q values as the temperature is increased. Sample II shows a very similar feature, however, the q vector is shifting to higher values, the overall intensity and the peak width are reduced. In the following, the static characterization measurements are analyzed using the fit function as introduced in section 5.2. This analysis yields the modulation vector and the normalized integrated intensity that provides the order parameter, which are presented in figure 5.7 as function of temperature. The modulation vector, that is the maximum of the magnetic scattering signal, occurs around 2.17 nm^{-1} at 130 K for sample I. This

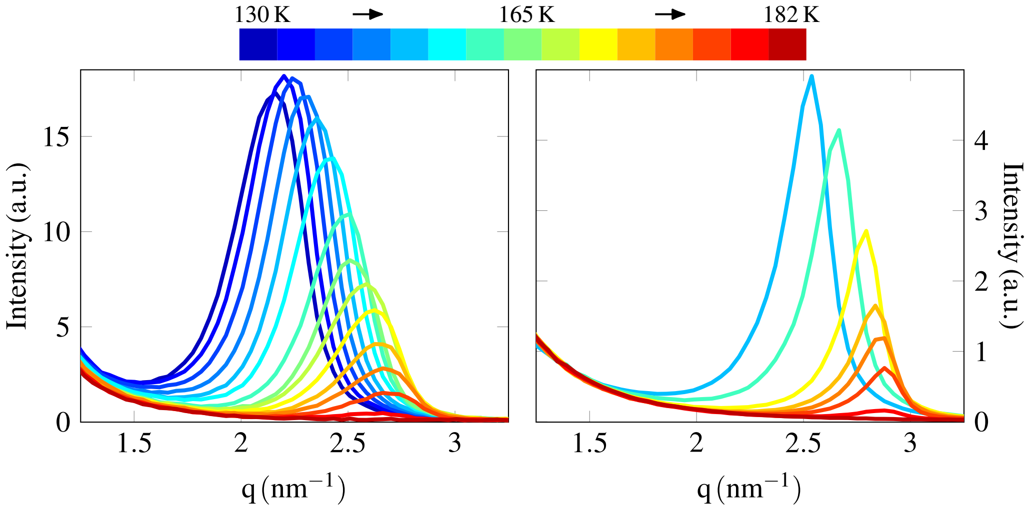

Figure 5.6.: Temperature-dependent x-ray scattering measurements as function of scattering vector, q, at the Dy M_V absorption edge of around 1293 eV for sample I in the left panel and sample II in the right panel in temperature range between 130 K and 180 K.

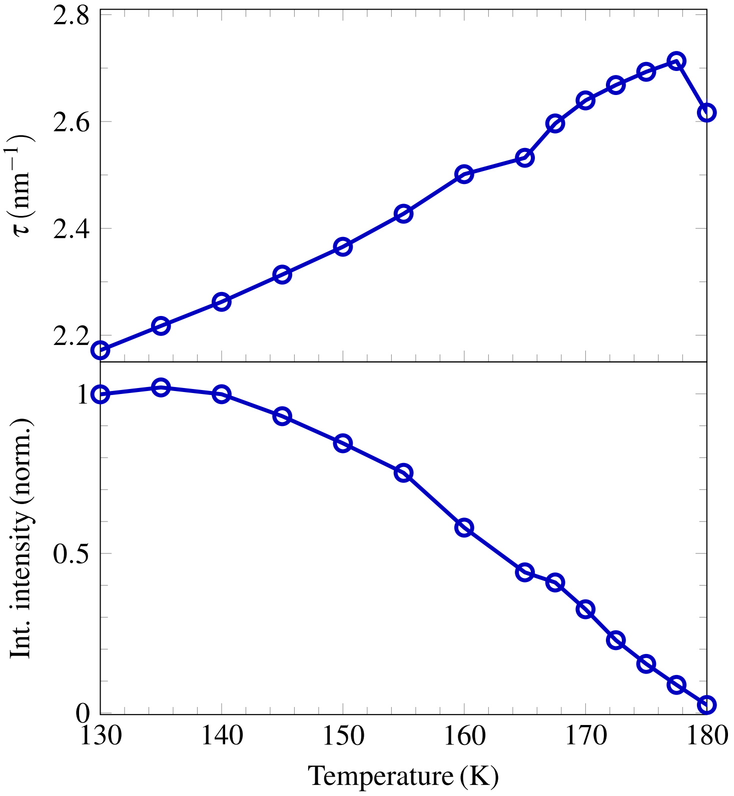

Figure 5.7.: a) Modulation vector, τ and b) normalized integrated intensity of first order Dy magnetic peak (000+τ) as function of temperature of sample I.

gives a period of $2\pi/\tau \approx 2.89\,\mathrm{nm}$, which corresponds to approximately 10.4 atomic distances of the Dy layers that does not match an integer of lattice constant, c. The spin helix is incommensurate with the lattice [40, 145]. The magnitude of the modulation vector increases monotonically as the temperature is increased up to 178 K, which implies a linear decrease of the period of the spin helix in real space. Sample II shows a very similar temperature-dependence of the modulation vector, however it occurs at higher τ values, which results in a shorter period of spin helix in sample II. It seems that around AFM-PM phase transition the modulation vector decreases slightly.

The integrated intensity decreases above 140 K due to the increase of magnetic fluctuations. Using the temperature dependence of the integrated intensity I, one can infer the static critical exponent β, of Dy, which describes the critical decrease of the order paramater for 2nd order AFM to PM phase transition (section 2.4) by fitting the data points with the power function, $I = A\,\epsilon^{2\beta}$ with the reduced temperature $\epsilon = |(T - T_\mathrm{N})/T_\mathrm{N}|$. The factor 2 is used due to the fact that the sublattice magnetization is the square of the integrated intensity. In figure 5.8, the data and fit results are presented as function of the reduced temperature in logarithmic scale with the fit parameters of $A = 3.457$ and $\beta = 0.418, 0.393$ for sample I and II, respectively. The β values are consistent with the other experiments reported in reference [100].

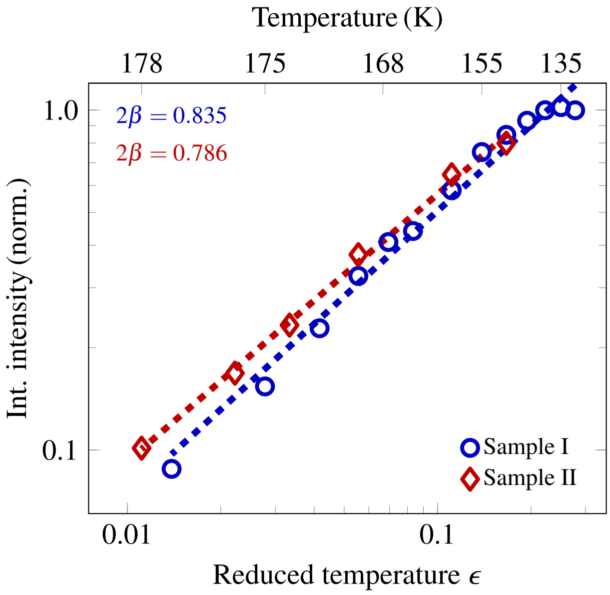

Figure 5.8.: The critical behavior of the integrated intensity of magnetic Bragg peak I, as function of reduced temperature, $\epsilon = |(T - T_\mathrm{N})/T_\mathrm{N}|$, for sample I and II. The symbols are the data points and the dashed lines are the fit of $I = A\,\epsilon^{2\beta}$ with the parameters, $A = 3.457$, $2\beta = 0.835$ and $2\beta = 0.786$, where β denotes the static critical exponent of Dy.

It is now possible to calculate the turn angle ϕ between magnetic moments of the neighboring $4f$ electrons. Therefore one needs two experimental results, lattice constant c as measured by XRD and the modulation vector τ obtained from RSXD. The angle is given by $\phi = 180^\circ\,\tau c/2\pi$ and the value as function of temperature is presented in figure 5.9 for both samples and for comparison the bulk value determined by Wilkinson [42] is also shown. The bulk values are inferred from neutron diffraction experiments. In the temperature regime of interest, the interlayer turn angle in sample I varies between 35° and 43.2°, which is very close the one in bulk Dy. However, a slight deviation occurs at lower temperatures. For sample II, the interlayer turn angle is much higher than in sample I and bulk Dy. Epitaxial strain in Dy films has a large impact on the structural and magnetic properties, and hence on the interlayer turn angle [129, 146]. One would expect that this is mostly determined by the growth conditions of the layer, however, our data imply that even the thickness of the surrounding metallic layers results in a significant stabilization of the HAF order in Y/Dy/Y heterostructures [146].

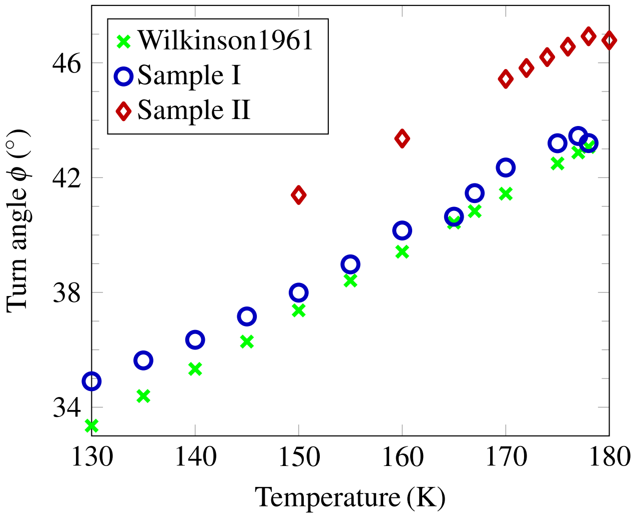

Figure 5.9.: Temperature variation of the interlayer turn angle ϕ in sample I, sample II that are as calculated from the XPP and RSXD data for lattice constant c and the modulation vector τ and in bulk Dy that is reproduced from [42].

Another piece of information can be obtained from the width of the magnetic Bragg peak of Dy. In figure 5.10.a the arithmetic mean of the asymmetric peak widths at FWHM of the right hand side and the left hand side, w_R and w_L, is presented. For the detailed temperature-dependence of w_R and w_L, see figure B.1 in the appendix. Even though the peak width is directly related to the correlation length in Dy, no significant width change is observed as the sample temperature is varied. This is caused by the limited penetration depth of the soft x-ray beam, ξ_{XR}, at resonance that is given for the Bragg angle θ and the wavelength of x-rays λ by

$$\xi_{XR}(\theta) = \sin\theta \, \frac{\lambda}{4\pi\beta} \, , \tag{5.5}$$

with the imaginary part, β, of the refractive index, $n = 1 - \delta + i\beta$, in the x-ray region. If the correlation length is larger than ξ_{XR}, the peak width is proportional to $1/\xi_{XR}$. The penetration depth strongly depends on the Bragg angle, therefore we compare the magnetic peak of both samples at the same sample

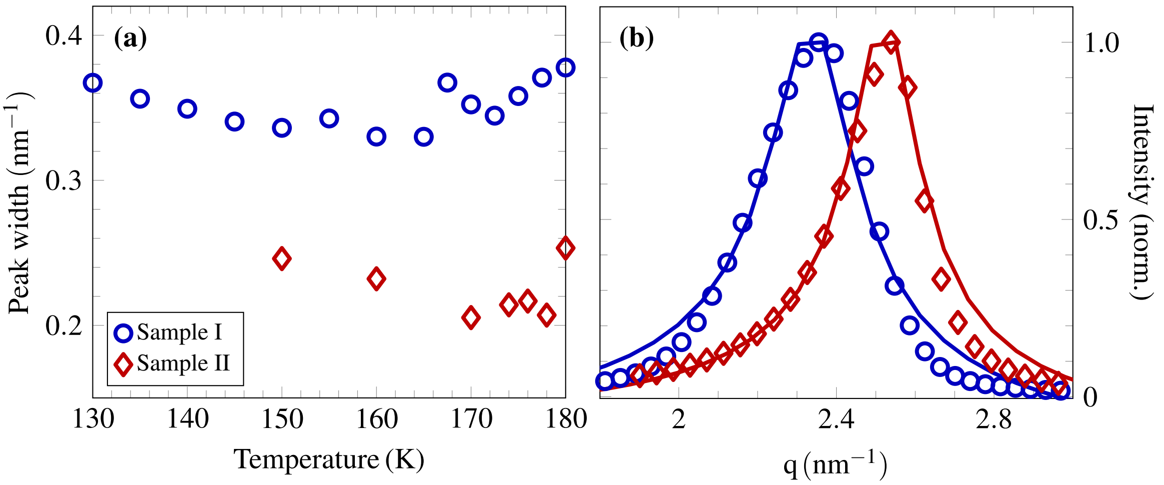

Figure 5.10.: a) Arithmetic mean of left and right widths of Dy magnetic peak as function of temperature. The results are shown for sample I and II. b) The magnetic peak (symbols) of Dy layer for sample I and sample II at 150 K compared to the Fourier transformation of a sinusoidal wave with exponential decay (solid lines). The decaying is caused by the absorption of the x-rays in the Dy layer. Here is a good agreement is obtained for penetration depth of 10 nm (sample I) and 12.5 nm (sample II).

temperature in order to calculate the penetration depth at θ at the maximum intensity. For sample I and II, the maximum of the magnetic Bragg peak occurs at about 10.4° and 11.2° at 150 K, respectively. The corresponding penetration depth is approximately $\xi_{XR} = 10$ nm and $\xi_{XR} = 12.5$ nm, as calculated using the β value at the M_V resonance edge extracted from figure 3.3.a [120]. At these θ values, the transmission of the upper Y layers in sample I and sample II are 96 % and 81 %, respectively. This explains the reduced intensity of the diffraction signal from sample II compared to sample I. A crosscheck of the peak width limitation due to the finite penetration depth of soft x-rays into the sample layer is performed using a very simple approach: it is assumed that the HAF order is well-described by a sinusoidal wave with the measured modulation vector (τ) and an exponential damping $e^{-z/\xi_{XR}}$ over the complete Dy layer of thickness 100 nm. Here, z is the sample depth in nm. The Fourier transformation of this function should represent the measured resonant scattering signal and its width should be comparable to the width of magnetic peak, because the soft x-ray beam propagates in the sample with a comparable damping of its intensity due to the finite absorption. In figure 5.10.b, the Fourier transformations (solid lines) of such sinusoidal functions are presented together with the extracted magnetic peaks (symbols) from the raw data at 150 K. The results agree nicely.

5.3.2. Dynamics of the antiferromagnetic order up to 4 ns

In this section, the results of the synchronous measurements for an absorbed fluence of 1 mJ/cm^2 at different sample temperatures are shown and discussed. On the left panel in figure 5.11, the dynamical response of the Dy magnetic Bragg peak is depicted for sample I after ultrafast optical excitation for three

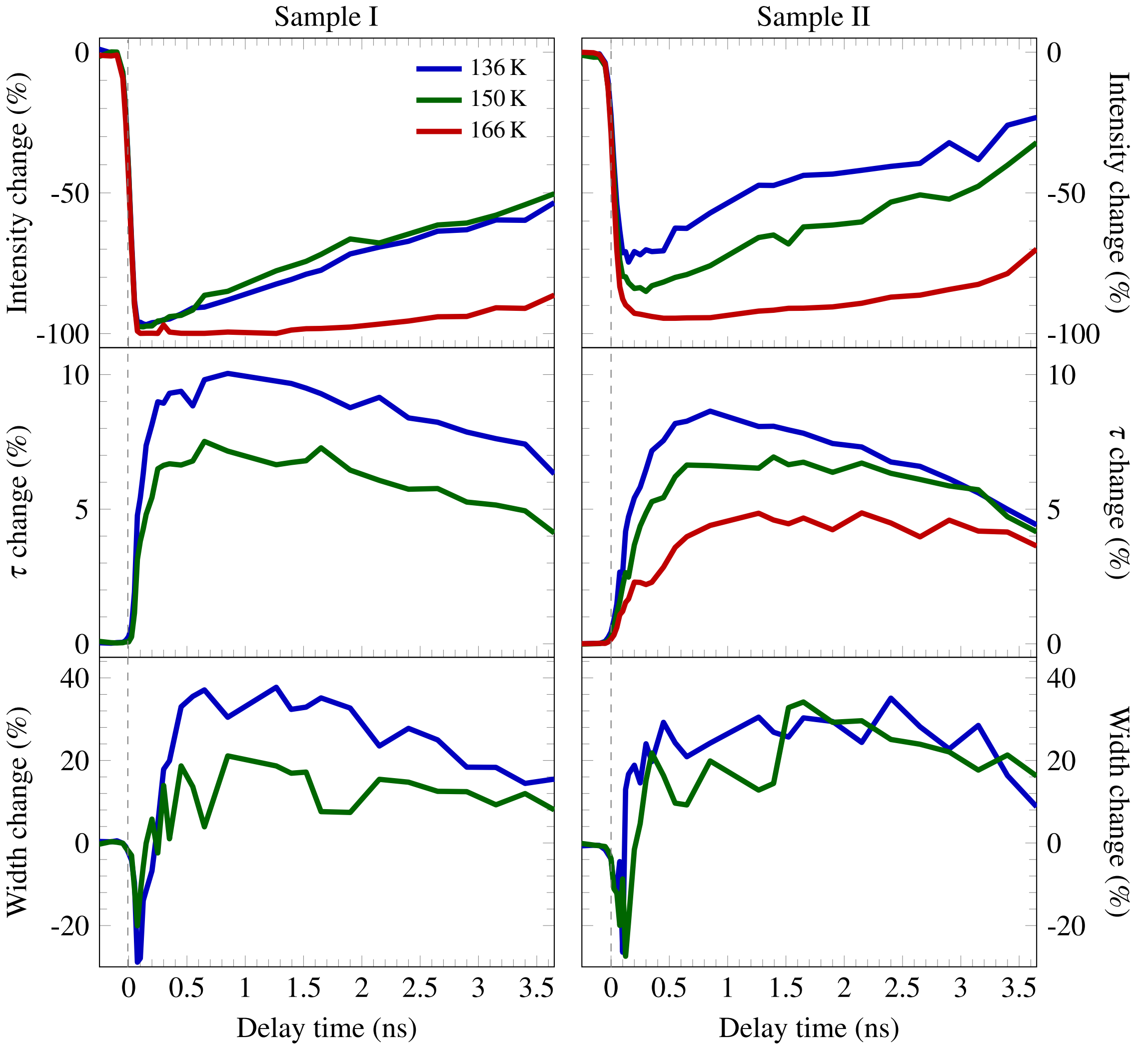

Figure 5.11.: The dynamics of the magnetic Dy Bragg peak parameters: Presented are the transient integrated intensity change, modulation vector change, and peak width change for sample I on the left and for sample II on the right panel. These results are obtained by synchronous RSXD measurements for the absorbed fluence of 1 mJ/cm^2 at different sample temperatures. Some of the results at 166 K are not shown as the magnetic Bragg peak became too weak to be fitted accurately.

different sample temperatures. The reduction of the integrated intensity, I, appears quasi-instantaneously within the time-resolution of the experiment. The initial decrease is independent of the starting temperature and amounts to more than 90%. The integrated intensity recovers to around 50% of its initial value in the low-temperature measurements at 136 and 150 K after about 3.5 ns while only approximately 10% of the initial value is reached at 166 K after 3.5 ns. Two more measurements at 176 K and 178 K are performed for the same excitation fluence, yet they are not shown here because the magnetic peak is already quite weak and seems not to recover within 3.5 ns. The modulation vector, τ, of the Dy magnetic Bragg peak increases after photoexcitation, however, this is not instantaneous and occurs after the maximum reduction of the integrated intensity. It is important to note that the relative change of the modulation vector is on order of 10%, which would correspond to considerably different equilibrium temperatures when using the static calibration measurements in figure 5.7. Surprisingly, the peak width shows interesting dynamics, even though the temperature-dependence of the peak width change is almost independent of temperature in thermal equilibrium. It however changes transiently: One observes a narrowing of the Bragg peak of more than 20% immediately after photoexcitation and after around 250 ps it has gained its initial value again. At later times, it continues to broaden and the maximum peak width change reaches approximately 35%.

In the right panel of figure 5.11, the corresponding results of the analysis of sample II are presented. The observed dynamics closely resemble the response of sample I. In general, one observes slower dynamics and the integrated intensity and modulation vector in sample II are less abruptly changed at early times below 500 ps. The reduced change of these parameters is likely caused by the thicker Y layer on the top of the sample, which absorbs most of the optical pump energy. The comparable dynamics on the time scale later than 500 ps of both samples implies that the HAF recovery dynamics is not affected by a partially direct or purely indirect excitation of the Dy layer.

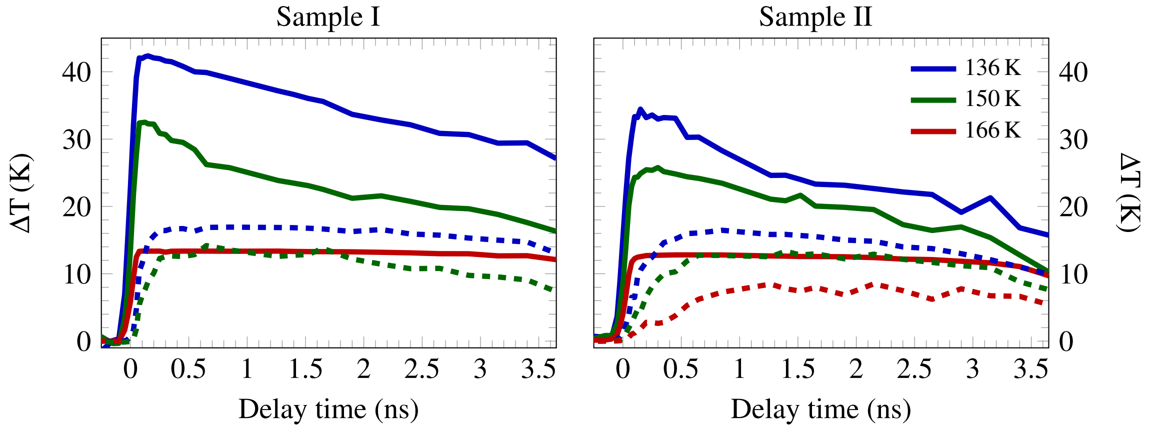

Figure 5.12.: Time-resolved temperature change of the magnetic system that is derived from the relative change of the integrated intensity ΔT_I (solid lines) and modulation vector ΔT_τ (dashed lines) of the magnetic Dy Bragg peak for sample I on the left and for sample II on the right panel. The temperature change is extracted assuming the temperature-dependence of both parameters in thermal equilibrium derived from the static measurements shown in figure 5.7.

Not only the temporal evolution until the maximal change of the integrated intensity and modulation vector differs but also their relative changes are quite different. By means of the static measurements presented in section 5.3.1 (figure 5.7), one can use their temperature-dependencies in thermal equilibrium and apply these to the dynamical measurements in order to infer the corresponding dynamical temperature change, ΔT, after photoexcitation assuming a quasi-equilibrium. The result of such an analysis is presented in figure 5.12 for samples I and II where the extracted values of the temperature change from the relative change of the integrated intensity ΔT_I (solid lines) and the modulation vector ΔT_τ (dashed lines) are shown. These two signatures yield significantly different temperature increases after photoexcitation at these sample temperatures. These differences indicate a non-equilibrium within the localized $4f$ system. Additionally, although the excitation fluence is the same for each sample temperature, one notices a reduced temperature change for the measurements close to T_N for both components of the magnetic Bragg peak. Another feature to notice is that the thermal equilibration of both parameters does not occur within the 3.5 ns time window. In particular, the temperature change remains practically constant after reaching its maximum value at 166 K.

From these transient parameters of the Dy magnetic peak, it is possible to derive a scenario that describes the interaction of the spin system with electronic and phononic degrees of freedom: The laser energy of 1.5 eV excites directly only $5d6s$ electrons. Due to the finite optical penetration depth of the pump light, an exponentially decaying excitation profile with an optical penetration depth of about 24 nm for the laser wavelength of 800 nm develops, which causes a temperature gradient in the sample. Using the advantage that the HAF order is well-described by a sinusoidal wave, one can model the transient magnetic peak by the same approach used in section 5.3.1 assuming a temperature gradient over the depth z within the Dy layer. The temperature gradients $T_I(z,t)$ and $T_\tau(z,t)$ derived from the integrated intensity change $T_I(t)$ and the modulation vector change $T_\tau(t)$ are different as the experimental results shown in figure 5.12 suggest. In order to quantify this, the Fourier transformation of a sinusoidal wave whose intensity (amplitude) describes the order parameter O and whose modulation vector τ describes the inverse periodicity as function of the corresponding temperature profile is performed:

$$HAF = O(T_I(z)) \cdot \sin(\tau(T_\tau(z)) \cdot z) \cdot e^{-z/\xi_{XR}} \; . \tag{5.6}$$

The last term on the right describes the exponential damping of the x-rays in the sample that is important for modelling the measured signal. The corresponding values of O and τ of the temperature profiles are again determined using their temperature-dependencies extracted from the static measurements shown in figure 5.7 in the preceding section. For simplicity we assume exponentially decaying depth profiles. This simple approach is performed the data with the largest changes of all parameters: The results for the experimental data obtained at 136 K for sample I at 75 ps and 650 ps after photoexcitation are shown in figure 5.13 and the origin of the different shapes are explained in the following:

i) 75 ps (panel a and b): The measurements show a reduction of the integrated intensity of around 96%, an increase of the modulation vector of 5%, and a narrowing of the peak width amounting to 29% (see figure 5.11). The model for the measured data starts with the definition of the temperature profiles $T_I(z)$ and $T_\tau(z)$ of the intensity and modulation vector at $t = 75$ ps that are shown in figure 5.13.a. For comparison, the temperature profile of the phonon system T_{ph} as derived from UXRD is also displayed. It is an estimation by means of the TTEM analysis of the experimental results for comparable UXRD measurements presented in section 4.2.2.1. It is important to note here that after 75 ps the $5d6s$ valence electrons are completely in thermal equilibrium with the phonon

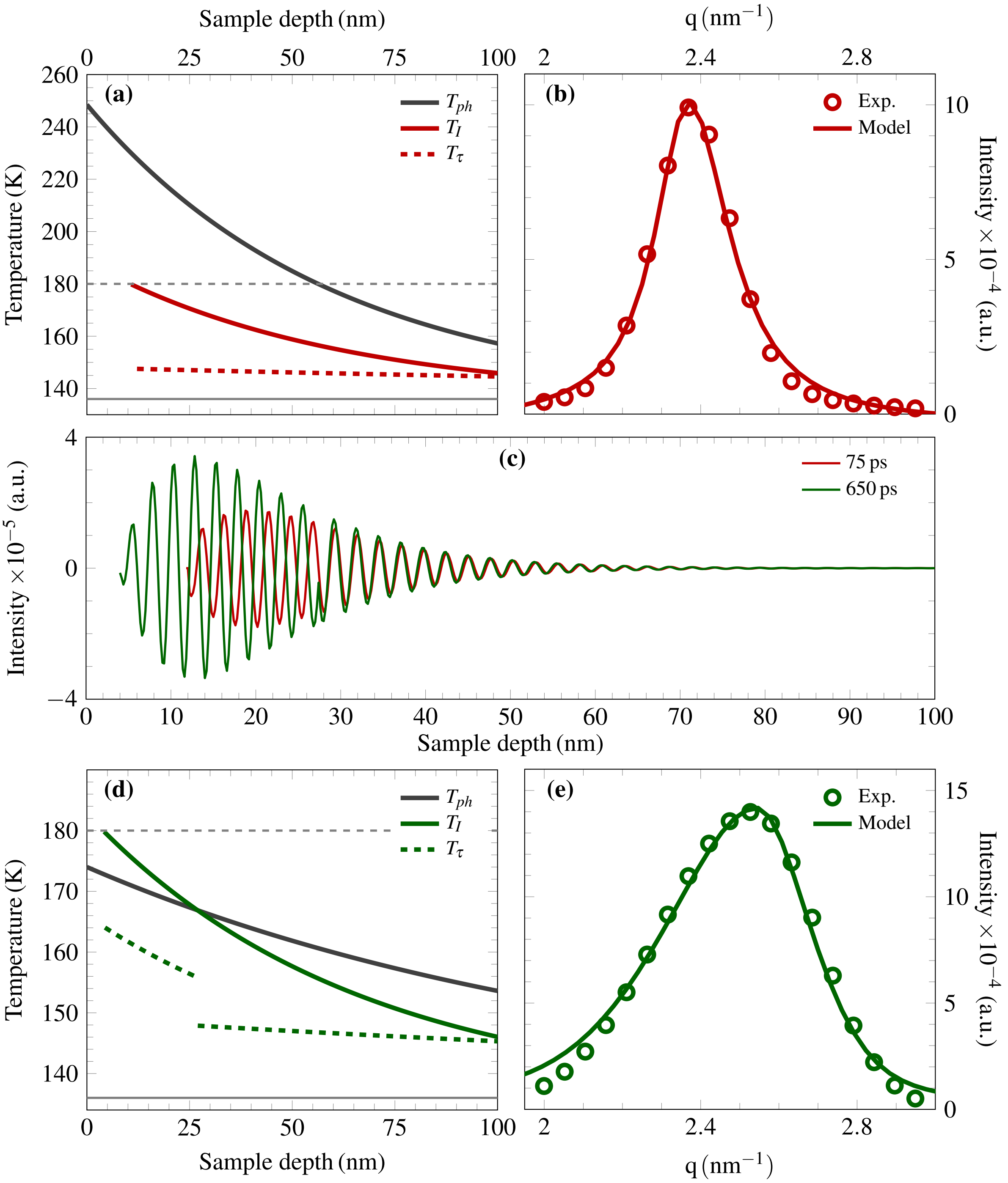

Figure 5.13.: A simple model for the experimental results at 136 K and 75 ps and 650 ps after photoexcitation for sample I: a and d) The temperature profile of intensity T_I and modulation vector T_τ at 75 ps and 650 ps, respectively. The spatial distribution of the phonon temperature is an estimation using the UXRD measurements. c) The sinusoidal wave derived from the model of the probed spin helix over the sample depth, which is derived using equation 5.6 assuming the temperature profiles in a and d. b and e) The resulting peak by Fourier transformation of the sinusoidal wave in c) and the experimental magnetic peak at 75 ps and 650 ps respectively.

system due to the electron-phonon coupling. Therefore, T_{ph} represents also the temperature of the valence electrons. Using equation 5.6, the HAF order in the Dy layer is described as a sinusoidal wave as presented in figure 5.13.c in red. This shows that the peak width to the diffraction signal from the spin helix is determined by the x-ray probe profile. The peak after the Fourier transformation of such a sinusoidal wave is depicted in figure 5.13.b, which describes the experimentally determined magnetic peak of Dy shown by the red symbols nicely.

T_τ does not define a real temperature, yet it is the corresponding temperature in thermal equilibrium for the observed modulation vector of the spin helix. In the approximately first 10 nm, the spin helix completely vanishes because T_l is exceeding T_N. This can be related to a vanishing nesting vector on the Fermi surface that is thought to be the reason for the formation of spin helix in Dy as already mentioned in section 2.2.1. Therefore, also T_τ is not defined. However, the spin helix retains its orientation for the sample depth with $T_l < T_\mathrm{N}$, but with a slightly increased modulation vector. This tiny change of the modulation period may be rationalized by the contracted crystal lattice (compare UXRD data in figure 4.12). The $4f$ and $5d6s$ spins are not coupled anymore, and the orientation of the $4f$ spins are frozen, likely due to the large crystal-field anisotropy energy in Dy, which T_{4f} can not overcome. One can think approximately the spin temperature increase to be given by the average temperature rise is $\Delta T_l = T_l - 136\,\mathrm{K}$. Taking into account the relative contribution to the diffraction signal due to the finite x-ray penetration depth properly, one obtains approximately a temperature rise of 42 K, consistent with the results previously derived in figure 5.12.

ii) 650 ps (panel d and e): The experiments manifest a reduction of the integrated intensity of around 90%, an increase of the modulation vector of 10%, and the broadening of the peak width amounting to 37% (see figure 5.11). Figure 5.13.e displays the extracted magnetic Bragg peak as explained in section 5.2 and the fit result of the peak after the Fourier transformation of the sine wave in figure 5.13.c in dark green. It is derived by taking into account the temperature profiles shown in figure 5.13.d and given by equation 5.6. The raw experimental data that contain the charge reflectivity, and also the peak resulting from the Fourier transformation of the sinusoidal wave in figure 5.13.c in green exhibit a peak splitting, which is shown separately in figure 5.14. The model describes the experimental data nicely.

If one just considers the temperature profiles shown in figure 5.13.d, one might get the impression that the $4f$ electrons carry most of the initially deposited energy as the phonon system cools quite quickly. The energy transfer of the $4f$ spin system is in general possible via all available heat carriers, valence electrons, phonons and magnons. However, when the valence electrons and phonons exceed the temperature of the $4f$ spin system, the only possible channel to cool the $4f$ spin system is via the magnetic system. This in turn means that the dominant channel for heat transport via conduction electrons is not available for cooling the magnetic system because the heat can only be transported to a colder subsystem. As shown in section 2.2.4, the magnetic system contributes only little to the heat conductivity compared to the valence electrons, especially close to the phase transition temperature. For the sample depth of 5 nm, T_l is still higher than T_N and thus no spin helix exists. Between 5 and 25 nm, T_{ph} is lower than T_l leading to a coupling of the $4f$ and $5d6s$ electrons and thus establishing a magnetic order. Here, the

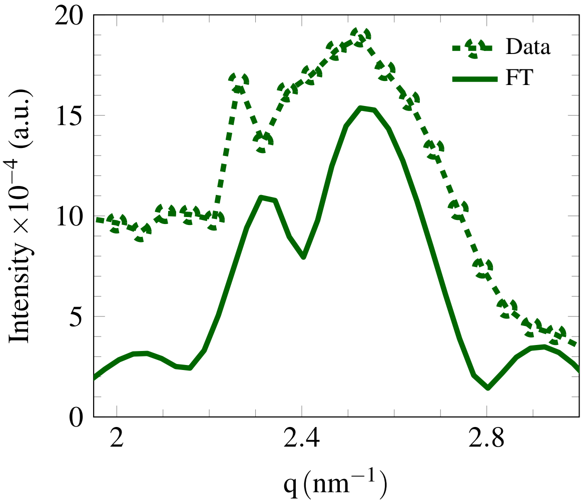

Figure 5.14.: The raw experimental data and the peak by Fourier transformation of the sinusoidal wave shown in figure 5.13.c at 136 K and 650 ps. The peak splitting occurs due to co-existing modulation vectors in Dy layer.

modulation vector does not correspond to T_I that shows a local non-equilibrium within the $4f$ spin system. This is thought to be caused by the magneto-elastic coupling, as the lattice exhibits an average strain of the expanding lattice due to the increase of the phonon temperature and of the contraction due to the excitation of the $4f$ spin system. In the region where $T_I < T_{ph}$, the magnetic system is very similar to the one at 75 ps: The calculated average temperature $\Delta T_I = 40\,\mathrm{K}$ resembles the results shown in figure 5.12 after proper consideration of the relative contribution of the x-ray probe profile. From this modelling it is possible to consider the measured transient integrated intensity as a direct measure of the temperature of the $4f$ spin system but the penetration depth of the probe pulse has to be taken into account for the interpretation.

As in the synchronous measurements no full recovery of the magnetic system is observed up to 4 ns, further measurements have been performed on longer time scales up to 10 µs, which are presented and discussed in the following section. This will allow the investigation of the full magnetic recovery dynamics.

5.3.3. Dynamics of the antiferromagnetic order up to 10 µs

In this section the results of the asynchronous measurements are presented, which supplement the recovery dynamics of the magnetic Bragg peak up to 10 µs after ultrashort photoexcitation. The recovery dynamics of the magnetic order is studied by the variation of the excitation fluence and the start temperature of the sample I. For the former the starting temperature is fixed to $T = 160\,\mathrm{K}$. For the latter the excitation fluence was kept constant to $F_a = 0.35$ and $F_a = 1.4\,\mathrm{mJ/cm^2}$ and the temperature was varied between 130 and 179.5 K in the antiferromagnetic regime of Dy.

5.3.3.1. Fluence study

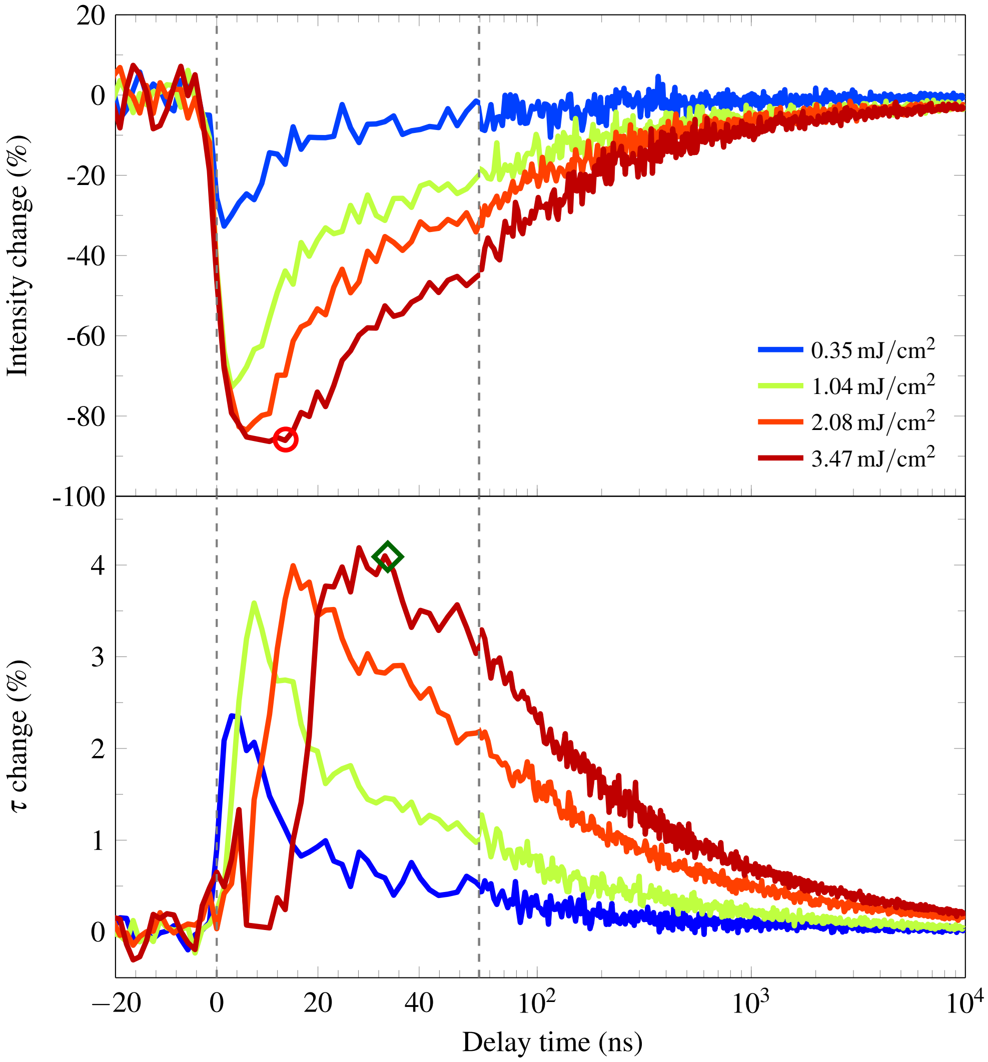

Figure 5.15.: Fluence-dependence of magnetization dynamics at 160 K. The relative temporal response of the integrated intensity (above) and modulation vector (below) of the Dy magnetic peak are displayed for four different fluences. The symbols are the example for the extraction of the maximal change and its time scale of the integrated intensity (red circle) and of modulation vector (green diamond) at the highest fluence. Note that the x-axis has a been divided into a linear and logarithmic part.

The fluence study is performed at the constant temperature of 160 K and the excitation fluence is successively increased from 0.17 up to 3.47 mJ/cm^2. The evolution of the transient integrated intensity and modulation vector of the Dy magnetic Bragg peak is depicted in figure 5.15 for four different excitation fluences. The maximum reduction of the integrated intensity at 0.35 mJ/cm^2 amounts to around 32% and it recovers to half of its initial value within 12 ns. As the excitation fluence is increased, the intensity reduces more and more and reaches a maximum reduction of 86% for $F_a = 3.47$ mJ/cm^2. Additionally, a plateau develops, where the intensity remains constant for almost 14 ns. After the plateau, the intensity starts to recover and attains the half of its initial maximal change at around 51 ns. With increasing fluence the recovery slows down.

The modulation vector increases upon excitation. For the lowest fluence in the figure, the maximum change is 2.4% and it reaches half of its initial value within 12 ns. At 3.47 mJ/cm^2, the modulation vector shows the maximum change after 22 ns and the transient modulation vector stays constant up to 33 ns. Then, the modulation vector is reduced within 120 ns by 50% towards its initial value. It is important to note here that due to the peak splitting of the experimental data as discussed in the previous section, the fit of the modulation vector for the highest fluence of 3.47 mJ/cm^2 between 7 ns and 16 ns needs special attention. The change of the peak width is presented for only two fluences in figure B.2 in the appendix. These results show that the recovery of the magnetic system takes very long time for the lower fluences but even after 10 µs the system is not yet recovered after the excitation with the higher fluences.

In order to interpret the fluence-dependent measurements, a first step is to look at the evolution of the maximum intensity reduction of the magnetic peak and the relative change of its position as function of the absorbed fluence. These are plotted in figure 5.16. The maximal reduction of the integrated intensity and the maximal increase of the modulation vector rises with fluence. They saturate around 82% reduction for the intensity and 4% increase for the modulation vector at high fluences. In figure 5.16.b the recovery time t_r^I and t_r^τ for the intensity and the modulation vector, respectively, are plotted. These times correspond to the time at the end of the observed plateau for the higher fluences and the observed maxima for the lower fluences (see figure 5.15). The fluence-dependence of both time seem to be constant below a threshold fluence of 1 mJ/cm^2 and with increasing fluence a slowing-down becomes evident. Additionally, it seems that between both time scales the relation $t_r^\tau \approx 2.5 \cdot t_r^I$ can be established.

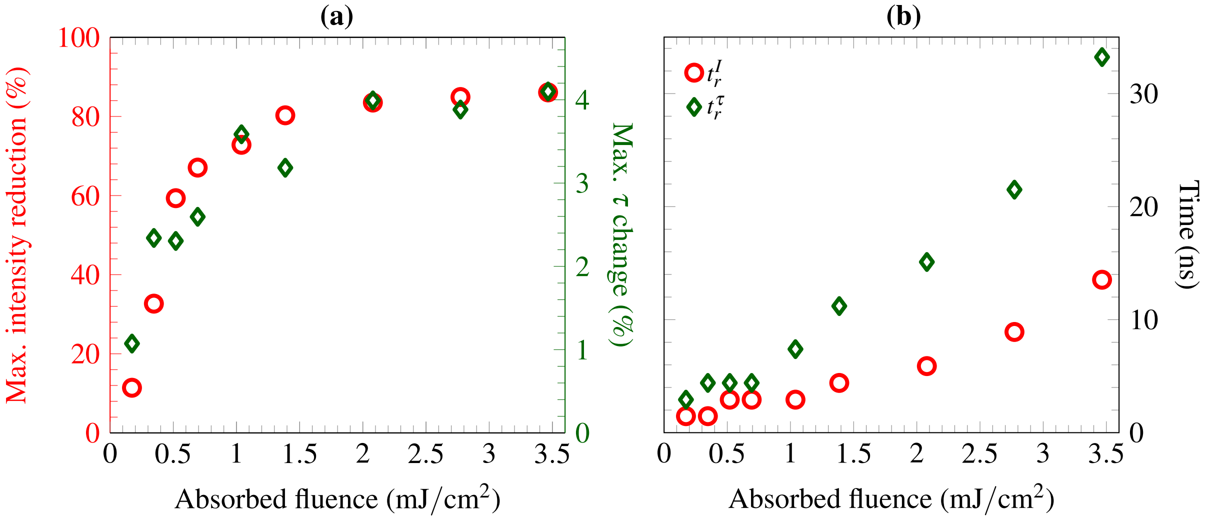

Figure 5.16.: Analysis of the fluence-dependence of magnetization dynamics at 160 K. a) The maximum changes of the integrated intensity and the modulation vector as function of the excitation fluence. b) The time at which the intensity and the modulation vector start to recover.

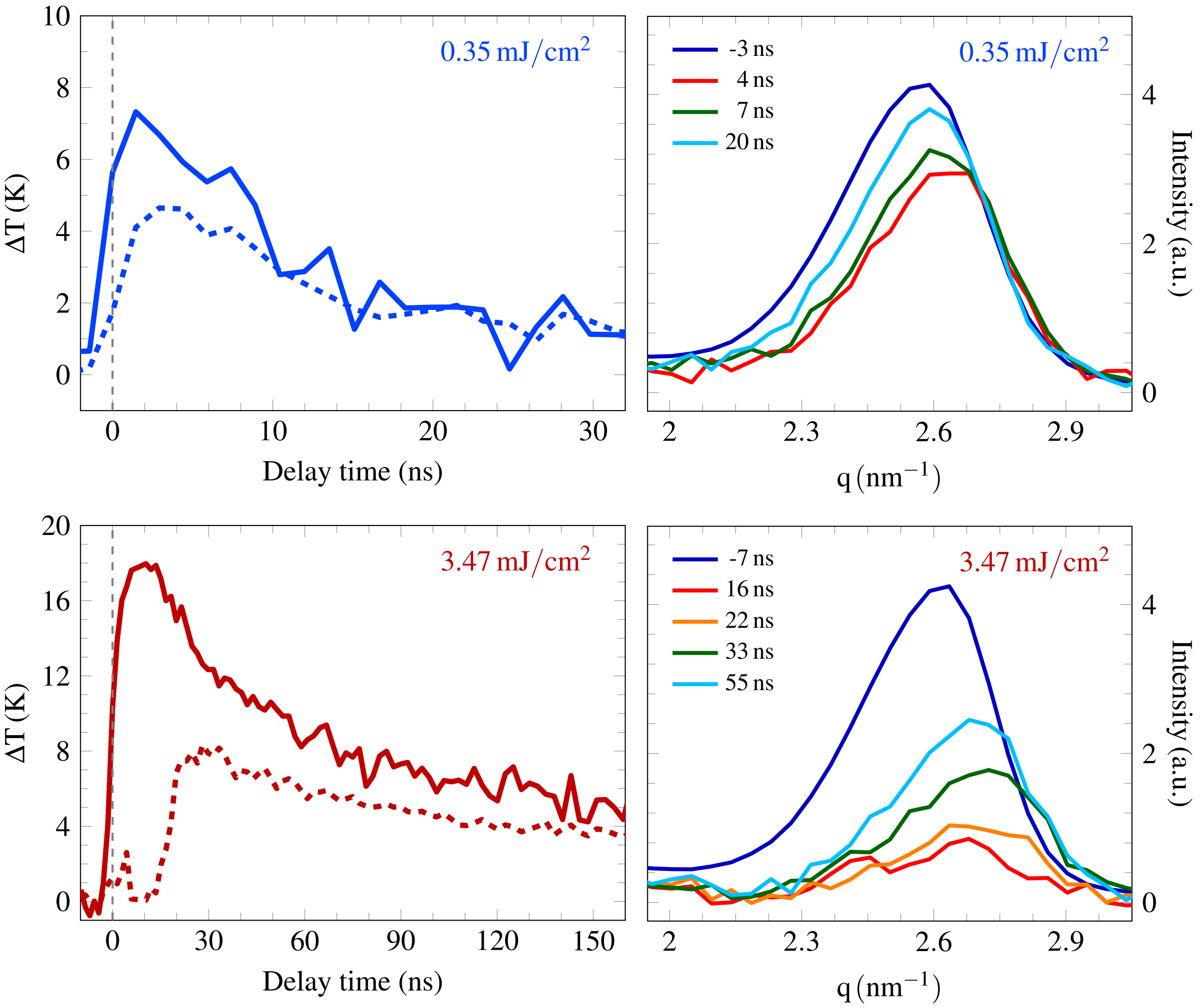

Figure 5.17.: Left panel: Temporal temperature change of the magnetic system that is derived from the relative change of the integrated intensity ΔT_I (solid lines) and the modulation vector ΔT_τ (dashed lines) for the lowest and highest excitation fluences $0.35\,\mathrm{mJ/cm^2}$ and $3.47\,\mathrm{mJ/cm^2}$. Start temperature for these measurements is always $T = 160\,\mathrm{K}$. The procedure is described in the text. Right panel: Raw experimental data of the magnetic Bragg peak at different delay times for the two fluences.

Now the integrated intensity and the modulation vector position can again be converted into a temperature characteristic for the respective subsystem. In figure 5.17 in the left panel the derived temperature change ΔT is plotted as function of delay time for the lowest and highest fluences. The extraction of the temperature rise is applied as in the previous section using the static measurements from figure 5.7 and assuming a quasi-equilibrium. For the lowest excitation fluence, the temperature increase of both subsystems is very similar and both equilibrate after around 10 ns. On the other hand, for the high-fluence excitation ΔT of both parameters is different: The maxima appear at different times where the intensity change responds quicker than the modulation vector. Also the corresponding maximum temperature increase differs by a factor more than 2. The equilibration takes very long, which suggests that the $4f$ electronic system is very disordered after photoexcitation and its recovery is slow. This is already visible in the raw experimental data, from which selected delays are plotted on the right panel of figure 5.17, in order to illustrate that this approach is suitable. For the $0.35\,\mathrm{mJ/cm^2}$ measurements no big changes of the magnetic Bragg reflection can be seen in the raw data as function of delay. This allows the conclusion that even in the directly excited sample depth, the temperature of the $4f$ spin system does exceed T_N, consistent with the previous interpretation of the evolution of the temperature increase. On the contrary, at $3.47\,\mathrm{mJ/cm^2}$ a peak splitting appears at 16 ns, which agrees with the time scale on which the integrated intensity starts to recover. At later times $t > 33$ ps, the peak splitting is not obvious anymore but the peak width is is still broader, which suggests that also there two components coexist. At 33 ns, the modulation vector starts to recover. This manifests a co-existence of the spin helix ordering with different modulation vectors over the sample depth.

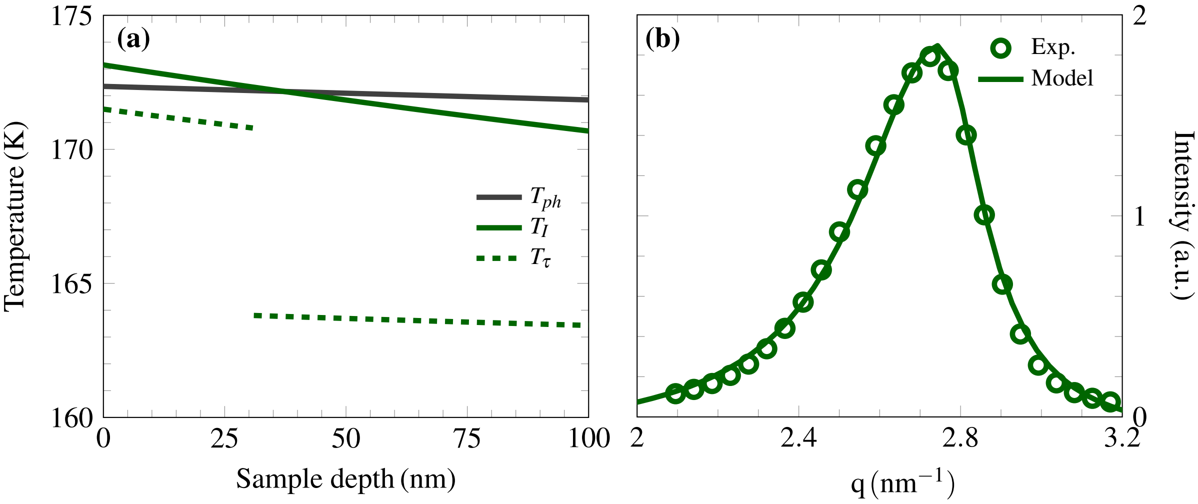

Figure 5.18.: Simple modelling of the magnetic Bragg peak at $t = 33$ ns for the measurement with excitation fluence $F_a = 3.47\,\mathrm{mJ/cm^2}$ following the same approach given by equation 5.6 and discussed in the text. a) The spatial dependence of the temperatures of the $4f$ spin system, T_I for the intensity and T_τ for the modulation vector. The temperature profile of the phonons, T_{ph}, is an estimation from UXRD results. b) The magnetic Bragg peak and the resulting peak by Fourier transformation of the sinusoidal wave that is derived using equation 5.6 with the temperature profiles in a) compared with the experimental data.

Now one can analyze the magnetic peak at 16 ns using the simple model given with the equation 5.6. The peak splitting and the maximum reduction of the intensity around 16 ns indicate a partial rebuilt of a new spin helix order over the excited region where it was initially destroyed because the temperature of the $4f$ spin system with T_I exceeded T_N after the excitation. From the high asymmetry of the peak shape one can directly deduce that over the first few nanometers of the Dy layer the spin helix has not yet regained the antiferromagnetic alignment, which is consistent with the results previously presented in section 5.3.2 in figure 5.13.d and figure 5.14.

The modelling procedure is applied to the magnetic Bragg peak at $t = 33\,\mathrm{ns}$. The corresponding T_I and T_τ are displayed in figure 5.18.a as function of the sample depth. Here, T_{ph} is estimated taking into account the spatial distribution of T_I and also the accompanying structural measurements with UXRD. One clearly sees that the temperature of each subsystem is below T_N over the sample depth of 100 nm. The temperature gradient of the phonon system is very small, although the $4f$ spin system exhibits still a slightly larger temperature gradient. The major difference to the data of 16 ns is that a new spin helix order has formed over the complete excitation depth. However, the modulation vector of this spin helix given by T_τ in the model does not correspond to T_I on this time scale, which confirms the local non-equilibrium within the $4f$ spin system.

From these fluence-dependent experiments and their analysis, it is possible to draw the following conclusions:

i. The time at which the integrated intensity starts to recover, t_r^I, indicates the time when the phonon temperature falls below the temperature of the $4f$ spin system. This is due to the fact that the dominating heat carriers, i.e. the valence electrons, are in thermal equilibrium with the phonons and the cooling of the magnetic system is only possible when the valence electrons are colder than the $4f$ spin system. Additionally, for the excitation fluences that are sufficient to overcome the RKKY exchange interaction by heating the $4f$ spins above T_N, the spin helix is initially destroyed over the directly excited sample depth. When the temperature of the $4f$ spin system falls below T_N at t_r^I the spin helix in the first few nanometers is rebuilt with a considerably larger τ, i.e. a new modulation vector in the part of the directly excited sample depth. These conclusions are based on the observation that the modulation vector reaches its maximum after the intensity has already started to recover. After the completed rebuilding of the spin helix in the directly excited region, the modulation vector also recovers.

ii. The time scales of the recovery of the magnetic system show a critical slowing down effect that can be attributed to the critical behavior of the heat capacity of the magnetic system, C_m. This is consistent with our experimental findings and also with the theoretical studies reported in references [80, 147]. At 160 K in thermal equilibrium, C_m is approximately equal to C_{ph}. Above 160 K C_m rises which is usually fitted by a power law as C_{ph} remains nearly constant. On the other hand, C_m above T_N is quite small. Thus, only limited energy is required to break up the short-range magnetic order. Upon ultrafast excitation always $T_{ph} > T_I$ is observed. Presumably, above a threshold fluence, the maximal energy density is reached for the magnetic system, hence, the rest of the energy is deposited into the phonon system leading to an additional increase of T_{ph}. The phonon system dissipates energy to the substrate with the same rate quasi-independently of the starting temperature. The higher temperature change results in the longer observed time scales required for cooling below T_N and T_I. Therefore, this slows down the magnetic recovery with increasing excitation fluence.

5.3.3.2. Temperature-dependent study

The temperature-dependence is investigated for the two fixed excitation fluences 0.35 and 1.40 mJ/cm^2. The initial temperature is varied between 130 K and 179.5 K in order to study the effect of the starting temperature on the magnetic recovery dynamics. In figure 5.19, the temporal response of the integrated intensity is presented for a temperature series from 130 K up to 179 K after photoexcitation for the fixed excitation fluence of 1.4 mJ/cm^2. At 130 K, the reduction of the intensity is around 50% and the recovery to half of the initial value occurs within 15 ns. With increasing temperature up to 175 K, the reduction of the intensity increases as well, however, above 175 K the maximum reduction decreases slightly. This feature is expected from the static characterization of the integrated intensity because close the second order phase transition the intensity decreases due to fluctuations. Thus, the expected changes due to the excitation of the magnetic system close to T_N are expected to be small. However, at 178 K and 179 K, a plateau forms as also has been discussed in the previous section. This plateau where the intensity does not change exists for the very long time up to several 100 ns. This is accompanied by the observation that for the temperatures close to T_N the integrated intensity does not recover to the initial value within 10 µs. The absolute change of the integrated intensity and the modulation vector is shown in figures B.3 and B.4 in the appendix, respectively, together with the results of the temperature series at $F_a = 0.35\,\mathrm{mJ/cm^2}$.

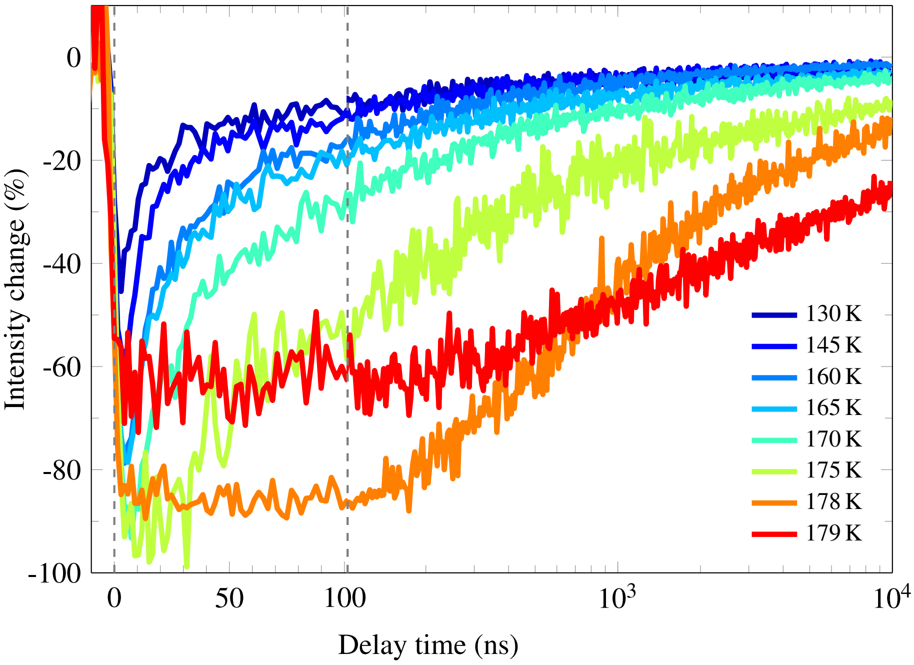

Figure 5.19.: Temperature-dependence of the integrated intensity at the fixed excitation fluence of 1.4 mJ/cm^2. The temporal response of the integrated intensity of the magnetic Bragg peak is presented for different start temperatures between 130 and 179 K. Note that the x-axis has a been divided into a linear and logarithmic scale part.

In figure 5.20 the raw experimental data of the magnetic Bragg reflection for different delay times at 170 K and 179 K are shown. At 170 K the magnetic Bragg peak is at 10 ns very weak and the shift

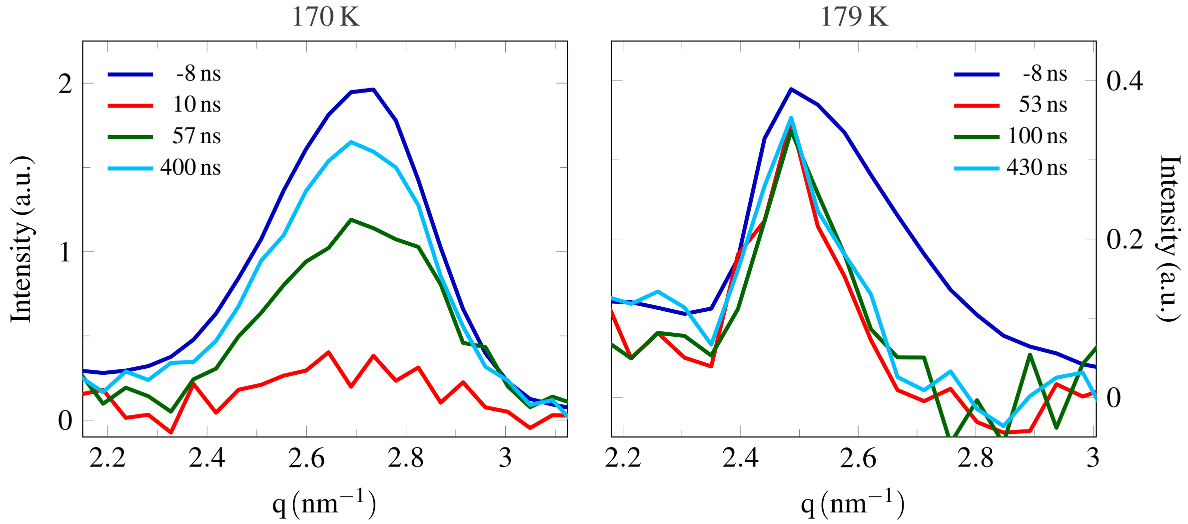

Figure 5.20.: The raw experimental data of the magnetic Bragg peak before and at different delay times after photoexcitation for the excitation fluence of $1.4\,\mathrm{mJ/cm^2}$ at 170 K (left) and 179 K (right).

of the peak position cannot be clearly determined. The behavior at $T = 179\,\mathrm{K}$ is quite different: The magnetic peak before photoexcitation is quite asymmetric. In addition, its peak position is reduced compared to the one that is measured at the phase transition in the static measurements presented in section 5.3.1. After photoexcitation, the position of the magnetic peak decreases further and becomes narrower. The scattering intensity shows no change and the position remains constant up to 430 ns. The same response occurs in the measurements for the start temperatures $T \geq 178\,\mathrm{K}$ and also for the measurements at $F_a = 0.35\,\mathrm{mJ/cm^2}$. This might be caused by the fact that the system does not completely recover between two subsequent 1 kHz laser pulses and the magnetic system remains disordered close to T_N.

The systematic slowing down of the recovery dynamics of the $4f$ spin system after photoexcitation is observed as the start temperature is increased towards T_N at fixed fluence, which suggests that the critical exponent of the magnetic recovery dynamics of Dy can be determined this way. From the discussion in the previous sections, this is the time scale at which the integrated intensity of the magnetic Bragg peak starts to recover and corresponds to the time of the relaxation of the phonon and the $4f$ spin system temperature below T_N. On the other hand, the time scale at which the modulation vector starts to recover indicates the complete rebuilt of a new spin helix in the directly excited region of the Dy layer. Using these indications, one can calculate the dynamical critical exponent of Dy taking the dependencies of t_r^I or t_r^τ on the reduced temperature, $\epsilon = |(T - T_\mathrm{N})/T_\mathrm{N}|$, as proposed in section 2.4. This is only possible if the assumption that both time scales indicate equilibration time of the magnetic system is correct. Figure 5.21 presents t_r^I as function of the reduced temperature for both temperature series at 1.40 and $0.35\,\mathrm{mJ/cm^2}$. According to theory, a critical exponent of 1.34 is expected for the equilibration time of a XY magnet such as Dy, which has been given in section 2.4 by equation 2.24. The parameter A

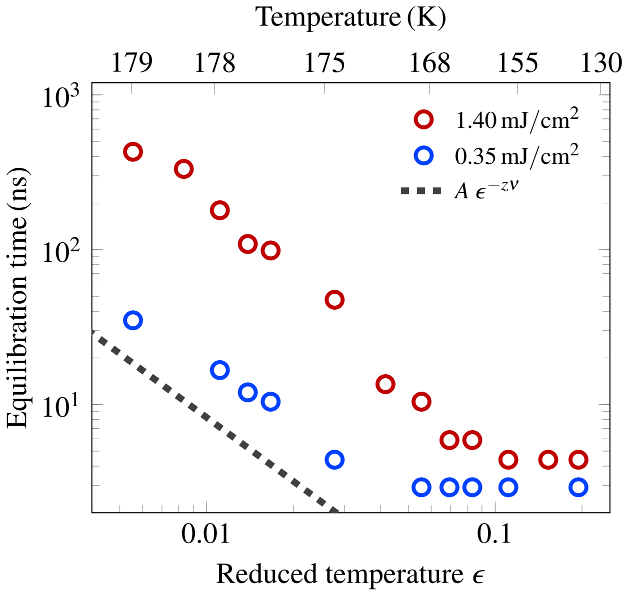

Figure 5.21.: Time t_r^I at which the integrated intensity of the magnetic Bragg peak starts to recover as function of the reduced temperature, $\epsilon = |(T - T_\mathrm{N})/T_\mathrm{N}|$, for the temperature-dependent measurements for 1.40 and $0.35\,\mathrm{mJ/cm^2}$ absorbed excitation fluences. The dashed black line shows the power law given by equation 2.24.

depends on the fluence and essentially serves as an offset for the fitting of the data. Figure 5.21 shows that indeed the experimental results are consistent with the theory of critical phenomena and Dy indeed exhibits the critical dynamical exponent of $z\nu \approx 1.37$. The data points for large values of ϵ, that is for low temperatures far away from T_N, are likely limited by the time resolution of the asynchronous measurements. This clearly indicates that far away from the phase transition temperature one can no longer speak of critical phenomena, in other words, the sample is not strongly phase separated and the transition not limited by a divergence of the order parameter any more as the domains are sufficiently large.

The results from the temperature-dependent series are in agreement with the fluence-dependent measurements. In addition very long time scales occur in the data. These become important for starting temperatures very close to T_N and the very small initial temperature gradient of the $4f$ spin system leads to an additional slowing down of the recovery time of the magnetic system, presumably connected to the limited specific heat capacity of the magnetic system above T_N.

6. Comparison of RSXD and UXRD results

In this chapter, the static and dynamical results of the RSXD and the UXRD experiments of the Dy sample I are compared. This allow the crosscheck the coupling between the magnetic and structural properties. The experimental conditions such as temperature and the laser parameters, excitation fluence, wavelength, and pulse duration for these investigations are similar, however, the RSXD experiments are performed at the $\mathrm{M_V}$ absorption edge of Dy, which limits the probe depth to a few tens of nanometers whereas the UXRD experiments probe the complete Dy layer. As first in this chapter, the close relation of the magnetic and structural properties is demonstrated in thermal equilibrium using the static measurements. Afterwards, the dynamical results of both techniques are compared by analysis of the equilibration time t_{eq} as dynamical critical phenomenon. Additionally, for the Gd sample, a similar analysis is performed.

6.1. Thermal equilibrium

During the sample characterization, the structural and magnetic Bragg peaks of Dy are measured at start temperatures in the antiferromagnetic phase. The structural measurements yield the out-of-plane lattice constant and the magnetic Bragg reflection provides a measure of the order parameter because the integrated intensity is proportional to the square of the order parameter, $I \propto O^2$ [144], which is given by the sublattice magnetization $O = M_S$ in the antiferromagnetic materials as mentioned in the previous chapter. Additionally, the turn angle ϕ between the magnetic moments of neighboring $4f$ electrons along the c-axis is derived from the modulation vector of the magnetic Bragg peak and the lattice constants. In figure 6.1, these three parameters are plotted in the temperature range between 130 K and 186 K. Decreasing the temperature from T_N, the order parameter increases and the lattice expands whereas the interplanar turn angle decreases. The anomalous expansion of the lattice is associated to the helical AFM order caused by the exchange magnetostriction, as already given in equation 2.13 [61, 62]. Now, the experimental results in thermal equilibrium can be compared to this model. In equation 2.13, $\varepsilon_m = (c - c_{ph})/c$ is the strain due to the magnetic order, where c_{ph} is the lattice constant where only the phonons contribute to the thermal expansion. Equation 2.13 relates it to the sublattice magnetization through the interplanar turn angle, the change of the exchange interaction $d\mathscr{J}/dc$ upon infinitesimal expansion and the effective elastic constant. The calculated $\varepsilon_m^{\mathrm{Dy}}$ shown in figure 6.2.a is derived from measured lattice constants and obtaining c_{ph} from the extrapolation of the lattice constant in the PM phase towards low temperatures. The temperature-dependence of $\varepsilon_m^{\mathrm{Dy}}$ is determined by the order parameter as

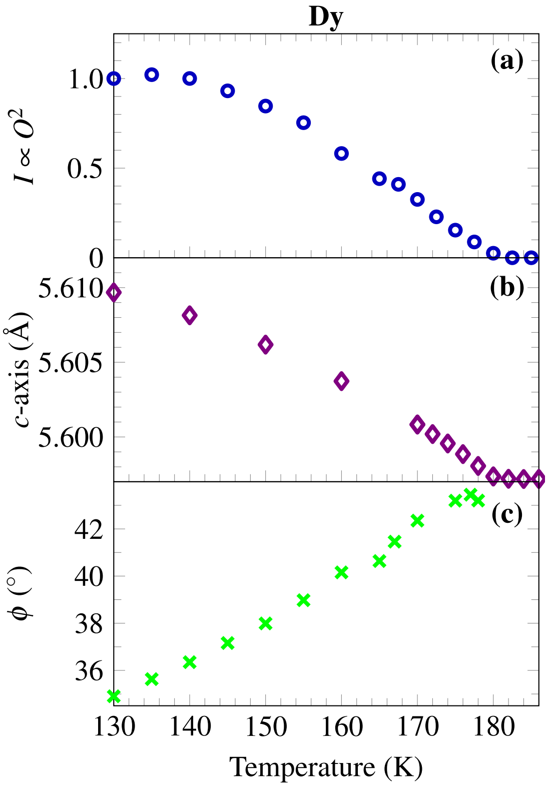

Figure 6.1.: Equilibrium properties of Dy: a) the integrated intensity of the magnetic Bragg peak, b) the lattice constant, and c) the interplanar turn angle of the magnetic moments of the $4f$ electrons as function of temperature.

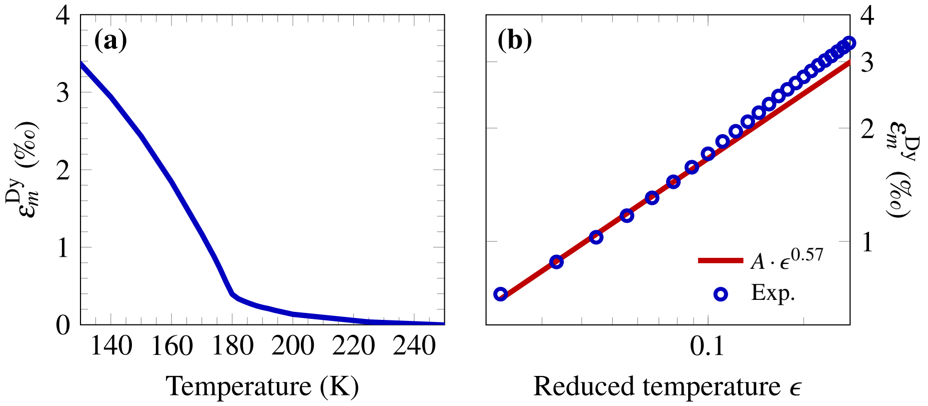

Figure 6.2.: a) The magnetic strain in Dy is calculated with $\varepsilon_m^{\mathrm{Dy}} = (c - c_{ph})/c$ using the measured lattice constants shown in figure 6.1.b. b) The magnetic strain as function of the reduced temperature $\epsilon = |(T - T_{\mathrm{N}})/T_{\mathrm{N}}|$. The red line shows the fit with a power function with an exponent $s = 0.57$.

suggested in equation 2.13. T_{N} is visible as a kink around 180 K and even ≈ 40 K above T_{N} the magnetic strain has not yet reached zero, which highlights the influence of the short-range magnetic order in Dy. In figure 6.2.b, $\varepsilon_m^{\mathrm{Dy}}$ is plotted as function of the reduced temperature $\epsilon = |(T - T_{\mathrm{N}})/T_{\mathrm{N}}|$ assuming a power law of the form $\varepsilon_m^{\mathrm{Dy}} = A \cdot \epsilon^s$ with the static critical exponent s for the magnetic strain. The fit of the power law reveals an exponent of $s = 0.57$. This shows the strong connection between the magnetic strain and the sublattice magnetization because they both exhibit the power law as function of the reduced temperature with the exponents on the same order.

Using the same principle, one can determine the exponent s for Gd whose temperature-dependence of the lattice constant is also measured by static UXRD in this work and was shown in figure 4.19.a. In figure 6.3.a the calculated magnetic strain in Gd $\varepsilon_m^{\mathrm{Gd}} = (c - c_{ph})/c$ is shown. It exhibits a critical behavior close to $T_{\mathrm{C}} \approx 295$ K. The short-range magnetic order close to T_{C} in the PM phase is stronger in comparison to the previously discussed magnetic strain in Dy. In figure 6.3.b the calculated magnetic strain of Gd is plotted as function of the reduced temperature $\epsilon = |(T - T_{\mathrm{C}})/T_{\mathrm{C}}|$ that is fitted by a power law. The resulting critical exponent $s = 0.42$ is in agreement with the static critical exponent β of the order parameter in the universality class of the XY and Heisenberg magnets, which is realized for the magnetization of Gd. Considering equation 2.13, the deviation from $\beta \approx 0.42$ as obtained for Dy in sample I, might be caused by the interplanar turn angle ϕ, which likely results in a small additional modification of the interplanar exchange interaction in Dy.

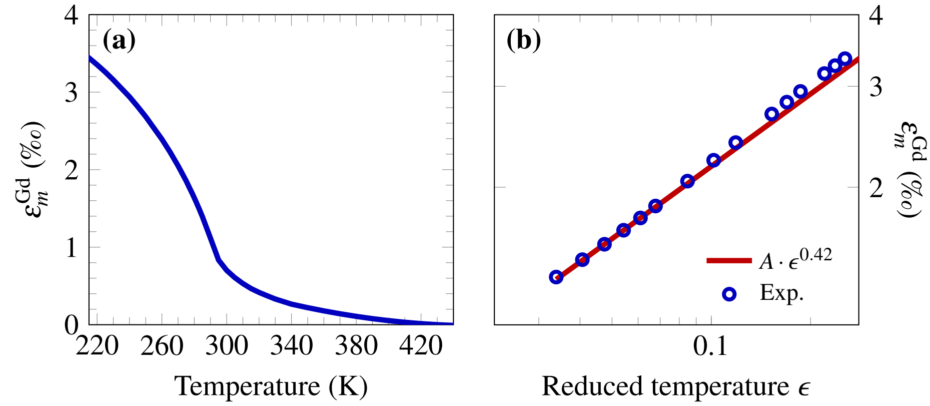

Figure 6.3.: a) The magnetic strain in Gd with $\varepsilon_m^{\mathrm{Gd}} = (c - c_{ph})/c$ using the measured lattice constants shown in figure 4.19. b) The magnetic strain as function of the reduced temperature $\epsilon = |(T - T_{\mathrm{C}})/T_{\mathrm{C}}|$. The red line shows the fit results the power function with an exponent of $s = 0.42$.

6.2. Dynamical critical exponent

Time-resolved RSXD experiments yield the time t_r^I at which the integrated intensity of the magnetic Bragg peak of Dy starts to recover. This time is given by the simple model explained in sections 5.3.2 and 5.3.3 as the time at which the temperature of the magnetic system T_m given by the integrated intensity falls below T_N. On the other hand, the temperature of the phonon system is expected to be $T_{ph} < T_m < T_\mathrm{N}$. Therefore, the time t_r^I is the equilibration time, which was determined for each fluence and start temperature and yields the dynamical critical exponent as shown in figure 5.21. On the other hand, the measured transient strain and the change of the peak width by the UXRD show a characteristic time for each start temperature that are identified by minima of the strain and the required time of the peak width to relax back to its initial value (see figure 4.12). This time was identified as the equilibration time between the temperature changes of the phononic and magnetic systems, $\Delta T_{ph} = \Delta T_m$ from the analysis of the data with the TTEM. After this time, ΔT_{ph} decreases down to ΔT_m (see figure 4.15). Now, all equilibration times determined by RSXD and UXRD are plotted together in figure 6.4 as function of the reduced temperature ϵ. According to the theory introduced in section 2.4, a dynamical critical

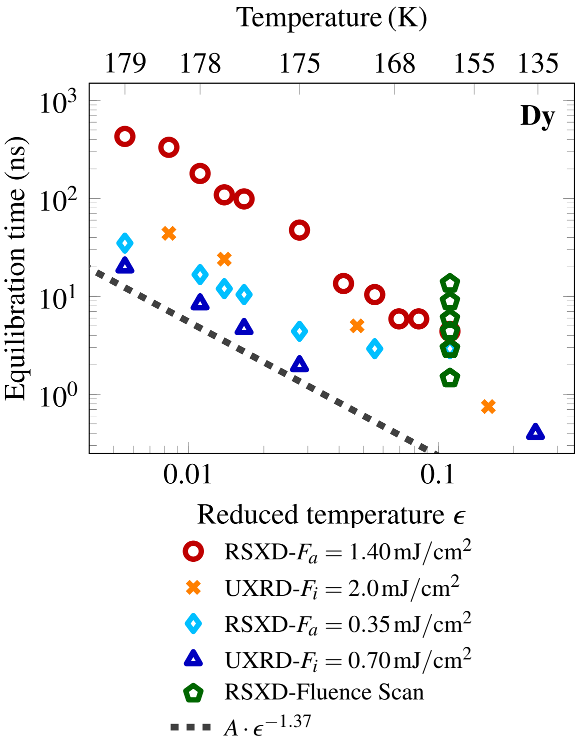

Figure 6.4.: Equilibration time t_{eq} as function of the reduced temperature $\epsilon = |(T - T_\mathrm{N})/T_\mathrm{N}|$ for Dy. The equilibration time is obtained from RSXD and UXRD experiments. The results show that a single dynamical critical exponent $z\nu \approx 1.37$ is obtained as indicated by the dashed line.

exponent of around $z\nu \approx 1.34$ is expected for the XY magnets given by equation 2.24. Not only the RSXD experiments but also the UXRD results are consistent with this theory as the fit gives $z\nu \approx 1.37$. The results are also consistent with the experiments shown in figure 2.14 obtained from a completely different experimental method.

From similar UXRD experiments on Gd, one can easily extract t_{eq} from the temperature changes of the phononic and the magnetic systems (see figure 4.23.b) in order to determine the dynamical critical exponent of another XY magnet. Figure 6.5 displays the equilibration time as function of the reduced

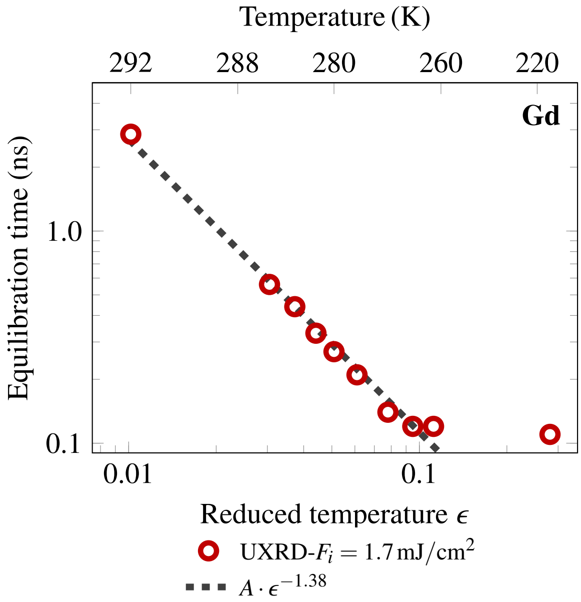

Figure 6.5.: Equilibration time t_{eq} as function of the reduced temperature $\epsilon = |(T - T_\mathrm{C})/T_\mathrm{C}|$ for Gd. The equilibration time is derived from UXRD. The results imply a dynamical critical exponent $z\nu \approx 1.38$.

temperature for Gd. The fit with the power law yields $z\nu \approx 1.38$ that is in good agreement with the dynamical critical exponent of Dy.

The very good agreement of the results obtained from the RSXD and the UXRD experiments shows that the results of UXRD experiments with the analysis by the TTEM allows correctly inferring the properties of the magnetic system.

7. Conclusion

In this dissertation systematic investigations of the structural and magnetic recovery dynamics in the two heavy rare-earth metals Dy and Gd were presented. The experimental results were obtained by two time-resolved x-ray diffraction techniques, UXRD and RSXD and the experiments were performed in the antiferromagnetic state of Dy where Dy exhibits long-range helical magnetic order, and in the ferromagnetic state of Gd.

From the UXRD studies, the transient strain is obtained with a pronounced different behavior depending on the sample temperatures in Dy and Gd. Only an expansion is observed in the PM phase, and only contraction of the lattice at the temperatures far below T_N and T_C, respectively. At temperatures close to the phase transition, a reduced expansion and contraction is observed for different delay times because of the competition between the positive and negative strain driven by phononic and magnetic stress due to photoexcitation. The transient strain suggests a non-equilibrium between these subsystems, in particular upon a direct excitation of the rare-earth layer. The initial energy densities $\Delta\rho^Q_{ph}$ and $\Delta\rho^Q_m$ are derived using the two-thermal-energies-model [24]. Assuming the equilibrium heat capacities to be valid, this defines the transient temperature changes of the individual subsystems ΔT_{ph} and ΔT_m. It always shows immediately after excitation that $\Delta\rho^Q_{ph} > \Delta\rho^Q_m$ and $\Delta T_{ph} > \Delta T_m$. The cooling of the phonon system starts directly after the excitation but cooling the magnetic system is much slower and strongly depends on the start temperature. In Gd 31% of the initial energy density is deposited in magnetic system at $T = 212\,\mathrm{K}$ that decreases down to 11% around T_C. In Dy 27% of the initial energy density is deposited in magnetic system at $T = 151.5\,\mathrm{K}$ and it decreases down to 6% around T_N. The transient temperatures are equilibrated after the time t_{eq}, which is slowed down at temperatures approaching the phase transition temperature. For example, in Gd $t_{eq} = 110\,\mathrm{ps}$ at $T = 212\,\mathrm{K}$ and it increases to $t_{eq} = 560\,\mathrm{ps}$ at $T = 286\,\mathrm{K}$. In Dy $t_{eq} = 750\,\mathrm{ps}$ at $151.5\,\mathrm{K}$ and $t_{eq} = 24\,\mathrm{ns}$ at $177.5\,\mathrm{K}$. After the equilibration time, a temperature inversion is observed that enables the heat transport from magnetic system to the phonon system. The recovery dynamics is faster in Gd sample than in Dy samples.

Using the UXRD measurements, the heat transport through multilayer systems on the nanoscale consisting of the rare-earth Dy and non-magnetic metal layers was investigated. In this complex heat flow, the transient temperatures of all layers including the temperatures of the phonon and magnetic systems in Dy are obtained quantitatively. This shows a faster energy dissipation from the top Y layer to the Dy layer due to the existence of the magnetic order in the AFM phase of Dy. Additionally, a reduced heat transport is observed through the layers due to the energy density stored in the magnetic system. Furthermore, the simulations showed that the total energy density in Dy obtained from the TTEM can be simulated and the observed strain deviates from simulated strain because of the competition of the expansive and contractive strain driven by the excitations of the phonon and the magnetic systems.

The study of the magnetic structure directly by RSXD gives the resulting transient changes of the modulation vector and the integrated intensity of the magnetic Bragg peak of Dy. The transient changes of these parameters yield the time scales for the maximum changes and recovery times. An instantaneous reduction of the integrated intensity is always observed but the modulation vector increases slowly and reaches the maximum change always after the integrated intensity starts to recover. A simple model is devoloped by the Fourier transformation of a sinusoidal wave where the amplitude characterizes the order parameter and the wavevector is given by the modulation vector of the HAF order in Dy. This is used to explain the transient experimental data and indicates a local non-equilibrium of the $4f$ spin system due to the fact that the changes of the modulation vector and integrated intensity differ spatially in the sample. These experimental results and the model agree well with depth-resolved RSXD measurements in Dy [120], although the sample used in reference [120] was directly grown on the substrate without buffer layers unlike the samples used in thesis. Furthermore, the dynamics shows that the observed time scales for these pronounced changes depend strongly on the excitation fluence and the start temperature. A systematical slowing down of the recovery dynamics after the initial loss of the magnetic order is detected as the sample temperature approaches T_{N}. The slowing down of the time on which the integrated intensity starts to recover follows the theoretically predicted dynamical critical exponent for XY magnets with $z\nu \approx 1.37$. The comparison of the results from the RSXD with the UXRD indicates that similar dynamics are observed in the transient lattice strain and the integrated intensity of the magnetic Bragg peak of Dy. This provides the opportunity to determine the dynamical critical exponent from the equilibration time t_{eq} determined by UXRD. This additionally shows that the TTEM successfully describes the transient temperatures of the subsystems. A similar analysis for ferromagnetic Gd gives $z\nu \approx 1.38$, which agrees well with theory.

Both experimental techniques yield in agreement that the magnetic recovery dynamics depend strongly on the initial distribution of the deposited energy density, which is the consequence of the large magnetic heat capacity that results in a critical behavior around the phase transition temperature [147] and is also responsible for slow cooling of the phonon system.

The faster recovery dynamics of Gd in contrast to Dy likely is related to the different sample structure: Gd is directly grown on the substrate, which provides a faster cooling of the phonon system due to enlarged heat conductivity of the substrate compared to the reduced interfacial thermal conductivities in Dy sample. This leads to a slower cooling of the phonon system in Dy through the layers to the substrate. This can be seen from the dynamics in the PM phase of both rare-earth metals, where only the phonon system is excited due to the absence of the magnetic order. In the future, it would be interesting to repeat the characterization of the Dy dynamics by UXRD and RSXD for a film deposited directly on a substrate or at least in a structure with less heat transport barriers between the film and the substrate.

Bibliography

[1] A. Eschenlohr et al. “Ultrafast spin transport as key to femtosecond demagnetization”. In: *Nature Materials* 12 (2013), pp. 332–336.

[2] C. von Korff Schmising et al. “Imaging Ultrafast Demagnetization Dynamics after a Spatially Localized Optical Excitation”. In: *Phys. Rev. Lett.* 112 (2014), p. 217203.

[3] Emrah Turgut et al. “Stoner versus Heisenberg: Ultrafast exchange reduction and magnon generation during laser-induced demagnetization”. In: *Phys. Rev. B* 94 (2016), p. 220408.

[4] Andrei Kirilyuk, Alexey V. Kimel, and Theo Rasing. “Ultrafast optical manipulation of magnetic order”. In: *Rev. Mod. Phys.* 82 (2010), pp. 2731–2784.

[5] R.J. Elliott. *Magnetic properties of rare earth metals*. Plenum Press, 1972.

[6] M. A. Ruderman and C. Kittel. “Indirect Exchange Coupling of Nuclear Magnetic Moments by Conduction Electrons”. In: *Physical Review* 96.1 (1954), pp. 99–102.

[7] Tadao Kasuya. “A Theory of Metallic Ferro- and Antiferromagnetism on Zener’s Model”. In: *Progress of Theoretical Physics* 16.1 (1956), pp. 45–57.

[8] Kei Yosida. “Magnetic Properties of Cu-Mn Alloys”. In: *Physical Review* 106.5 (1957), pp. 893–898.

[9] M. Doerr *, M. Rotter, and A. Lindbaum. “Magnetostriction in rare-earth based antiferromagnets”. In: *Advances in Physics* 54.1 (2005), pp. 1–66.

[10] J. Güdde et al. “Magnetization dynamics of Ni and Co films on Cu(001) and of bulk nickel surfaces”. In: *Phys. Rev. B* 59 (1999), R6608–R6611.

[11] M. Cinchetti et al. “Spin-Flip Processes and Ultrafast Magnetization Dynamics in Co: Unifying the Microscopic and Macroscopic View of Femtosecond Magnetism”. In: *Phys. Rev. Lett.* 97 (2006), p. 177201.

[12] E. Carpene et al. “Dynamics of electron-magnon interaction and ultrafast demagnetization in thin iron films”. In: *Phys. Rev. B* 78 (2008), p. 174422.

[13] Marko Wietstruk et al. “Hot-Electron-Driven Enhancement of Spin-Lattice Coupling in Gd and Tb $4f$ Ferromagnets Observed by Femtosecond X-Ray Magnetic Circular Dichroism”. In: *Phys. Rev. Lett.* 106 (2011), p. 127401.

[14] B Frietsch et al. “Disparate ultrafast dynamics of itinerant and localized magnetic moments in gadolinium metal”. In: *Nature Communications* 6.1 (2015), p. 8262.

[15] A. Melnikov et al. “Nonequilibrium Magnetization Dynamics of Gadolinium Studied by Magnetic Linear Dichroism in Time-Resolved $4f$ Core-Level Photoemission”. In: *Phys. Rev. Lett.* 100 (2008), p. 107202.

[16] Robert Carley et al. “Femtosecond Laser Excitation Drives Ferromagnetic Gadolinium out of Magnetic Equilibrium”. In: *Phys. Rev. Lett.* 109 (2012), p. 057401.

[17] Nele Thielemann-Kühn et al. “Ultrafast and Energy-Efficient Quenching of Spin Order: Antiferromagnetism Beats Ferromagnetism”. In: *Phys. Rev. Lett.* 119 (2017), p. 197202.

[18] L. Rettig et al. “Itinerant and Localized Magnetization Dynamics in Antiferromagnetic Ho”. In: *Phys. Rev. Lett.* 116 (2016), p. 257202.

[19] B Koopmans et al. “Explaining the paradoxical diversity of ultrafast laser-induced demagnetization”. In: *Nature Materials* 9.3 (2010), pp. 259–265.

[20] M. C. Langner et al. “Scattering bottleneck for spin dynamics in metallic helical antiferromagnetic dysprosium”. In: *Phys. Rev. B* 92 (2015), p. 184423.

[21] David G. Cahill et al. “Nanoscale thermal transport. II. 20032012”. In: *Applied Physics Reviews* 1.1 (2014), p. 011305.

[22] M. Woerner et al. “Ultrafast structural dynamics of perovskite superlattices”. In: *Applied Physics A* 96.1 (2009), p. 83.

[23] Florian Quirin et al. “Structural dynamics in FeRh during a laser-induced metamagnetic phase transition”. In: *Phys. Rev. B* 85 (2012), p. 020103.

[24] A. von Reppert et al. “Persistent nonequilibrium dynamics of the thermal energies in the spin and phonon systems of an antiferromagnet”. In: *Structural Dynamics* 3.5 (2016), p. 054302.

[25] Jakob Bohr, Doon Gibbs, and Kegang Huang. “X-ray-diffraction studies of the magnetic state of thulium”. In: *Phys. Rev. B* 42 (1990), pp. 4322–4328.

[26] M. K. Sanyal et al. “Resonance magnetic x-ray-scattering study of erbium”. In: *Phys. Rev. B* 49 (1994), pp. 1079–1085.

[27] Holger Ott. “Magnetic Structures and Phase Transitions in Thin and Ultrathin Films of Heavy Lanthanide Metals Investigated by Resonant Magnetic X-Ray Scattering”. PhD thesis. Frei Universität Berlin, 2004.

[28] H. Ott et al. “Depth-resolved magnetic structure across the ferromagnetic to helical-antiferromagnetic phase transition in Dy/W(110)”. In: *Phys. Rev. B* 82 (2010), p. 214408.

[29] U.J. Fourier. *Magnetism: Fundamentals, Materials and Applications*. Magnetism. Springer New York, 2002.

[30] J. Stöhr and H.C. Siegmann. *Magnetism: From Fundamentals to Nanoscale Dynamics*. Springer Series in Solid-State Sciences. Springer, 2006.

[31] T. Chatterji. *Neutron Scattering from Magnetic Materials*. Elsevier Science, 2005.

[32] B. T. Thole et al. “X-ray circular dichroism as a probe of orbital magnetization”. In: *Physical Review Letters* 68.12 (1992), pp. 1943–1946.

[33] N.A. Spaldin. *Magnetic Materials: Fundamentals and Device Applications*. Cambridge University Press, 2003.

[34] C. Kittel. *Introduction to Solid State Physics*. Wiley, 2004.

[35] P.W. Atkins and R.S. Friedman. *Molecular Quantum Mechanics*. OUP Oxford, 2011.

[36] R. Gross and A. Marx. *Festkörperphysik*. De Gruyter Studium. Walter de Gruyter GmbH, 2014.

[37] J.M.D. Coey. *Magnetism and Magnetic Materials*. EngineeringPro collection. Cambridge University Press, 2010.

[38] S. Blundell. *Magnetism in Condensed Matter*. Oxford Master Series in Condensed Matter Physics. OUP Oxford, 2001.

[39] G. Engdahl and I.D. Mayergoyz. *Handbook of Giant Magnetostrictive Materials*. Electromagnetism. Elsevier Science, 1999.

[40] J. Jensen and A.R. Mackintosh. *Rare earth magnetism: structures and excitations*. International series of monographs on physics. Clarendon Press, 1991.

[41] W. C. Koehler. “Magnetic Properties of RareEarth Metals and Alloys”. In: *Journal of Applied Physics* 36.3 (1965), pp. 1078–1087.

[42] M. K. Wilkinson et al. “Neutron Diffraction Investigation of Magnetic Ordering in Dysprosium”. In: *Journal of Applied Physics* 32.3 (1961), S48–S49.

[43] W. C. Koehler et al. “Magnetic Structures of Holmium. I. The Virgin State”. In: *Phys. Rev.* 151 (1966), pp. 414–424.

[44] F. J. Darnell and E. P. Moore. “Crystal Structure of Dysprosium at Low Temperatures”. In: *Journal of Applied Physics* 34.4 (1963), pp. 1337–1338.

[45] T. A. Kaplan and D. H. Lyons. “Theory of Indirect Exchange Interactions in Rare-Earth Metals”. In: *Phys. Rev.* 129 (1963), pp. 2072–2086.

[46] Frederick Specht. “Indirect Exchange Interaction in the Rare-Earth Metals”. In: *Phys. Rev.* 162 (1967), pp. 389–398.

[47] W. Nolting and A. Ramakanth. *Quantum Theory of Magnetism*. Springer Berlin Heidelberg, 2009.

[48] Keith A. McEwen, Uschi Steigenberger, and Jens Jensen. “Spin waves, phonons, and crystal-field excitations in thulium”. In: *Phys. Rev. B* 43 (1991), pp. 3298–3310.

[49] W. E. Evenson and S. H. Liu. “Theory of Magnetic Ordering in the Heavy Rare Earths”. In: *Physical Review* 178.2 (1969), pp. 783–794.

[50] I. D. Hughes et al. “Lanthanide contraction and magnetism in the heavy rare earth elements”. In: *Nature* 446.7136 (2007), pp. 650–653.

[51] W. C. Koehler et al. “Spin-Wave Dispersion Relations in Gadolinium”. In: *Phys. Rev. Lett.* 24 (1970), pp. 16–18.

[52] J. Jensen, J. G. Houmann, and H. Bjerrum Møller. “Spin waves in terbium. I. Two-ion magnetic anisotropy”. In: *Phys. Rev. B* 12 (1975), pp. 303–319.

[53] R. M. Nicklow et al. “Spin-Wave Dispersion Relation in Dysprosium Metal”. In: *Phys. Rev. Lett.* 26 (1971), pp. 140–143.

[54] C. C. Larsen, J. Jensen, and A. R. Mackintosh. “Magnetic excitations in commensurable periodic structures”. In: *Phys. Rev. Lett.* 59 (1987), pp. 712–715.

[55] Kristian M. Döbrich. “Bandstrukturen und Fermiflächen schwerer Lanthanidmetalle bei magnetischen Phasenübergängen”. PhD thesis. Frei Universität Berlin, 2007.

[56] Earl Callen and Herbert B. Callen. “Magnetostriction, Forced Magnetostriction, and Anomalous Thermal Expansion in Ferromagnets”. In: *Phys. Rev.* 139 (1965), A455–A471.

[57] Bernard R. Cooper. “Spin Waves and Magnetic Resonance in Rare-Earth Metals: Thermal, Applied-Field, and Magnetoelastic Effects”. In: *Phys. Rev.* 169 (1968), pp. 281–294.

[58] S. Legvold, J. Alstad, and J. Rhyne. “Giant Magnetostriction in Dysprosium and Holmium Single Crystals”. In: *Phys. Rev. Lett.* 10 (1963), pp. 509–511.

[59] F. J. Darnell. “Temperature Dependence of Lattice Parameters for Gd, Dy, and Ho”. In: *Physical Review* 130.5 (1963), pp. 1825–1828.

[60] F. J. Darnell. “Lattice Parameters of Terbium and Erbium at Low Temperatures”. In: *Phys. Rev.* 132 (1963), pp. 1098–1100.

[61] E W Lee. “The magnetoelastic behaviour of antiferromagnets having helical spin configurations”. In: *Proceedings of the Physical Society* 84.5 (1964), p. 693.

[62] C. Kittel. “Model of Exchange-Inversion Magnetization”. In: *Phys. Rev.* 120 (1960), pp. 335–342.

[63] M. Griffel, R. E. Skochdopole, and F. H. Spedding. “The Heat Capacity of Gadolinium from 15 to 355°K”. In: *Phys. Rev.* 93 (1954), pp. 657–661.

[64] V.K. Pecharsky, K.A. Gschneidner, and D. Fort. “Superheating and other unusual observations regarding the first order phase transition in Dy”. In: *Scripta Materialia* 35.7 (1996), pp. 843 – 848.

[65] B. C. Gerstein et al. “Heat Capacity of Lutetium from 6 to 300K”. In: *The Journal of Chemical Physics* 51.7 (1969), pp. 2924–2928.

[66] Alexander von Reppert. “Ultrafast magnetostriction in dysprosium studied by femtosecond X-Ray diffraction”. MA thesis. Universität Potsdam, 2015.

[67] G. Ventura and M. Perfetti. *Thermal Properties of Solids at Room and Cryogenic Temperatures*. International Cryogenics Monograph Series. Springer Netherlands, 2014.

[68] Maurice Griffel, R. E. Skochdopole, and F. H. Spedding. “Heat Capacity of Dysprosium from 15 to 300K”. In: *The Journal of Chemical Physics* 25.1 (1956), pp. 75–79.

[69] L. D. Jennings, R. E. Miller, and F. H. Spedding. “Lattice Heat Capacity of the Rare Earths. Heat Capacities of Yttrium and Lutetium from 15350 K”. In: *The Journal of Chemical Physics* 33.6 (1960), pp. 1849–1852.

[70] S.A. Nikitin et al. “Magnetic part of specific heat in high-purity Dy single crystal”. In: *Journal of Magnetism and Magnetic Materials* 96.1 (1991), pp. 26 –28.

[71] D. W. Boys and S. Legvold. “Thermal Conductivities and Lorenz Functions of Dy, Er, and Lu Single Crystals”. In: *Phys. Rev.* 174 (1968), pp. 377–384.

[72] W. J. Nellis and S. Legvold. “Thermal Conductivities and Lorenz Functions of Gadolinium, Terbium, and Holmium Single Crystals”. In: *Phys. Rev.* 180 (1969), pp. 581–590.

[73] H. E. Nigh, S. Legvold, and F. H. Spedding. “Magnetization and Electrical Resistivity of Gadolinium Single Crystals”. In: *Phys. Rev.* 132 (1963), pp. 1092–1097.

[74] Eugene Hecht. *Optik*. Ed. by N. Armağan and N. Can. Akademi Yayın Hizmetleri, 2005.

[75] Jae Bin Lee, Kwangu Kang, and Seong Hyuk Lee. “Comparison of Theoretical Models of Electron-Phonon Coupling in Thin Gold Films Irradiated by Femtosecond Pulse Lasers”. In: *MATERIALS TRANSACTIONS* 52.3 (2011), pp. 547–553.

[76] B. Y. Mueller and B. Rethfeld. “Relaxation dynamics in laser-excited metals under nonequilibrium conditions”. In: *Phys. Rev. B* 87 (2013), p. 035139.

[77] M. B. Agranat et al. “Interaction of picosecond laser pulses with the electron, spin, and phonon subsystems of nickel”. In: *Sov. Phys. JETP* 59.4 (1984), p. 804.

[78] E. Beaurepaire et al. “Ultrafast Spin Dynamics in Ferromagnetic Nickel”. In: *Phys. Rev. Lett.* 76 (1996), pp. 4250–4253.

[79] Pui-Wai Ma, S. L. Dudarev, and C. H. Woo. “Spin-lattice-electron dynamics simulations of magnetic materials”. In: *Phys. Rev. B* 85 (2012), p. 184301.

[80] T. Roth et al. “Temperature Dependence of Laser-Induced Demagnetization in Ni: A Key for Identifying the Underlying Mechanism”. In: *Phys. Rev. X* 2 (2012), p. 021006.

[81] Matthieu Nicoul et al. “Picosecond acoustic response of a laser-heated gold-film studied with time-resolved x-ray diffraction”. In: *Applied Physics Letters* 98.19 (2011), p. 191902.

[82] Shouhua Nie et al. “Measurement of the Electronic Grüneisen Constant Using Femtosecond Electron Diffraction”. In: *Phys. Rev. Lett.* 96 (2006), p. 025901.

[83] A. Melnikov et al. “Coherent Optical Phonons and Parametrically Coupled Magnons Induced by Femtosecond Laser Excitation of the Gd(0001) Surface”. In: *Phys. Rev. Lett.* 91 (2003), p. 227403.

[84] Mischa Bonn et al. “Ultrafast electron dynamics at metal surfaces: Competition between electron-phonon coupling and hot-electron transport”. In: *Phys. Rev. B* 61 (2000), pp. 1101–1105.

[85] Uwe Bovensiepen. “Coherent and incoherent excitations of the Gd(0001) surface on ultrafast timescales”. In: *Journal of Physics: Condensed Matter* 19.8 (2007), p. 083201.

[86] M. Battiato, K. Carva, and P. M. Oppeneer. “Superdiffusive Spin Transport as a Mechanism of Ultrafast Demagnetization”. In: *Phys. Rev. Lett.* 105 (2010), p. 027203.

[87] C Stamm et al. “Femtosecond modification of electron localization and transfer of angular momentum in nickel”. In: *Nature Materials* 6.10 (2007), pp. 740–743.

[88] Christoph Trabant. “Ultrafast photoinduced phase transitions in complex materials probed by time-resolved resonant soft x-ray diffraction”. PhD thesis. Universität Potsdam, 2014.

[89] W. Hübner and K. H. Bennemann. “Simple theory for spin-lattice relaxation in metallic rare-earth ferromagnets”. In: *Phys. Rev. B* 53 (1996), pp. 3422–3427.

[90] L.D. Landau and E.M. Lifshitz. *Statistical Physics*. Volume 5. Pergamon Press, 1958.

[91] P. Tol dano and V. Dmitriev. *Reconstructive Phase Transitions: In Crystals and Quasicrystals*. World Scientific, 1996.

[92] K Binder. “Theory of first-order phase transitions”. In: *Reports on Progress in Physics* 50.7 (1987), p. 783.

[93] Uwe C. Täuber. *Critical Dynamics, A Field Theory Approach to Equilibrium and Non-Equilibrium Scaling Behavior*. Cambridge University Press, 2014.

[94] H. Eugene Stanley. “Scaling, universality, and renormalization: Three pillars of modern critical phenomena”. In: *Rev. Mod. Phys.* 71 (1999), S358–S366.

[95] Kenneth G. Wilson. “Renormalization Group and Critical Phenomena. I. Renormalization Group and the Kadanoff Scaling Picture”. In: *Phys. Rev. B* 4 (1971), pp. 3174–3183.

[96] C. Kadanoff L.P. ed. Domb and M. S. Green. *Scaling, Universality and Operator Algebras*. Academic Press, 1976.

[97] J. C. Le Guillou and J. Zinn-Justin. “Critical Exponents for the n-Vector Model in Three Dimensions from Field Theory”. In: *Phys. Rev. Lett.* 39 (1977), pp. 95–98.

[98] Andrea Pelissetto and Ettore Vicari. “Critical phenomena and renormalization-group theory”. In: *Physics Reports* 368.6 (2002), pp. 549 –727.

[99] Hikaru Kawamura. “Monte Carlo Study of Chiral Criticality XY and Heisenberg Stacked-Triangular Antiferromagnets”. In: *Journal of the Physical Society of Japan* 61.4 (1992), pp. 1299–1325.

[100] P de V Du Plessis, A M Venter, and G H F Brits. “Neutron diffraction and ultrasonic studies of the helical implies/implied by paramagnetic phase transition in dysprosium and holmium”. In: *Journal of Physics: Condensed Matter* 7.50 (1995), p. 9863.

[101] M E Fisher. “The theory of equilibrium critical phenomena”. In: *Reports on Progress in Physics* 30.2 (1967), p. 615.

[102] P. C. Hohenberg and B. I. Halperin. “Theory of dynamic critical phenomena”. In: *Rev. Mod. Phys.* 49 (1977), pp. 435–479.

[103] Leticia F. Cugliandolo. *Out of equilibrium dynamics of complex systems*. Université Pierre et Marie Curie, 2013.

[104] R. J. Pollina and B. Lüthi. “Critical Scattering of Sound in Rare-Earth Metals”. In: *Phys. Rev.* 177 (1969), pp. 841–847.

[105] B. Luthi and R. J. Pollina. “Critical Attenuation of Sound in Gadolinium”. In: *Phys. Rev.* 167 (1968), pp. 488–492.

[106] Muhammad Sultan et al. “Electron- and phonon-mediated ultrafast magnetization dynamics of Gd(0001)”. In: *Phys. Rev. B* 85 (2012), p. 184407.

[107] X. J. Liu et al. “Critical behavior of a photodisordered spin system in doped manganite”. In: *Phys. Rev. B* 64 (2001), p. 100401.

[108] T. Kise et al. “Ultrafast Spin Dynamics and Critical Behavior in Half-Metallic Ferromagnet: Sr_2FeMoO_6”. In: *Phys. Rev. Lett.* 85 (2000), pp. 1986–1989.

[109] V. Pecharsky and P. Zavalij. *Fundamentals of Powder Diffraction and Structural Characterization of Metarials*. Springer US, 2003.

[110] M. Birkholz. *Thin Film Analysis by X-Ray Scattering*. Wiley, 2006.

[111] J. Als-Nielsen and D. McMorrow. *Elements of Modern X-ray Physics*. Wiley, 2011.

[112] B.D. Cullity. *Elements of X-ray Diffraction*. Addison-Wesley series in metallurgy and materials. Addison-Wesley Publishing Company, 1978.

[113] I. K. Robinson. “Crystal truncation rods and surface roughness”. In: *Phys. Rev. B* 33 (1986), pp. 3830–3836.

[114] Enrico Schierle. “Antiferromagnetism in Thin Films Studied by Resonant Magnetic Soft X-Ray Scattering”. PhD thesis. Frei Universität Berlin, 2006.

[115] Boris W. Batterman and Henderson Cole. “Dynamical Diffraction of X Rays by Perfect Crystals”. In: *Rev. Mod. Phys.* 36 (1964), pp. 681–717.

[116] J Fink et al. “Resonant elastic soft x-ray scattering”. In: *Reports on Progress in Physics* 76.5 (2013), p. 056502.

[117] B.H. Bransden and C.J. Joachain. *Quantum Mechanics*. Prentice Hall, 2000.

[118] J. P. Hannon et al. “X-Ray Resonance Exchange Scattering”. In: *Phys. Rev. Lett.* 61 (1988), pp. 1245–1248.

[119] D. Attwood. *Soft X-Rays and Extreme Ultraviolet Radiation: Principles and Applications*. EBSCO ebook academic collection. Cambridge University Press, 2000.

[120] Nele Thielemann-Kühn. “Optically induced ferro- and antiferromagnetic dynamics in the rare-earth metal dysprosium”. PhD thesis. Universität Potsdam, 2017.

[121] Christian Vettier. “Neutrons and X-rays: two probes for magnetism”. In: *Physica B: Condensed Matter* 192.1 (1993), pp. 1 –13.

[122] A. Koc et al. “Ultrafast x-ray diffraction thermometry measures the influence of spin excitations on the heat transport through nanolayers”. In: *Phys. Rev. B* 96 (2017), p. 014306.

[123] A Koc et al. “Grueneisen-approach for the experimental determination of transient spin and phonon energies from ultrafast x-ray diffraction data: gadolinium”. In: *Journal of Physics: Condensed Matter* 29.26 (2017), p. 264001.

[124] H. Navirian et al. “Synchrotron-based ultrafast x-ray diffraction at high repetition rates”. In: *Rev. Sci. Instrum.* 83.6 (2012), p. 063303.

[125] Matthias Reinhardt et al. “Optimized spatial overlap in optical pump-X-ray probe experiments with high repetition rate using laser-induced surface distortions”. In: *Journal of Synchrotron Radiation* 23.2 (2016), pp. 474–479.

[126] Matthias Reinhardt and Wolfram Leitenberger. “XPP: X-ray Pump Probe station at BESSY II”. In: *Journal of large-scale research facilities* A89.2 (2016).

[127] B. Henrich et al. “PILATUS: A single photon counting pixel detector for X-ray applications”. In: *Nuclear Instruments and Methods in Physics Research Section A: Accelerators, Spectrometers, Detectors and Associated Equipment* 607.1 (2009). Radiation Imaging Detectors 2008, pp. 247 –249.

[128] T. Ejdrup et al. “Picosecond time-resolved laser pump/X-ray probe experiments using a gated single-photon-counting area detector”. In: *Journal of Synchrotron Radiation* 16.3 (2009), pp. 387–390.

[129] K. Dumesnil et al. “Magnetoelastic and Exchange Contributions to the Helical-Ferromagnetic Transition in Dysprosium Epitaxial Films”. In: *EPL (Europhysics Letters)* 31.1 (1995), p. 43.

[130] V. Holy, U. Pietsch, and T. Baumbach. *High-Resolution X-Ray Scattering from Thin Films and Multilayers*. Springer Tracts in Modern Physics. Springer Berlin Heidelberg, 1998.

[131] B.L. Henke, E.M. Gullikson, and J.C. Davis. “X-Ray Interactions: Photoabsorption, Scattering, Transmission, and Reflection at E = 50-30,000 eV, Z = 1-92”. In: *Atomic Data and Nuclear Data Tables* 54.2 (1993), pp. 181 –342.

[132] Daniel Schick et al. “Ultrafast reciprocal-space mapping with a convergent beam”. In: *Journal of Applied Crystallography* 46.5 (2013), pp. 1372–1377.

[133] Erling Pytte. “Spin-phonon interactions in a Heisenberg ferromagnet”. In: *Annals of Physics* 32.3 (1965), pp. 377 –403.

[134] J. F. Smith and J. A. Gjevre. “Elastic constants of yttrium single crystals in the temperature range 4.2-400 K”. In: *Journal of Applied Physics* 31.4 (1960), pp. 645–647.

[135] M. Rosen and H. Klimker. “Low-Temperature Elasticity and Magneto-Elasticity of Dysprosium Single Crystals”. In: *Physical Review B* 1.9 (1970), pp. 3748–3756.

[136] Keith J. Carroll. “Elastic Constants of Niobium from 4.2 to 300 K”. In: *Journal of Applied Physics* 36.11 (1965), pp. 3689–3690.

[137] D. Schick et al. “udkm1DsimA simulation toolkit for 1D ultrafast dynamics in condensed matter”. In: *Computer Physics Communications* 185.2 (2014), pp. 651 –660.

[138] F. Barson, S. Legvold, and F. H. Spedding. “Thermal Expansion of Rare Earth Metals”. In: *Phys. Rev.* 105 (1957), pp. 418–424.

[139] S. B. Palmer, E.W. Lee, and M. N. Islam. “The elastic constants of gadolinium, terbium and erbium”. In: *Proceedings of the Royal Society of London A: Mathematical, Physical and Engineering Sciences* 338.1614 (1974), pp. 341–357.

[140] Muhammad Sultan, Alexey Melnikov, and Uwe Bovensiepen. “Ultrafast magnetization dynamics of Gd(0001): Bulk versus surface”. In: *Physica Status Solidi B* 248.10 (2011), pp. 2323–2329.

[141] Daniel Schick et al. “Analysis of the halo background in femtosecond slicing experiments”. In: *Journal of Synchrotron Radiation* 23.3 (2016), pp. 700–711.

[142] S. Khan et al. “Femtosecond Undulator Radiation from Sliced Electron Bunches”. In: *Phys. Rev. Lett.* 97 (2006), p. 074801.

[143] Karsten Holldack et al. “Femtospex: A versatile optical pump-soft x-ray probe facility with 100fs x-ray pulses of variable polarization”. In: *Journal of Synchrotron Radiation* 21.5 (2014), pp. 1090–1104.

[144] H. Ott et al. “Magnetic x-ray scattering at the M_5 absorption edge of Ho”. In: *Phys. Rev. B* 74 (2006), p. 094412.

[145] M. B. Salamon et al. “Long-range incommensurate magnetic order in a Dy-Y multilayer”. In: *Phys. Rev. Lett.* 56 (1986), pp. 259–262.

[146] K. Dumesnil et al. “Magnetic structure of dysprosium in epitaxial Dy films and in Dy/Er superlattices”. In: *Phys. Rev. B* 54 (1996), pp. 6407–6420.

[147] Johannes Kimling et al. “Ultrafast demagnetization of FePt:Cu thin films and the role of magnetic heat capacity”. In: *Phys. Rev. B* 90 (2014), p. 224408.

A. Additional results of UXRD experiments

Transient lattice strain in dysprosium at $F_i = 0.7\,\mathrm{mJ/cm^2}$

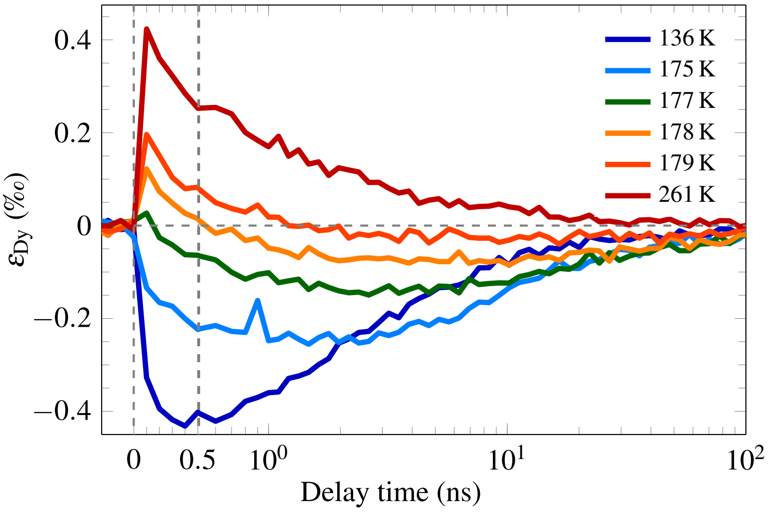

Figure A.1.: Temperature-dependence of the transient strain in directly excited Dy in sample I after the ultrafast photoexcitation with an incident fluence of $F_i = 0.7\,\mathrm{mJ/cm^2}$. Note that the x-axis is split into a linear and a logarithmic part. The dashed gray lines indicate $t = 0$, $\varepsilon = 0$, and the time where the x-axis is split into the linear and logarithmic scales at 0.5 ns.

Peak width change of the Bragg peaks of Y and Dy after photoexcitation at $F_i = 2\,\mathrm{mJ/cm^2}$

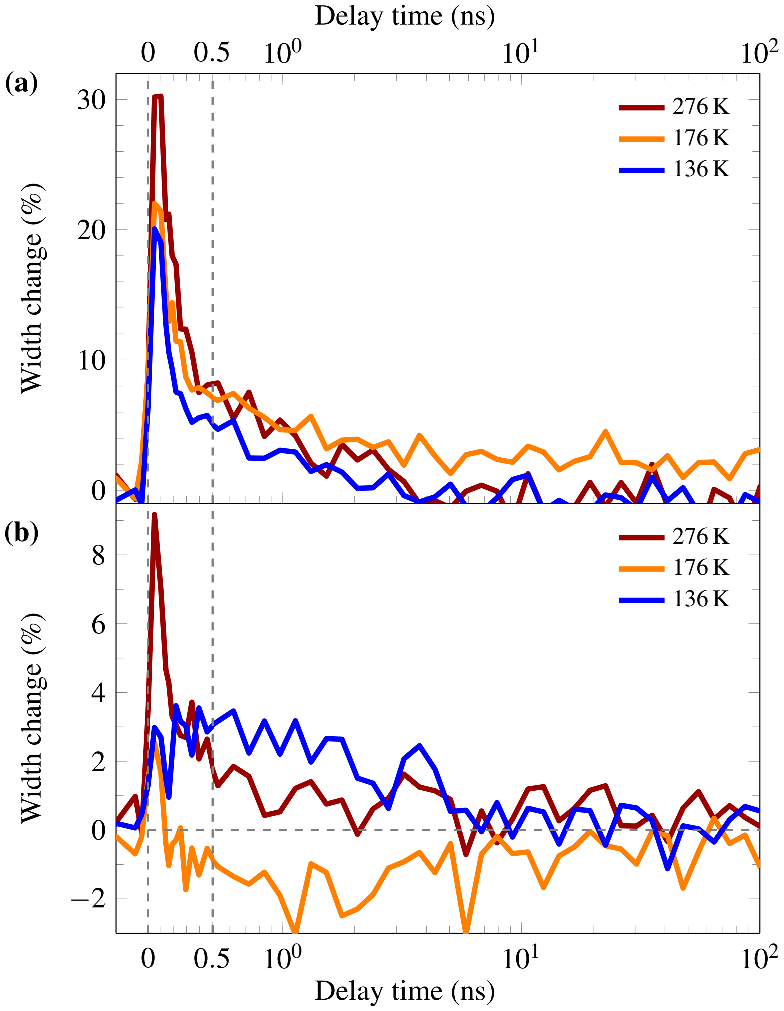

Figure A.2.: The peak width change of the structural Bragg peak of a) Y and b) Dy in sample II after ultrafast laser heating with incidence fluence of $F_i = 2\,\mathrm{mJ/cm^2}$. Note that the x-axis is split into a linear and a logarithmic part.

B. Additional results of RSXD experiments

Peak width of the magnetic Bragg peak of Dy

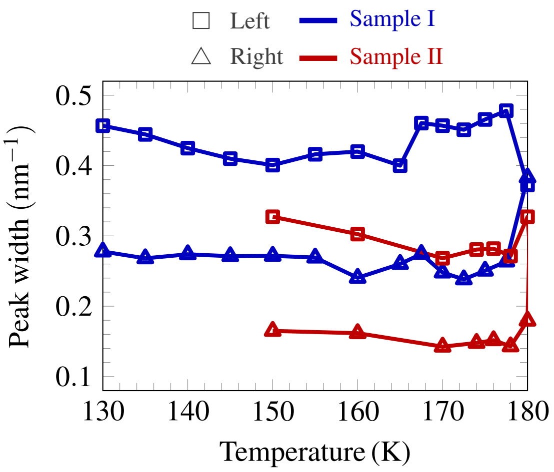

Figure B.1.: The results of the pseudo-Voigt fit of the asymmetric magnetic Bragg reflection where the peak widths for the left (squares) and right (triangles) sides are allowed to be fit individually, plotted as function of temperature. The results are shown for samples I and II (see figure 4.3) in thermal equilibrium.

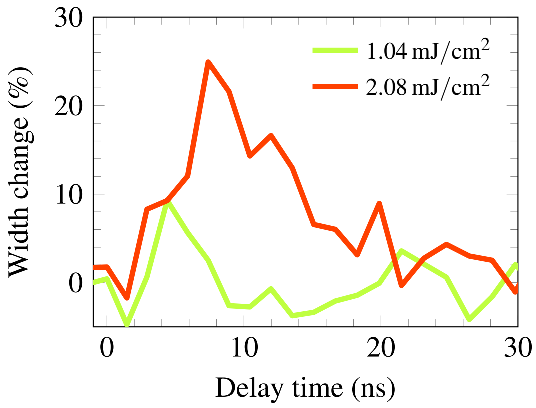

Figure B.2.: The fit results of the peak width of the Dy magnetic Bragg peak in sample I at start temperature $T = 160\,K$ for two excitation fluences where a successful fit has been achieved.

Absolute changes of the parameters at temperature study

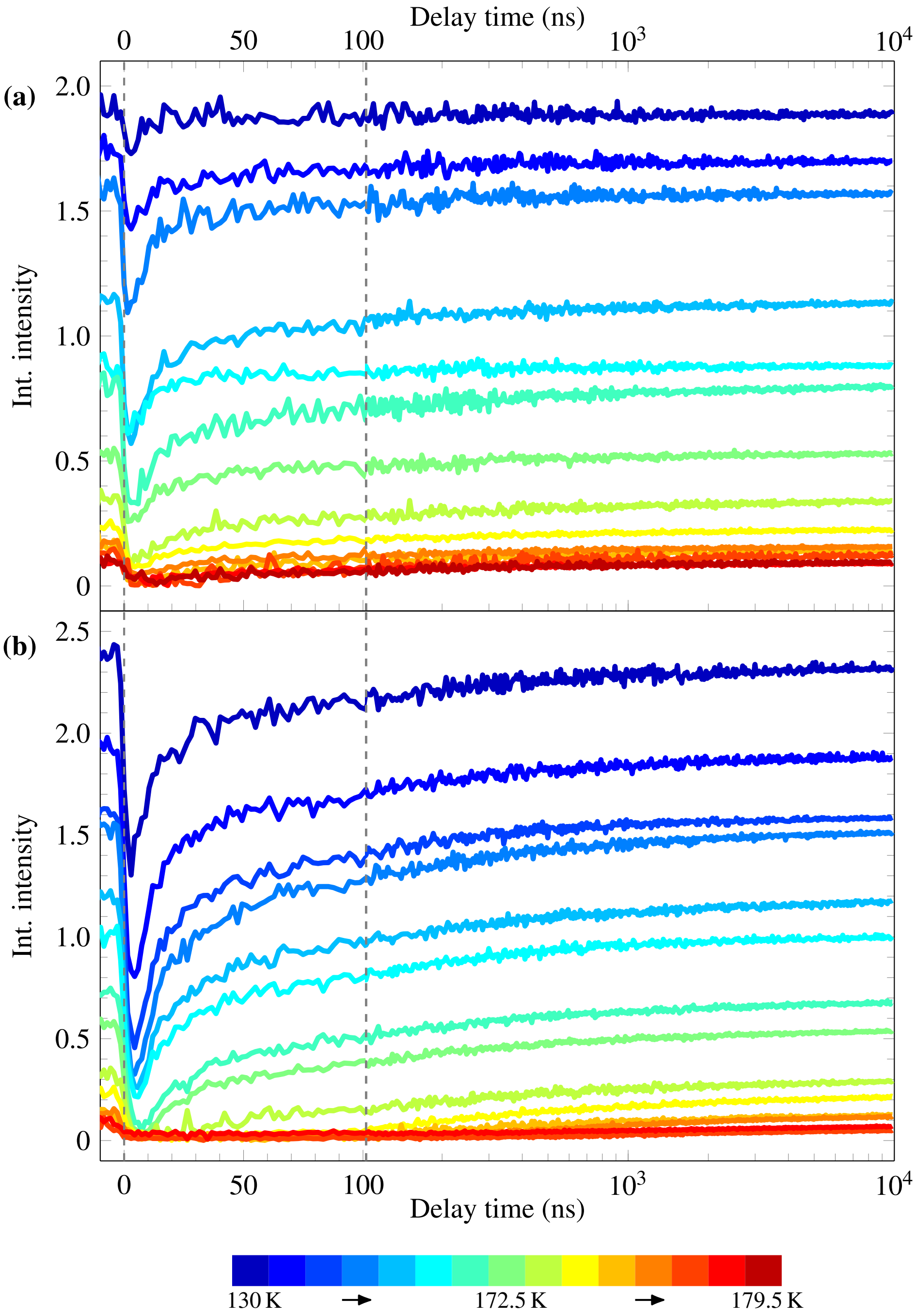

Figure B.3.: The transient absolute change of the integrated intensity of the Dy magnetic peak measured at a) $F_a = 0.35\,\mathrm{mJ/cm^2}$ and b) $F_a = 1.4\,\mathrm{mJ/cm^2}$ for different start temperatures between 130 K and 179.5 K.

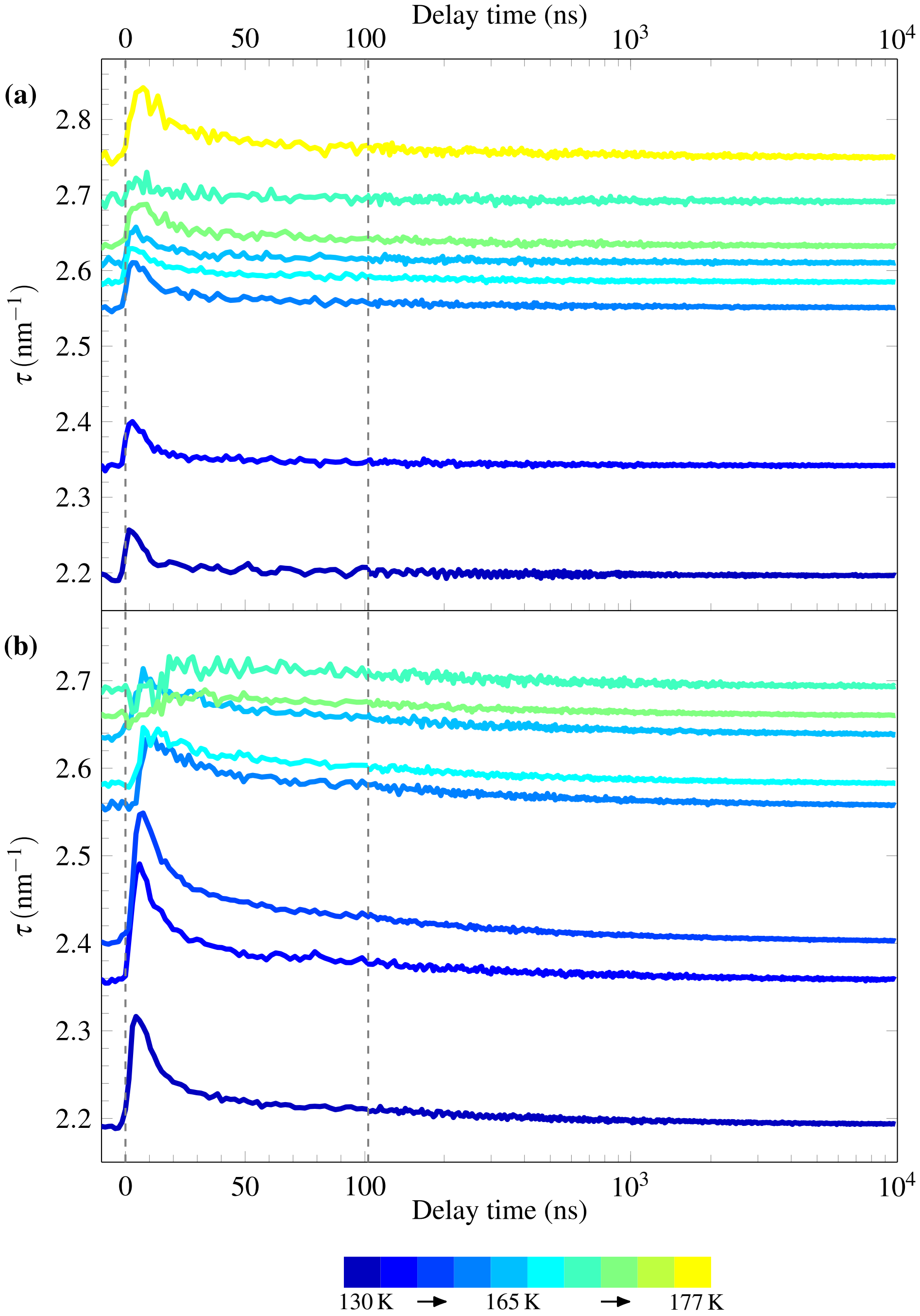

Figure B.4.: The transient absolute change of the modulation vector τ of the Dy magnetic peak measured at a) $F_a = 0.35\,\mathrm{mJ/cm^2}$ and b) $F_a = 1.4\,\mathrm{mJ/cm^2}$ for different start temperatures between 130 K and 179.5 K.

List of publications

1) A. Koc, M. Reinhardt, A. von Reppert, M. Rössle, W. Leitenberger, M. Gleich, M. Weinelt, F. Zamponi, and M. Bargheer, “Grueneisen-approach for the experimental determination of transient spin and phonon energies from ultrafast x-ray diffraction data: gadolinium”, *Journal of Physics: Condensed Matter*, **29**, 264001, 2017.
2) A. Koc, M. Reinhardt, A. von Reppert, M. Rössle, W. Leitenberger, K. Dumesnil, P. Gaal, F. Zamponi, and M. Bargheer, “Ultrafast x-ray diffraction thermometry measures the influence of spin excitations on the heat transport through nanolayers”, *Physical Review B*, **96**, 014306, 2017.
3) A. von Reppert, J. Pudell, A. Koc, M. Reinhardt, W. Leitenberger, K. Dumesnil, F. Zamponi, and M. Bargheer, “Persistent nonequilibrium dynamics of the thermal energies in the spin and phonon systems of an antiferromagnet”, *Structural Dynamics*, **3**, 054302, 2016.
4) M. Sander, A. Koc, C.T. Kwamen, H. Michaels, A. v. Reppert, J. Pudell, F. Zamponi, M. Bargheer, J. Sellmann, J. Schwarzkopf, and P. Gaal, “Characterization of an ultrafast Bragg-Switch for shortening hard x-ray pulses”, *Journal of Applied Physics*, **120**, 193101, 2016.
5) Matthias Reinhardt, Azize Koc, Wolfram Leitenberger, Peter Gaal and Matias Bargheer, “Optimized spatial overlap in optical pump-Xray probe experiments with high repetition rate using laser-induced surface distortions”, *Journal of Synchrotron Radiation*, **23**, 474-479, 2016.
6) V. Iurchuk, D. Schick, J. Bran, D. Colson, A. Forget, D. Halley, A. Koc, M. Reinhardt, C. Kwamen, N. A. Morley, M. Bargheer, M. Viret, R. Gumeniuk, G. Schmerber, B. Doudin, and B. Kundys, “Optical Writing of Magnetic Properties by Remanent Photostrcition”, *Physical Review Letters*, **117**, 107403, 2016.

Acknowledgments

First of all, I would like to thank my supervisor Prof. Dr. Matias Bargheer for giving me the opportunity to work on such an exciting project and for the support and discussions.

A special thank to Dr. Matthias Rössle who always motivated me to keep going, helped me a lot to improve my English skills, had the patience to answer my all questions and the time to discuss interesting physics with me. I am very grateful for that.

I would like to thank all the people in the *Ultrafast Dynamics in Condensed Matter* group of the University of Potsdam.

Thanks to Dr. Matthias Reinhardt, my dear colleage Jan-Etienne Pudell, Dr. Flavio Zamponi, Dr. Daniel Schick and all other colleagues who supported me during the beamtimes at BESSY.

Many many thanks to Christelle Kwamen. Not only did she help me at BESSY, but we had many nice conversations and she was always there to listen when I had problems.

Bu zorlu süreçte benden desteğini hiç esirgemeyen, bıkmadan usanmadan beni dinleyen, çok sevdiğim kıymetli arkadaşlarıma ve canım aileme en içten teşekkürlerimi sunuyorum.

Selbstständigkeitserklärung

Hiermit versichere ich, dass ich die vorliegende Dissertation selbstständig erarbeitet und verfasst habe. Ich habe die vorliegende Dissertation ohne Benutzung anderer als der angegebenen Quellen und Hilfsmittel angefertigt und die direkt oder indirekt übernommenen Zitate aus anderen Quellen kenntlich gemacht.

Diese Dissertation ist bisher an keiner anderen Hochschule oder Universität eingereicht oder veröffentlicht worden.

Potsdam, den 05.09.2018 Azize Koç